Louisiana State University
LSU Digital Commons

LSU Doctoral Dissertations | Graduate School

2015

Cellulose Nanofibers from Energycane Bagasse and Their Applications in Core-Shell Structured Hydrogels

Yiying Yue
Louisiana State University and Agricultural and Mechanical College

Follow this and additional works at: https://digitalcommons.lsu.edu/gradschool_dissertations

 Part of the Environmental Sciences Commons

Recommended Citation

Yue, Yiying, "Cellulose Nanofibers from Energycane Bagasse and Their Applications in Core-Shell Structured Hydrogels" (2015). *LSU Doctoral Dissertations*. 1742.
https://digitalcommons.lsu.edu/gradschool_dissertations/1742

This Dissertation is brought to you for free and open access by the Graduate School at LSU Digital Commons. It has been accepted for inclusion in LSU Doctoral Dissertations by an authorized graduate school editor of LSU Digital Commons. For more information, please contactgradetd@lsu.edu.

CELLULOSE NANOFIBERS FROM ENERGYCANE BAGASSE AND THEIR APPLICATIONS IN CORE-SHELL STRUCTURED HYDROGELS

A Dissertation

Submitted to the Graduate Faculty of the
Louisiana State University and
Agricultural and Mechanical College
in partial fulfillment of the
requirements for the degree of
Doctor of Philosophy

in

The School of Renewable Natural Resources

by
Yiying Yue
B.S., Heilongjiang Institute of Science and Technology, 2007
M.S., Louisiana State University, 2011
M.S., Louisiana State University, 2014
December 2015

ACKNOWLEDGEMENTS

I would like to take this precious opportunity to appreciate my major adviser, Dr. Qinglin Wu for his guidance, advice and support throughout this work. Appreciation also goes to my committee members, Dr. Alfred D. French for his inspiring and enlightening suggestions on my research, Dr. Quang V. Cao for his invaluable and insightful comments on statistics, Dr. Giovanna M. Aita for introducing me the method of compositional analysis and helping me with kind and encouraging discussions.

I am indebted to many of my colleagues in the Engineering Composites Laboratory, School of Renewable Natural Resources, LSU. Mr. Kunlin Song, Dr. Meichun Li, Mr. Xiuxuan Sun and Mr. Jinlong zhang are appreciated for their assistance on my experiments.

My deepest thanks go to my family and friends for their support throughout my life. In particular, I would like to thank my mother for spending many weekends and nights in the laboratory with me. I am very grateful for my husband, Jingquan Han, for travelling from China to USA to accompany me, for helping me resolve technical problems, and most importantly of all, for his endless support, encouragement, love and belief in me.

TABLE OF CONTENTS

LIST OF TABLES

LIST OF FIGURES

ABSTRACT

Cellulose fibers (Cellulose I, cellulose II and cellulose I/II Hybrid fibers) were successfully extracted from energycane bagasse by using a combined NaOH and $NaClO_2$ treatment. After the delignification process, most lignin and hemicellulose were removed with a 27.4wt% yield of cellulose fibers, and the mean diameter of cellulose fibers decreased from 137 ± 46 (raw fiber bundles) to $12 \pm 5\mu m$ (unpacked fibers). The raw bagasse fibers showed a three-step pyrolysis process, while isolated cellulose fibers had a one-step pyrolysis process. $NaClO_2$ treatment caused the reduction of cellulose thermal stability due to its acting on lignin and cellulose. With 10h NaOH treatment, the ribbon shaped cellulose I fibers were converted to cellulose I/II Hybrid fibers with rougher surfaces. The percentage of cellulose I decreased from 100% to 5%, and the corresponding CI values increased from 58.2% to 68.8% during the conversion from cellulose I to II. After further $NaClO_2$ treatment, the CI values were decreased because of partial destruction of hydrogen bond network. XRD, NMR and FTIR results present the same trend in the degree of crystallization for all the samples.

Core-shell structured hydrogels consisting of a flexible interpenetrating polymer network (IPN) core and a rigid semi-interpenetrating polymer network (SIPN) shell were prepared through chemical crosslinking of polyvinyl alcohol (PVA) and sodium alginate (SA) with Ca^{2+} and glutaraldehyde. Cellulose nanoparticles (CNPs) with cellulose I and I/II structures extracted from energycane bagasse were incorporated in the hydrogels and their effects on hydrogels properties were investigated. The shell was micro-porous and the core was macro-porous, the translucent hydrogels had a water content of ~93 wt%. The hydrogels could be used in multiple adsorption–desorption cycles for dyes and the maximum methyl blue adsorption capacity increased 10% after incorporating CNPs. The homogeneous distribution of CNPs in PVA-SA polymer matrix, allowed

additional hydrogen bonds among the polymer molecular chains, resulting in enhanced density, viscoelasticity, and mechanical strength for the hydrogel. With incorporation cellulose nanofiber I, the storage modulus of the IPN core and compressive strength of the hydrogel reached 600 Pa and 79.5kPa, respectively, 13 and 3.2 times higher than values for neat hydrogel, respectively. The core/shell structure, with a high ductility core and high strength shell, gave a hydrogel with improved performance, broadening potential applications.

CHAPTER 1 INTRODUCTION

1.1 BACKGROUND

Owing to the attractive properties of low density, high strength, high tensile modulus, abundance, eco-friendliness, and sustainability (Lu et al., 2008; Thakur et al., 2013a; Thakur et al., 2013b), cellulose has broad applications, such as pharmaceuticals, engineering scaffolds, filter media, nano sensors, adhesives, skin masks, wound dressings, functional clothes, papermaking and liquid fuel production (Kumar et al., 2002; Sun et al., 2004c; Park et al., 2008a; Gatenholm and Klemm, 2010a). Cellulose offers light weight, strong reinforcing effects, and improved thermal stability in diverse materials that could be also used in automobiles and buildings (Thakur and Thakur, 2014; Thakur et al., 2014).

The raw materials for manufacturing cellulose are widely considered inexhaustible in nature. Most agricultural wastes, woody plants, forest residues, herbaceous biomass, cellulose wastes, and municipal solid wastes are sources of cellulose (Martin et al., 2007). One crop being considered as a resource for extracting cellulose is energycane which is a hybrid of commercial and wild sugarcanes. Compared to sugarcane, it is cold tolerant, requires less fertilizer and water. More importantly, it has lower sucrose content and higher fiber content, implying higher expected cellulose yields in terms of tons of plant material per acre (Kim and Day, 2011). However, the presence of a hemicellulose and lignin complex reduces accessibility to cellulose microfibrils and hinders cellulose isolation (Hubbell and Ragauskas, 2010). Therefore, delignification is a critical process towards the successful separation of cellulose from the other components of energycane bagasse.

Efficient and economic cellulose production is achieved by extracting the maximum amount of cellulose fibers from crops through delignification. Sodium hydroxide treatment has

been used to partially separate the microfibrils from the cell wall, remove natural impurities, and obtain fibers with low lignin and hemicellulose content (Moubarik et al., 2013). It is generally thought that alkali can penetrate the inter-fibril region and cleave α-ether bonds between lignin and hemicellulose (Sun et al., 2000b; Mwaikambo and Ansell, 2002). Since NaOH may not achieve complete lignin removing (Talebnia et al., 2010), a further delignification process is needed. Acidified-$NaClO_2$ is an established laboratory method for lignin removal (Hubbell and Ragauskas, 2010; Agarwal et al., 2013; Moubarik et al., 2013). Under acidic conditions, $NaClO_2$ degrades into chlorite anion (ClO_2^-) and ultimately chloride anion (Cl^-) which solubilizes the lignin components. Few researchers have focused on the impact of a combination of NaOH and $NaClO_2$ treatments on energycane bagasse. Furthermore, the properties of isolated cellulose fibers, such as morphology, cellulose reactivity, structure and thermal stability may change through different NaOH/$NaClO_2$ treatments (e.g., treatment time, the amount and concentration of chemicals). For example, Ben Sghaier et al. (2012) reported a modification of cellulose surface topography for *Agave americana* L. fiber during NaOH delignification. The extensive delignification of cellulose biomass via the $NaClO_2$ method can affect cellulose's degree of polymerization (DP) (Hubbell and Ragauskas, 2010). In addition, the effects of delignification are largely related to the properties of native energycane bagasse fibers, because the lignin content in energycane bagasse is highly variable (Hoi and Martincigh, 2013).

The structural transformation from parallel arrangement of cellulose I (native cellulose) to antiparallel-chains structure of cellulose II occurs by NaOH treatment. During this process, the fibers are converted into a swollen state and hydroxyl groups on cellulose surface are able to interact with one another to form different types of intra and intermolecular hydrogen bonds. Because of the different supermolecular structure of cellulose I and cellulose II, mechanical,

chemical and thermal properties of these two kinds of fibers, such as dimensional stability, fibrillation tendency, tensile strength, dyeability, luster and fabric smoothness, change significantly (Siroky et al., 2010). Cellulose I fibers are widely used in many industries such as clothing, cosmetics and pharmaceuticals. On the other hand, cellulose II fibers have some preferable properties over cellulose I fibers in clothing, smart materials (such as electro-activepaper (EAPap), sensors, actuators), biomedicine (such as tablet excipients), and reinforcing materials (such as filler and binder) (Kumar et al., 2002; Ma et al., 2011). However, the transformation from cellulose I to cellulose II is not spontaneous. The presence of lignin can somehow prevent or retard chemical penetration and swelling of cellulose, and intermingling of the cellulose molecules from adjacent microfibrils, resulting in cellulose I and II mixture. The presence of a cellulose I and II hybrid affects morphology, thermal stability and mechanical properties of cellulose fibers. Therefore, evaluating the percentage of cellulose I and II in cellulose hybrid fibers plays a crucial role to further utilize cellulose materials. A few researchers mentioned the existence of cellulose I/II mixtures in their studies (Nelson and O'Connor, 1964; Correa et al., 2010). However, little is known about the percentages of cellulose I and II in cellulose I/II hybrid fibers, and the chemical structural and morphologial properties of these hybrid fibers.

Hydrogels, which can hold a large amount of water, may be constructed from biocompatible and biodegradable materials. The characteristics of hydrogels can be tuned to be similar to human tissues, making them particularly attractive in the fields of implantable artificial organs, drug delivery, cell encapsulation and biosensors (Cushing and Anseth, 2007; Seliktar, 2012; Perez et al., 2015). However, most hydrogels are soft. Their low mechanical strength and variable dimensions with water content changes severely restrict their range of applications (Sun

et al., 2012; Zhang et al., 2015). Increased attention has thus been paid to novel hydrogel architectures including core–shell and interpenetrating network (IPN) structures that offer improved strength and smaller swelling ratios (Yang et al., 2014; Zhang et al., 2015). In recent years, core-shell or IPN structured hydrogels have found use as biomaterials and adsorbents (Kan et al., 2014; Perez et al., 2015; Zhang et al., 2015). IPNs can be classified as either semi-IPNs (SIPN) or full-IPNs. SIPNs are cross-linked linear polymer structures and IPNs consist of at least two polymers, in which one polymer networks is cross-linked in the presence of the other polymer network (Dragan, 2014; Berrebi et al., 2015; Zhang et al., 2015). IPN and SIPN structures can improve the mechanical performance and dimensional stability of functional hydrogels (Yang et al., 2014; Berrebi et al., 2015).

Sodium alginate (SA) is a linear polymer comprising 1,4-linked-β-D-mannuronic acid (M) and α-L-guluronic acid (G) units, combined in blocks of M-M, G-G and M-G (Lee and Mooney, 2012; Bidarra et al., 2014). Due to its aqueous-solubility, biocompatibility, non-toxicity, non-immunogenicity, biodegradability and acceptance by human body (Yang et al., 2014; Zhang et al., 2015), SA is a valuable biopolymer that is widely used in the textile industry (as a base for dyes), foods, biomedicines, pharmaceuticals and encapsulation materials (Lee and Mooney, 2012; Bidarra et al., 2014; Dragan, 2014). SA is hydrophilic, absorbing water quickly. Its –COOH and –OH groups participate in hydrogen bonding and van der waals force; therefore, it is an excellent natural adsorbent and is commonly used for removal of water pollutants, such as heavy metal ions, dyes, fertilizer, microorganisms and enzymes (Papageorgiou et al., 2012; Aftab et al., 2014). At a pH level of 4, the maximum amounts of –COOH groups in G units are deprotonated to --COO^-, which permits facile cross-linking by multivalent cations, such as Ca^{2+}, to form SIPN by chelation (Sun et al., 2012; Bidarra et al., 2014; Dragan, 2014; Samanta and Ray, 2014). Usually,

the SA-Ca^{2+} structure is formed only in the shell of hydrogels (Dragan, 2014). Compared to the rigid SA, poly (vinyl alcohol) (PVA), with one –OH group in each repeating unit, is more flexible (Cho et al., 2009). Therefore, PVA can be blended with SA to improve the flexibility of SA matrixes. PVA/SA blends exhibit good compatibility in aqueous solutions (Cho et al., 2009), and they can be chemically crosslinked with glutaraldehyde (GA), a commonly used crosslinking agent, to form IPN (Jao et al., 2009).

Although core-shell structures can significantly enhance the toughness of hydrogels by three-dimensional physical and/or chemical cross-linkages (Cushing and Anseth, 2007; Perez et al., 2015), the mechanical behavior of most hydrogels is still not satisfactory for some applications. To further improve hydrogel performance, adsorption capability, and dimensional stability, cellulose nanoparticles (CNPs) extracted from energycane bagasse were used to reinforce hydrogels (Thakur and Thakur, 2014). Because of the hydrophilic nature of PVA and SA, the CNPs could crosslink with hydrogen bond of the PVA/SA matrix to stabilize hydrogel (Ummartyotin and Manuspiya, 2015). To the best of our knowledge, we are unaware of any work on IPN core-SIPN shell structured hydrogels. In addition, the impacts of cellulose I/II hybrid extracted from energycane bagasse on IPN networks have not been assessed. The designed structure of a good ductility core and a high strength shell greatly improved the performance of the hydrogel, making it a suitable candidate in the areas of biosensors.

1.2 OBJECTIVES

The objectives of the research described in this work are:

1) To compare the non-cellulosic components, yield, crystallinity, and thermal stability of isolated ligno-cellulose fibers under different treatment conditions, investigate the structural features and chemical reactivity of the obtained lignocellulose, and provide a fundamental

guidance on the effects of delignification treatments on the properties of energycane bagasse fibers.

2) To characterize the morphology, crystallinity, percentage and functional groups of the cellulose I/II hybrid fibers obtained during the delignification process, qualitatively investigate crystallinity, crystal form, and estimate the percentage of cellulose I and II in the hybrid fibers.

3) To develop functional core-shell structured hydrogels consisting of a rigid SIPN shell and a flexible IPN core through chemical crosslinking of sodium alginate-polyvinyl alcohol with Ca^{2+} and glutaraldehyde, thoroughly study the structure and characteristics of the hydrogels, explore the gelation mechanism of the hydrogel with good ductility core and high strength shell, and investigate the effects of the CNP length, aspect ratio and crystal structure on the density, water content, morphology, thermal stability, optical transmittance, dynamic rheological properties, compression and adsorption capacity of the hydrogels.

1.3 ORGANIZATION OF DISSERTATION

Chapter 1 provides an overall introduction of this research and the structure of this dissertation.

Chapter 2 studies the structural, chemical and thermal properties of cellulose Fibers isolated from energycane bagasse using alkaline and sodium chlorite treatments.

Chapter 3 describes the morphology, crystallinity and percentage estimation of isolated cellulose I/II hybrid fibers from energycane bagasse during the delignification process.

Chapter 4 presents the formation and characterization of core-shell structured hydrogels and investigates the effect of particle size, aspect ratio and crystal structure of cellulose nanoparticles on hydrogels.

Chapter 5 provides overall conclusions of the dissertation.

1.4 REFERENCES

Aftab, K., Akhtar, K., Jabbar, A., 2014. Batch and column study for Pb-II remediation from industrial effluents using glutaraldehyde–alginate–fungi biocomposites. Ecological Engineering 73, 319-325.

Agarwal, U.P., Zhu, J.Y., Ralph, S.A., 2013. Enzymatic hydrolysis of loblolly pine: effects of cellulose crystallinity and delignification. Holzforschung 67, 371-377.

Berrebi, M., Fabre-Francke, I., Lavédrine, B., Fichet, O., 2015. Development of organic glass using Interpenetrating Polymer Networks with enhanced resistance towards scratches and solvents. European Polymer Journal 63, 132-140.

Bidarra, S.J., Barrias, C.C., Granja, P.L., 2014. Injectable alginate hydrogels for cell delivery in tissue engineering. Acta Biomaterialia 10, 1646-1662.

Cho, S.H., Lim, S.M., Han, D.K., Yuk, S.H., Lm, G.I., Lee, J.H., 2009. Time-Dependent Alginate/Polyvinyl Alcohol Hydrogels as Injectable Cell Carriers. Journal of Biomaterials Science -- Polymer Edition 20, 863-876.

Correa, A.C., Teixeira, E.D., Pessan, L.A., Mattoso, L.H.C., 2010. Cellulose nanofibers from curaua fibers. Cellulose 17, 1183-1192.

Cushing, M.C., Anseth, K.S., 2007. Hydrogel Cell Cultures. Science 316, 1133-1134.

Dragan, E.S., 2014. Design and applications of interpenetrating polymer network hydrogels. A review. Chemical Engineering Journal 243, 572-590.

Gatenholm, P., Klemm, D., 2010. Bacterial Nanocellulose as a Renewable Material for Biomedical Applications. MRS Bulletin 35, 208-213.

Hoi, L.W.S., Martincigh, B.S., 2013. Sugar cane plant fibres: Separation and characterisation. Industrial Crops and Products 47, 1-12.

Hubbell, C.A., Ragauskas, A.J., 2010. Effect of acid-chlorite delignification on cellulose degree of polymerization. Bioresource Technology 101, 7410-7415.

Jao, W.-C., Chen, H.-C., Lin, C.-H., Yang, M.-C., 2009. The controlled release behavior and pH- and thermo-sensitivity of alginate/poly(vinyl alcohol) blended hydrogels. Polymers for Advanced Technologies 20, 680-688.

Kan, B., Lin, B., Zhao, K., Zhang, X., Feng, L., Wei, J., Fan, Y., 2014. Imprinting of bovine serum albumin in a nonwoven polypropylene membrane supported

polyacrylamide/calcium alginate interpenetrating polymer network hydrogel. RSC Advances 4, 55846-55852.

Kim, M., Day, D.F., 2011. Composition of sugar cane, energy cane, and sweet sorghum suitable for ethanol production at Louisiana sugar mills. Journal of Industrial Microbiology & Biotechnology 38, 803-807.

Kumar, V., Reus-Medina, M.D.L., Yang, D., 2002. Preparation, characterization, and tabletting properties of a new cellulose-based pharmaceutical aid. International Journal of Pharmaceutics 235, 129-140.

Lee, K.Y., Mooney, D.J., 2012. Alginate: Properties and biomedical applications. Progress in Polymer Science 37, 106-126.

Lu, J., Askeland, P., Drzal, L.T., 2008. Surface modification of microfibrillated cellulose for epoxy composite applications. Polymer 49, 1285-1296.

Ma, H., Zhou, B., Li, H.S., Li, Y.Q., Ou, S.Y., 2011. Green composite films composed of nanocrystalline cellulose and a cellulose matrix regenerated from functionalized ionic liquid solution. Carbohydrate Polymers 84, 383-389.

Martin, C., Alriksson, B., Sjode, A., Nilvebrant, N.O., Jonsson, L.J., 2007. Dilute sulfuric acid pretreatment of agricultural and agro-industrial residues for ethanol production. Applied Biochemistry and Biotechnology 137, 339-352.

Moubarik, A., Grimi, N., Boussetta, N., 2013. Structural and thermal characterization of Moroccan sugar cane bagasse cellulose fibers and their applications as a reinforcing agent in low density polyethylene. Composites Part B-Engineering 52, 233-238.

Mwaikambo, L.Y., Ansell, M.P., 2002. Chemical modification of hemp, sisal, jute, and kapok fibers by alkalization. Journal of Applied Polymer Science 84, 2222-2234.

Nelson, M.L., O'Connor, R.T., 1964. Relation of certain infrared bands to cellulose crystallinity and crystal lattice type. Part II. A new infrared ratio for estimation of crystallinity in celluloses I and II. Journal of Applied Polymer Science 8, 1325–1341.

Papageorgiou, S.K., Katsaros, F.K., Favvas, E.P., Romanos, G.E., Athanasekou, C.P., Beltsios, K.G., Tzialla, O.I., Falaras, P., 2012. Alginate fibers as photocatalyst immobilizing agents applied in hybrid photocatalytic/ultrafiltration water treatment processes. Water Research 46, 1858-1872.

Park, J.-M., Kim, S.-J., Jang, J.-H., Wang, Z., Kim, P.-G., Yoon, D.-J., Kim, J., Hansen, G., DeVries, K.L., 2008. Actuation of electrochemical, electro-magnetic, and electro-active

actuators for carbon nanofiber and Ni nanowire reinforced polymer composites. Composites Part B: Engineering 39, 1161-1169.

Perez, R.A., Kim, J.-H., Buitrago, J.O., Wall, I.B., Kim, H.-W., 2015. Novel therapeutic core–shell hydrogel scaffolds with sequential delivery of cobalt and bone morphogenetic protein-2 for synergistic bone regeneration. Acta Biomaterialia 23, 295-308.

Samanta, H.S., Ray, S.K., 2014. Synthesis, characterization, swelling and drug release behavior of semi-interpenetrating network hydrogels of sodium alginate and polyacrylamide. Carbohydrate Polymers 99, 666-678.

Seliktar, D., 2012. Designing Cell-Compatible Hydrogels for Biomedical Applications. Science 336, 1124-1128.

Siroky, J., Blackburn, R.S., Bechtold, T., Taylor, J., White, P., 2010. Attenuated total reflectance Fourier-transform Infrared spectroscopy analysis of crystallinity changes in lyocell following continuous treatment with sodium hydroxide. Cellulose 17, 103-115.

Sun, J.-Y., Zhao, X., Illeperuma, W.R.K., Chaudhuri, O., Oh, K.H., Mooney, D.J., Vlassak, J.J., Suo, Z., 2012. Highly stretchable and tough hydrogels. Nature 489, 133-136.

Sun, R.C., Tomkinson, J., Zhu, W., Wang, S.Q., 2000. Delignification of maize stems by peroxymonosulfuric acid, peroxyformic acid, peracetic acid, and hydrogen peroxide. 1. Physicochemical and structural characterization of the solubilized lignins. Journal of Agricultural and Food Chemistry 48, 1253-1262.

Sun, X.F., Sun, R.C., Su, Y.Q., Sun, J.X., 2004. Comparative study of crude and purified cellulose from wheat straw. Journal of Agricultural and Food Chemistry 52, 839-847.

Talebnia, F., Karakashev, D., Angelidaki, I., 2010. Production of bioethanol from wheat straw: An overview on pretreatment, hydrolysis and fermentation. Bioresource Technology 101, 4744-4753.

Thakur, V.K., Thakur, M.K., 2014. Processing and characterization of natural cellulose fibers/thermoset polymer composites. Carbohydrate Polymers 109, 102-117.

Thakur, V.K., Thakur, M.K., Gupta, R.K., 2013a. Rapid synthesis of graft copolymers from natural cellulose fibers. Carbohydrate Polymers 98, 820-828.

Thakur, V.K., Thakur, M.K., Gupta, R.K., 2013b. Synthesis of lignocellulosic polymer with improved chemical resistance through free radical polymerization. International Journal of Biological Macromolecules 61, 121-126.

Thakur, V.K., Thakur, M.K., Gupta, R.K., 2014. Review: Raw Natural Fiber-Based Polymer Composites. International Journal of Polymer Analysis and Characterization 19, 256-271.

Ummartyotin, S., Manuspiya, H., 2015. A critical review on cellulose: From fundamental to an approach on sensor technology. Renewable and Sustainable Energy Reviews 41, 402-412.

Yang, J.-M., Wang, N.-C., Chiu, H.-C., 2014. Preparation and characterization of poly(vinyl alcohol)/sodium alginate blended membrane for alkaline solid polymer electrolytes membrane. Journal of Membrane Science 457, 139-148.

Zhang, Y., Liu, J., Huang, L., Wang, Z., Wang, L., 2015. Design and performance of a sericin-alginate interpenetrating network hydrogel for cell and drug delivery. Scientific Reports 5, 12374.

CHAPTER 2 CELLULOSE FIBERS ISOLATED FROM ENERGYCANE BAGASSE USING ALKALINE AND SODIUM CHLORITE TREATMENTS: STRUCTURAL, CHEMICAL AND THERMAL PROPERTIES[1]

2.1 INTRODUCTION

Cellulose is a polymer that has attracted an extraordinary attention due to its superior performance. Because of its exceptional characteristics of great stiffness and high hydrophilicity, cellulose related materials can be used in tissue engineering scaffolds, filter media, nano sensors, adhesive, skin mask, wound dressing, and functional clothes (Park et al., 2008b; Gatenholm and Klemm, 2010b). The raw materials for manufacturing cellulose are widely considered inexhaustible in nature. Most agricultural wastes, woody plant, forestry residues, herbaceous biomass, cellulose wastes, and municipal solid wastes are a source of cellulose (Martin et al., 2007). One of the crops being considered as a lignocellulose resource for extracting cellulose is energycane. Compared to sugarcane, energycane has lower sucrose content and higher fiber content, implying higher expected cellulose yields in terms of tons of plant material per acre (Kim and Day, 2011). In addition, energycane is cold tolerant and can be grown on fallow land. Additional biomass material can boost the economy for cellulose production (Singh et al., 2014).

Efficient and economic cellulose production is achieved by extracting the maximum amount of cellulose fibers from crops through delignification. The delignification process is generally carried out using acidic, alkaline, or oxidative methods (Bussemaker and Zhang, 2013). However, the above methods face some problems, such as high processing costs and larger power requirement. For example, a limiting factor for acid hydrolysis and organic solvent pretreatment is the costs of chemical recovery. Supercritical fluids process and mechanical

[1] Reprint in part with permission from Industrial Crops and Products
Yue Y.Y., Han J.Q., Han G.P., Aita G.M., Wu Q.L. 2015. Cellulose Fibers Isolated from Energycane Bagasse using Alkaline and Sodium Chlorite Treatments: Structural, Chemical and Thermal Properties. Industrial Crops and Products 76, 355-363.

pretreatments are less favored because of high energy consumption (Talebnia et al., 2010; Aita and Kim, 2011).

NaOH treatment, an efficient method to dissolve non-cellulosic components by cleaving the α- and β-aryl ether linkages between lignin and hemicellulose, has been used as an initial step for cellulose isolation (Li et al., 2007; Singh et al., 2014). Mwaikambo (2002) reported the extraction of cellulose from hemp, sisal, jute, and kapok fibers with the same NaOH treatment. In Corrêa's study (2010), curaua fibers were pretreated by 5wt% and 17.5wt% aqueous NaOH solution at 70 ℃ and the lignin contents of treated fibers were reduced by 0.5wt% and 5.1wt%, respectively. Since NaOH may not achieve complete lignin removing (Talebnia et al., 2010), a further delignification process is needed.

Acidified-$NaClO_2$ is an established laboratory method for lignin removal (Hubbell and Ragauskas, 2010). Jungnikl et al. (2008) employed the acidified $NaClO_2$ pretreatment method to extract pure cellulose from softwoods. Hubbell et al. (2010) investigated the effect of $NaClO_2$ on pure cellulose in the presence of incorporated lignin and proved the reaction between lignin and $NaClO_2$. Under acidic conditions, $NaClO_2$ degrades into chlorite anion (ClO_2^-) and ultimately chloride anion (Cl^-) which solubilizes the lignin components.

Few researchers have focused on the impact of a combination of NaOH and $NaClO_2$ treatments on energycane bagasse. Furthermore, the properties of isolated cellulose fibers, such as morphology, cellulose reactivity, structure and thermal stability may change through different NaOH/$NaClO_2$ treatments (e.g., treatment time, the amount and concentration of chemicals). For example, Ben Sghaier et al. (2012) reported a modification of cellulose surface topography for *Agave americana* L. fiber during NaOH delignification. The extensive delignification of pure cellulose via the $NaClO_2$ method can affect cellulose's degree of polymerization (DP) (Hubbell

and Ragauskas, 2010). In addition, the effects of delignification are largely related to the properties of native energycane bagasse fibers, because the lignin content in energycane bagasse is highly variable (Hoi and Martincigh, 2013).

In the present study, cellulose fibers were extracted from energycane bagasse using a $NaOH/NaClO_2$ treatment. Different treatment conditions were applied to efficiently break down the carbohydrates–lignin complex in energycane bagasse. The major objective was to compare the non-cellulosic components, yield, crystallinity, and thermal stability of isolated ligno-cellulose fibers under different treatment conditions. To investigate the structural features and chemical reactivity of the obtained lignocellulose during the extraction process, compositional analysis, UV absorption, SEM, FTIR, and thermal degradation techniques were carried out, providing a fundamental guidance of delignification treatments on the properties of energycane bagasse fibers.

2.2 MATERIALS AND METHODS

2.2.1 Materials

Energycane bagasse (HO 02-113), supplied by the Audubon Sugar Institute at Louisiana State University Agricultural Center, St. Gabriel, LA, was oven-dried at 40 ℃ for 48h and milled to pass through a 2.0 mm screen (10-mesh sieve). Sodium chlorite (80%) and acetic acid (glacial, 99.85%) were obtained from Sigma-Aldrich Inc. (St. Louis, MO, USA) and Sodium Hydroxide (98.9%, ACS grade) was purchased from Fisher Scientific Inc. (Fair Lawn, NJ, USA). All reagents and solvents were of analytical grade. Distilled water was used in the preparation of all solutions.

2.2.2 Isolation of Cellulose

Twenty grams of energycane bagasse (dry weight) were soaked in 70 ℃ water for 2h and then washed with distilled water. The obtained lignocellulose fibers were treated with NaOH at different conditions (10wt% for 1.5h, 20wt% for 1.5h and 20wt% for 10h) at 98 ℃. The mixtures were then filtered, and the obtained slurry was washed repeatedly with distilled water until a neutral pH was reached. Each sample was dried at 40 ℃ for 48h to determine the cellulose yield and sample composition.

Because of the incomplete isolation of pure cellulose, $NaClO_2$/glacial CH_3COOH treatments were further applied to the NaOH treated samples. The mass ratio of $NaClO_2$ to the fibers was 0.75:1 and the volume ratio of CH_3COOH to suspension was 1:50. The mixture was heated in an oil bath at 75 ℃ for 2h. During the period of two hours, $NaClO_2$ and CH_3COOH were added every half hour to keep the pH less than 4.0. The samples were washed extensively until a neutral pH was reached. If the obtained slurry was not pure white, the addition of $NaClO_2$/glacial CH_3COOH mixture was repeated. The final white samples were oven-dried at 40 ℃ for 48h. The diagram for cellulose extraction procedure is shown in Figure 2.1.

The original bagasse fibers were labeled as B0, and the samples after NaOH treatment were designated as Bxy with x= 10, 20 (NaOH concentration/wt%) and y=1.5, 10 (reaction time/hour). For example, the sample reacted with 10wt% NaOH solution for 1.5h was designated as B101.5. Similarly, samples after NaOH/$NaClO_2$ treatment were designated as Bxys. Thus, B101.5 became B101.5s after $NaClO_2$ treatment.

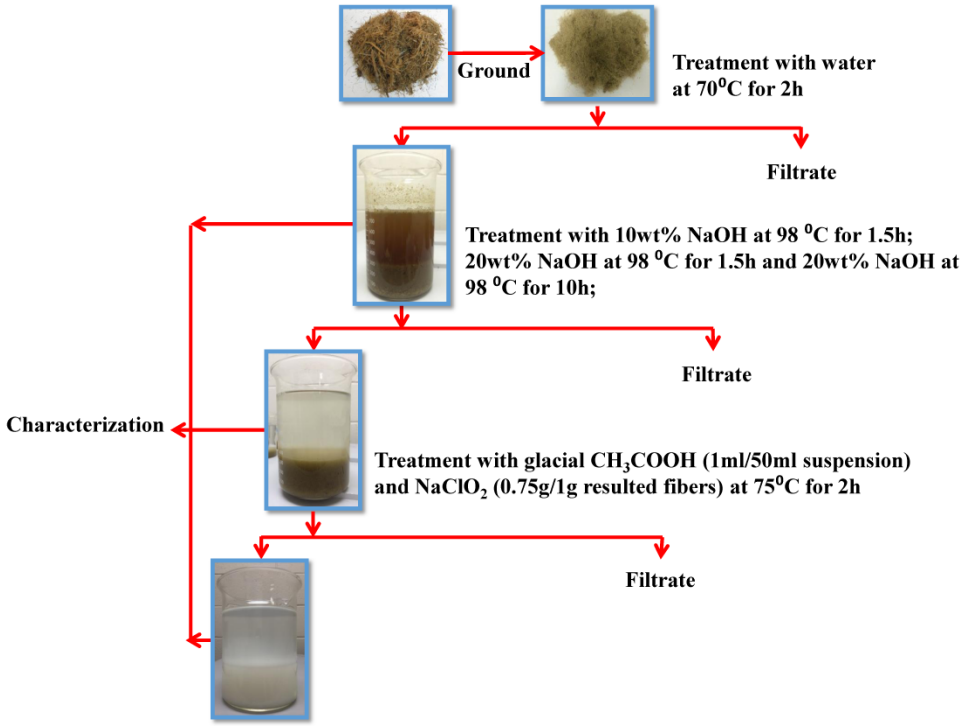

Figure 2.1 Scheme for extraction of cellulose from bagasse fiber

2.2.3 Characterizations

2.2.3.1 Compositional Analysis

Prior to each measurement, all the samples were conditioned at 40 ℃ for 48 h. Compositional analysis was carried out according to the Laboratory Analytical Procedures (LAPs #42618, 42619, 42622) of National Renewable Energy Laboratory (NREL). The NREL reference material (8491 sugarcane bagasse) was analyzed as an internal standard to ensure the accuracy of the procedures. The yield of lignocellulose was calculated by dividing the weight of treated samples by the dry weight of raw materials.

2.2.3.2 UV Absorbance

UV spectra were recorded using a UV-vis spectrophotometer (Evolution 600 PC, Thermo Electron Co., Waltham, MA, USA). Each sample was extracted with the ethanol/benzene solvent and then dissolved in the LiCl/DMSO system.

Five grams of sample (B0, B101.5, B201.5 N2010, B101.5s, B201.5s and B2010s) were each extracted with 100ml of ethanol/benzene solvent (1:2, v/v) in a flask reactor with a reflux condenser for 8h. The reaction was conducted at 85℃ to keep the liquid stable at boiling. After extraction, the fibers were washed with distilled water and filtered through a Büchner funnel. The dried fibers were placed in a refrigerator at -20℃ for 8h.

The LiCl/DMSO solvent was prepared by adding 8wt% of oven-dried LiCl to DMSO under continuously magnetic stirring at 20℃ (Wang et al., 2009). Approximately 1.0wt% of the prepared fibers were dissolved in the LiCl/DMSO system and stirred for 5 days.

The prepared solutions were placed into a UV quartz cuvette with PTFE cover (dimension of 45 ×12.5× 12.5 mm). Each measurement was carried out in the spectral range of 400-800 nm with a scan speed of 240nm/min at 20℃. LiCl/DMSO at 8wt/v% was used as reference. The optical absorbance of each solution was measured three times at 20℃. The mean absorbance of each sample was calculated by averaging the absorbance over the wavelength ranging from 400 to 800 nm.

2.2.3.3 Environmental Scanning Electron Microscope (ESEM)

Oven dried lignocellulose fibers were placed on the aluminum stubs with conductive carbon tape. The samples were coated with gold using the sputtering technique for 2 min. The micrographs of the bagasse before and after various delignification treatments were captured using ESEM (FEI Quanta 200 F, Hillsboro, OR, USA) microscope with an accelerating voltage of 12.5kV. For each sample, around 20 fibers were randomly selected and measured from ESEM images. Fiber width defined as the dimension perpendicular to its long axis was measured using Image J software (http://imagej.nih.gov/ij/, 1997-2011).

2.2.3.4 Fourier Transform Infrared Spectrometry (FTIR)

FTIR measurements were performed using Bruker FTIR analyzer (Tensor-27, Bruker Optics Inc., Billerica, MA, USA) in the range of 4000 to 600cm^{-1} with 64 repetitious scans. The resolution for the spectra was 4cm^{-1}. All samples were dried in an oven at 40 ℃ for 48h and cooled to 20 ℃ before placing them in the sample chamber. Three replicated measurements were recorded for each condition.

2.2.3.5 Thermal Degradation

The dehydration and degradation behavior of bagasse fibers were characterized through thermo-gravimetric (TG) analysis with a TA Q50 Analyzer (TA Instruments, New Castle, DE, USA). Purified nitrogen at a flow rate of 60ml/min was used as the carrier gas to prevent any thermo-oxidative degradation. The sample weight was in the range of 3-5g to mitigate the difference of heat and mass transfer. Before the data acquisition segment, each sample was equilibrated at 30 ℃ for 4min to obtain an isothermal condition. The specimen was then heated from 30 to 600 ℃ at a rate of 10 ℃ /min. Each measurement was repeated three times.

The weight-loss rate was obtained from derivative thermogravimetric (DTG) data. Weight losses or derivative weights vs. temperature thermograms were employed to exhibit the different decomposition processes. The onset degradation temperature (T_0, ℃) was defined as the intersection of tangents drawn from thermo-gravimetric curve, one before inflection caused by the degradation and another from the cellulose degradation step. The maximum thermal degradation temperature (T_{max}, ℃), the maximum weight loss rate (WLR_{max}, %/℃) and char yields (CY, %) were used to analyze the thermal stability of bagasse fibers.

2.3 RESULTS AND DISCUSSION

2.3.1 Chemical Composition and Yield of Lignocellulose

The chemical composition and aqueous dispersion state of the raw and treated energycane bagasse are summarized in Table 2.1 and in Figure 2.2a, respectively. After NaOH treatment, the color of the fibers in water was changed from dark brown to yellow, suggesting the reducing amount of lignin. According to Table 2.1, the lignin contents of B101.5, B201.5 and B2010 were reduced by 6.37, 7.12 and 8.79wt%, and their hemicellulose content were decreased by 13.52, 15.93 and 20.18wt%, respectively. The large amount of decreasing in hemicellulose was due to the disruption and breaking of hydrogen bonds through NaOH treatment (Hubbell and Ragauskas, 2010). In addition, the contents for extractive and ash were also reduced to ≤1wt%.

Table 2.1 Chemical composition of lignocellulose from energycane bagasse

Sample	Cellulose (%)	Hemicellulose (%)	Lignin (%)	Extractive (%)	Ash (%)
B0	43.10	22.82	24.09	2.13	1.96
B101.5	65.14	9.30	17.72	1.03	0.38
B201.5	68.36	6.89	16.97	0.93	0.25
B2010	72.20	2.54	15.30	0.89	0.08
B101.5s	72.57	7.41	8.31	0.04	0.23
B201.5s	76.49	3.83	6.78	0.05	0.11
B2010s	84.12	2.37	6.48	0.05	0.06

Note: B0- raw fibers; B101.5, B201.5 and B2010- NaOH treated bagasse fibers (designated as Bxy with x= 10, 20 (NaOH concentration/wt%) and y=1.5, 10 (reaction time/hour)); B101.5s, B201.5s and B2010s- NaOH/$NaClO_2$ treated bagasse fibers (designated as Bxys)

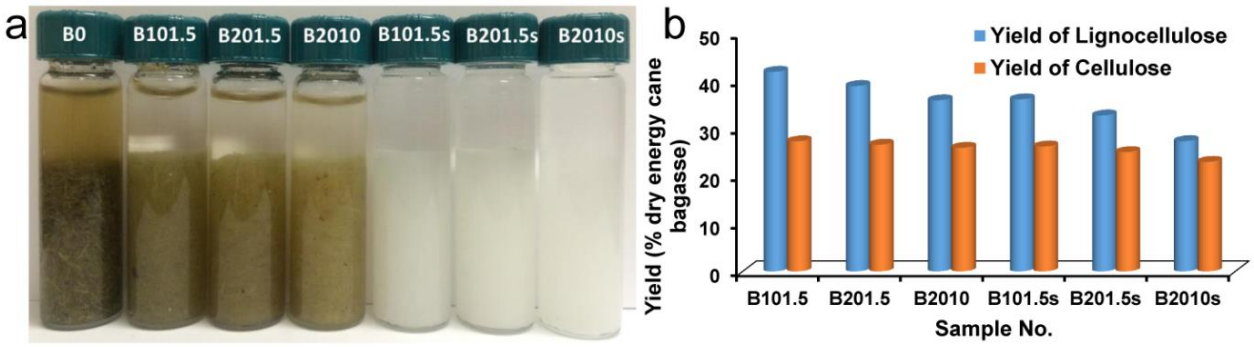

Figure 2.2 Dispersion states of raw fibers (B0), NaOH treated fibers (B101.5, B201.5 and B2010) and NaOH/$NaClO_2$ treated fibers (B101.5s, B201.5s and B2010s) in water (a), and the yield of lignocellulose and pure cellulose (b)

It was found that hemicellulose and lignin could not be thoroughly removed by the pure NaOH treatment. To further eliminate the residual lignin, the NaOH treated samples were then subjected to a $NaClO_2$ treatment. After acidified $NaClO_2$ treatment, B101.5s, B201.5s and B2010s became pure white without any trace of dark lignin residue and their lignin contents were reduced to 6 - 9wt%. The reason for the decreasing of lignin and hemicellulose was that $NaClO_2$ reacted with lignin and resulted in aromatic substitution, the displacement of side chains in acidic environment (Sun et al., 2004a). The final white fibers contained a small amount of lignin which was in accordant with Hubbell's observations that the cellulose appeared white with up to 10wt% lignin (Hubbell and Ragauskas, 2010). In addition, the contents of extractive and ash for B101.5s, B201.5s and B2010s were extremely low because of water and alcohol extraction.

Compared with B101.5s and B201.5s, B2010s removed more non-cellulosic material. There was 20.45wt% and 17.61wt% reduction of hemicellulose and lignin for B2010s. And the amount of hemicellulose and lignin was reduced by 15.41wt% and 15.78wt% for B101.5s and 18.99wt% and 17.31wt% for B201.5s, respectively, indicating that harsh NaOH/$NaClO_2$ treatment significantly eliminated non-cellulosic components.

As shown in Figure 2.2b, after the NaOH treatment, the lignocellulose yield decreased from 42.04wt% (B101.5) to 36.02wt% (B2010), as result of the higher NaOH concentration and longer treatment time. After $NaClO_2$ treatment, because of the further reduction of hemicellulose and lignin contents, the lignocellulose yield was decreased to 36.20wt% for B101.5s and 27.40wt% for B2010s, which were lower than the values for the corresponding samples without $NaClO_2$ treatment.

Compositional analysis revealed that the raw bagasse fibers had 43.10wt% cellulose, and the yield of cellulose was reduced by 15.74, 16.44 and 17.10wt% for sample B101.5, B201.5 and B2010, respectively. After treated by $NaClO_2$, the content of celluloses was further decreased to 26.23, 25.09, 23.05wt% for sample B101.5s, B201.5s, B2010s. The possible reason for the reduction of cellulose yield was that part of glycosidic bonds were cleaved during NaOH/$NaClO_2$ treatments, leading to the de-polymerization of polysaccharides.

2.3.2 Lignin Content by UV Absorbance

Figure 2.3 shows the dispersion state of lignocellulose solutions at the concentrations of 1.0wt% in the LiCl/DMSO solvent and the UV absorbance spectra of all the samples at a visible wavelength range of 400 to 800 nm. The mean absorbance (Ab) of lignocellulose solutions largely depends on lignin amount and the compatibility of lignocellulose fibers in LiCl/DMSO solvent. All the lignocellulose fibers after extraction formed highly homogenous transparent solutions, suggesting an excellent compatibility of lignocellulose fibers in 8wt% LiCl/DMSO solvent. Thus the Ab values of all the samples depended on their lignin content.

Due to the presence of large amount of lignin, B0 with an average absorbance value of 2.32 exhibited a dark brown color. Compared with the other samples, the higher absorbance value in B0 reflected the larger amount of lignin because the UV light could cleavage the band in

lignin as well as lignin-carbohydrate linkages, resulting in the large molecular vibrations in B0 (Sun et al., 2000a). After alkali treatment, the color of B101.5, B201.5 and B2010 turned from dark brown to bright yellow, suggesting that the alkali treatment removed lignin and impurities. The mean Ab values decreased from 2.32 for B0 to 0.90, 0.79 and 0.67 for B101.5, B201.5 and B2010, respectively. Compared with B101.5 and B201.5, B2010 had a lower absorbance, indicating that the amount of lignin decreased with increase of alkali concentration and reaction time. After a further $NaClO_2$ treatment, B101.5s, B201.5s and B2010s exhibited white color, suggesting successful isolation of pure cellulose. The mean Ab values of B101.5s, B201.5s and B2010s reduced to 0.57, 0.48, and 0.41, respectively. Among all the samples, B2010s with the smallest mean Ab value had the lowest lignin content. These conclusions were in accordance with the results observed in the composition analysis section.

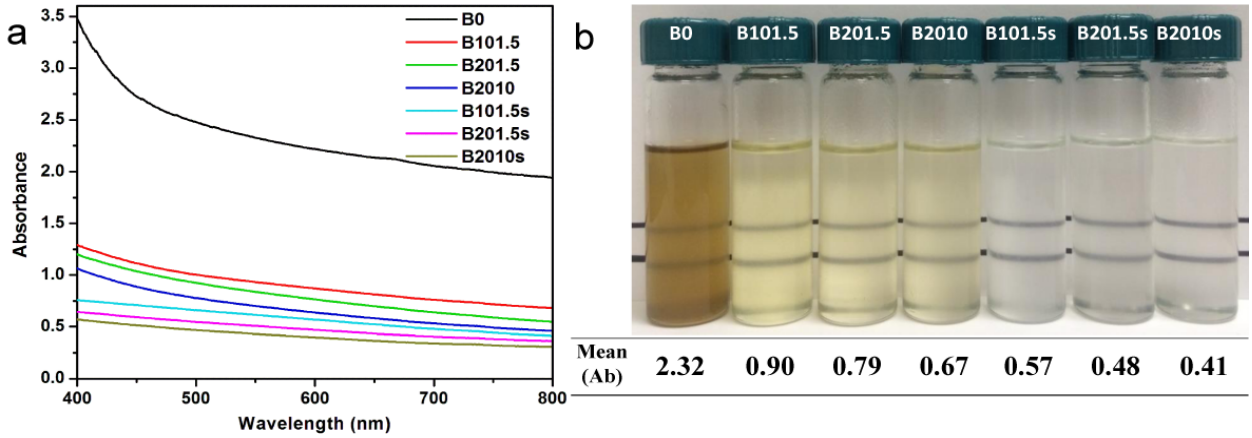

Figure 2.3 UV absorbance spectra (a) and dispersion state of raw fibers (B0), NaOH treated fibers (B101.5, B201.5 and B2010) and NaOH/$NaClO_2$ treated bagasse fibers (B101.5s, B201.5s and B2010s) in 8wt% LiCl/DMSO solvent system with 1wt% concentration after 5days of stirring (b)

2.3.3 Fiber Morphology by ESEM

The structural features of bagasse fibers before and after NaOH and $NaClO_2$ treatments are shown in Figure 2.4.

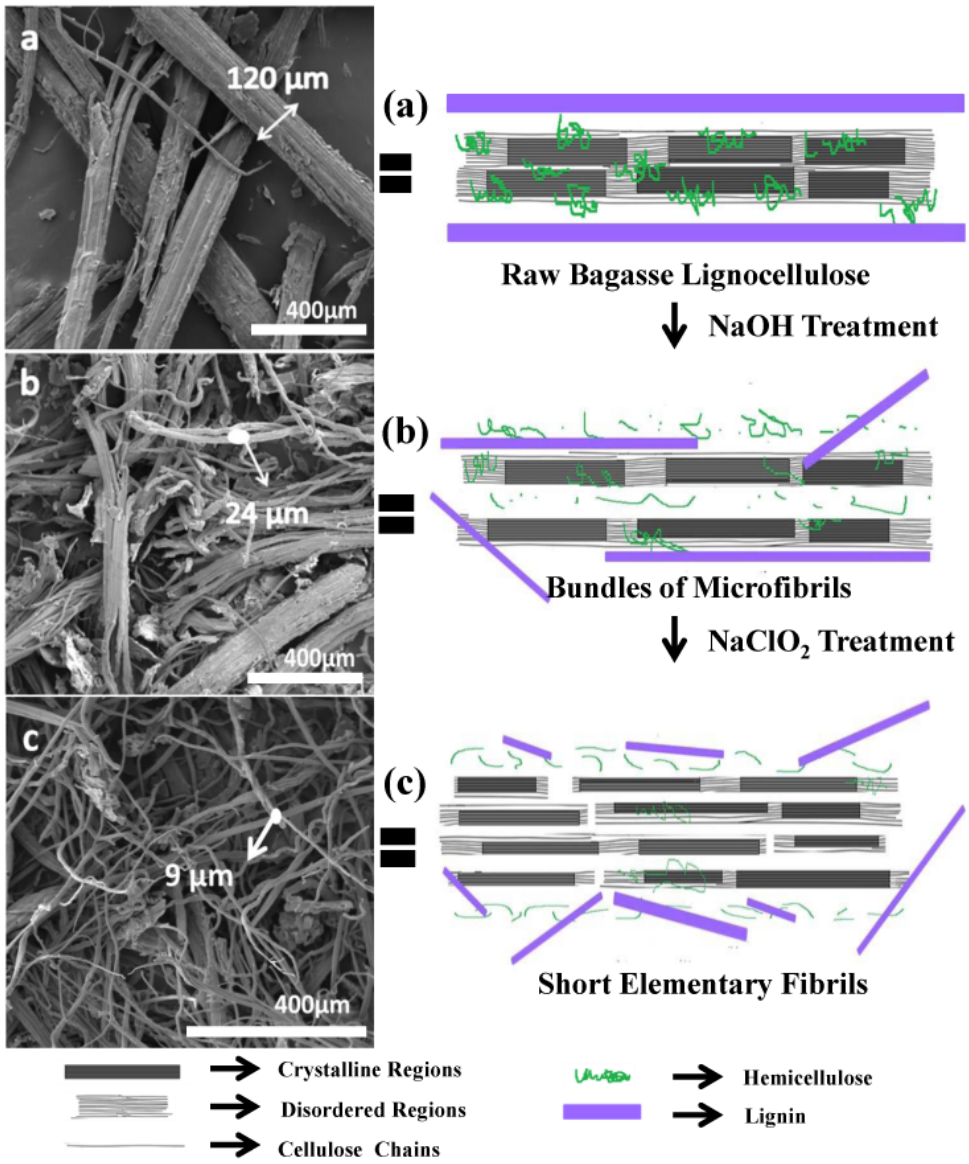

Figure 2.4 ESEM images of raw fibers (a), the fibers treated with 20% NaOH for 10h (b), the fiber treated with 20% NaOH for 10h and $NaClO_2$ for 2h (c) and the schematic of defibrillation.

The native bagasse fiber bundles (B0) present a rigid and smooth surface with an average width of 137±46µm (Figure 2.4a) due to the existence of lignin and waxes. In plant cell walls, hemicellulose and lignin are clustered around cellulose fiber bundles. The highly ordered crystalline regions of the fibers are constituted by several cellulose microfibrils aligned in the fiber axis direction (Mandal and Chakrabarty, 2011; Ben Sghaier et al., 2012). After the NaOH treatment, the diameter of fiber bundles was decreased to 47±40µm (Figure 2.4b). It is well

known that lignin acts as "glue" and it strengthens cell walls. Without lignin, a highly branched and complex polymer with aromatic constituents, the cell walls are partly collapsed (Goshadrou et al., 2011). NaOH can dissolve the inter-fibrillar or bulk lignin and then disrupt the initial fiber structure, leading to the disaggregation of micro-fibrils from their neighbor fibers (Rezende et al., 2011). After a further $NaClO_2$ treatment, the fibers are broken down in both their radial and axial directions, leading to a more uniform fiber distribution with less vacant area (Rezende et al., 2011). Therefore, the average diameter of individual fibers was further reduced to 12±5μm, and the final cellulose fibers showed round, fine and long characteristics (Figure 2.4c).

2.3.4 Lignocellulose Structure and Crystallinity by FTIR

The FTIR spectra in the finger print region of 1800-1200 cm^{-1} are shown in Figure 2.5a. For all of the samples, the band at 1632cm^{-1} assigned to the O−H bending of adsorbed water had almost the same absorbance, indicating that the cellulose-water interaction was difficult to be destroyed by the delignification treatments (Han et al., 2013d).

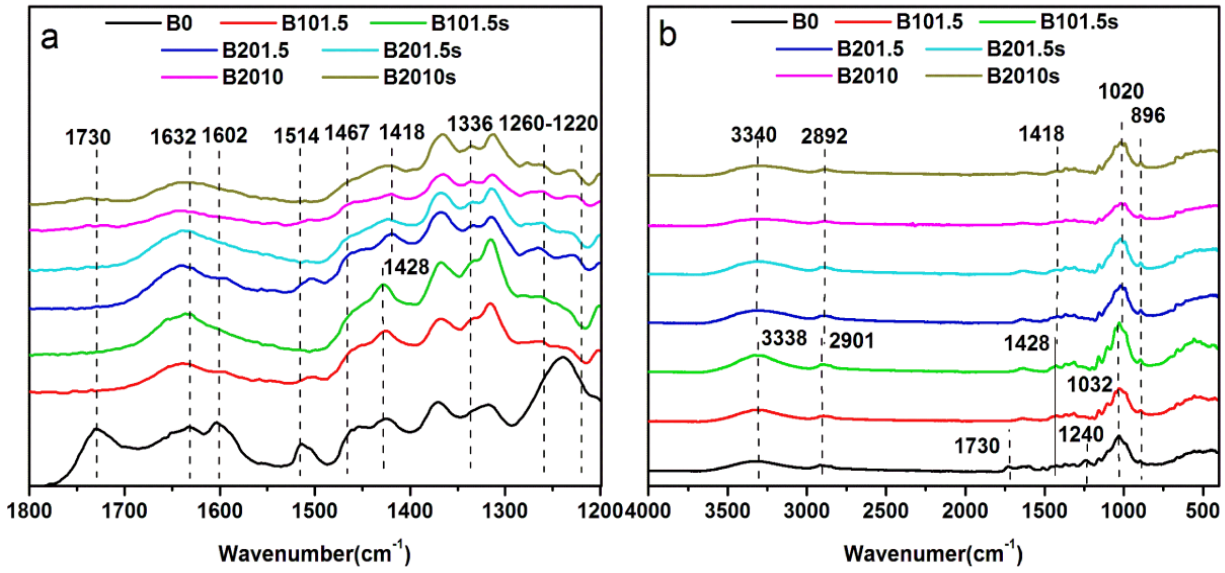

Figure 2.5 The raw fibers (B0), NaOH treated bagasse fibers (B101.5, B201.5 and B2010) and $NaOH/NaClO_2$ treated bagasse fibers (B101.5s, B201.5s and B2010s) with the wavenumber ranges of 1800-1200 cm^{-1} (a), and with the wavenumber ranges of 4000-500 cm^{-1} (b).

Compared to the treated samples, B0 presents higher intensities of absorbance peaks assigned to $–CH_3$, –COOH and C=O stretching (aromatic ring) compounds (Mwaikambo and Ansell, 2002; Khan et al., 2004; Yang et al., 2007a; Corredor et al., 2009), indicating that B0 contained high amounts of lignin.

Upon $NaOH/NaClO_2$ treatment, most of the lignin was removed as indicated by the reduction in intensity of the lignin-associated peaks. For instance, the peak between 1740 and 1710 cm^{-1} disappeared because of the removal of esters from carboxylic groups (Mwaikambo and Ansell, 2002; Jungnikl et al., 2008). The bands related to lignin aromatic ring (guaiacyl and syringyl rings) vibrating at 1602 and 1514 cm^{-1} decreased (Sun et al., 2000a; Sun et al., 2004a; Corredor et al., 2009). The broad band within the range of 1220cm^{-1} and 1260cm^{-1} originated from the C–O stretching in guaiacyl ring was significantly decreased (Khan et al., 2004). The band at 1467 cm^{-1} related to methyl group deformation and the aromatic ring vibrations was reduced (Sun et al., 2000a; Khan et al., 2004).

The measured FTIR characteristic bands of raw and mercerized bagasse fibers over the entire range are shown in Figure 2.5b. Compared with 10wt% alkali treated samples (B101.5 and B101.5s), B201.5, B201.5s, B2010 and B2010s treated with a higher NaOH concentration (20wt%) exhibited a significant change in site and absorbance intensity. Many characteristic bands were shifted at the maximum peak value. For example, the bands at 3338, 2901, 1428, 1371, 1316, 1161, 1032, 993 and 896 cm^{-1} were shifted to 3340, 2892, 1418, 1368, 1314, 1159, 1020, 996 and 894 cm^{-1}, respectively. In addition, compared with B101.5 and B101.5s, smaller intensities were observed in B201.5, B201.5s, B2010 and B2010s. These changes suggest the altering of intra and intermolecular hydrogen bonds and the conversion of cellulose crystal

structure (Yue et al., 2012b). It should be noted that B2010 had the smallest intensity, indicating its greatest extent of crystal structure transition.

The absorption bands at 1428 cm^{-1} and 896 cm^{-1} reflected crystalline regions and amorphous regions, respectively (O'Connor et al., 1958). It was reported that cellulose molecule chain vibrated differently in crystalline region and amorphous area, and both of the two absorption bands were greatly influenced by cellulose crystal structure. Thus, the ratio of the intensities of these two bands was defined as an empirical ‘‘crystallinity index’’, and it was termed as the ‘‘Lateral Order Index’’ (LOI)”. Generally, crystallinity decreases with decreasing LOI values (Oh et al., 2005; Kljun et al., 2011).

An empirical index “Hydrogen Bond Intensity (HBI)”, which compares the ratio of absorption bands at 3338 cm^{-1} and 1336 cm^{-1}, was introduced to study the changes of hydrogen bonding between certain hydroxyl groups in cellulose (Oh et al., 2005). The bands at 3338 cm^{-1} and 1336 cm^{-1} were closely related to crystalline cellulose and intra-, inter- molecular regularity (Oh et al., 2005; Siroky et al., 2010). Generally, crystallinity decreases with increasing HBI values (Kljun et al., 2011). Therefore, LOI and HBI were employed to interpret the qualitative changes in crystallinity for all the samples.

The values of LOI and HBI for the ligno-cellulosic samples are shown in Table 2.2. Compared with B101.5, B0 exhibited a smaller LOI value and larger HBI value, indicating that B0 possessed a lower crystallinity value.

The LOI values from B101.5 to B201.5 decreased and then the value increased for B2010. This phenomenon can be explained as follows. When NaOH ≤ 10wt%, no crystal transformation occurred and cellulose molecular maintained a highly ordered parallel arrangement, leading to a high LOI value for B101.5 (Yue et al., 2012b). Whereas when NaOH concentration = 20wt%,

the conversion began with the formation of Na-cellulose I. Na^+ ions broke the inter-molecular hydrogen bonds between the lattice planes, leading to the transition from the parallel-chain structure of Na-cellulose I to the antiparallel-chain structure characteristic of Na-cellulose II (Gwon et al., 2010). As a result, the LOI value of B201.5 decreased. When the treatment time was increased to 10h, any changes in structure were limited as Na cellulose II had no available inter- or intra-molecular hydrogen bonding. Finally, cellulose II with anti-parallel chains was achieved by rinsing process to remove Na^+, resulting in an increased LOI value of B2010.

Table 2.2 Crystallinity data of ligno-cellulosic fibers

Sample	LOI[a]	HBI[b]
B0	0.52	1.65
B101.5	0.63	1.49
B201.5	0.50	1.47
B2010	0.52	1.18
B101.5s	0.61	1.75
B201.5s	0.47	1.75
B2010s	0.47	1.36

[a] Lateral Order Index, calculated using the ratio of the absorption bands at 1428 cm^{-1} and 896 cm^{-1}

[b] Hydrogen Bond Intensity, calculated using the ratio of the absorption bands at 3338 cm^{-1} and 1336 cm^{-1}

Note: B0- raw fibers; B101.5, B201.5 and B2010- NaOH treated bagasse fibers (designated as Bxy with x= 10, 20 (NaOH concentration/wt%) and y=1.5, 10 (reaction time/hour)); B101.5s, B201.5s and B2010s- NaOH/$NaClO_2$ treated bagasse fibers (designated as Bxys)

From B101.5 to B2010, the decreasing HBI values suggested that the degree of intermolecular regularity was increased during the conversion process. In addition, at a higher NaOH concentration level for a longer treatment time, HBI values of B2010 and B2010s were smaller than those of the other samples, indicating that the interaction among inter- or intra-

molecular chains in B2010 and B2010s became stronger. The result was probably attributed to the different ultra-molecular structure of polymorphic forms and different polarity of chains between cellulose I and II.

After $NaClO_2$ treatment, B101.5s, B201.5s and B2010s exhibited lower LOI and higher HBI values than the samples without $NaClO_2$ treatment, suggesting that B101.5s, B201.5s and B2010s contained less crystalline structures and more available hydroxyl groups. It was thus concluded that $NaClO_2$ treatments destroyed a portion of crystalline region and inter- and/or intramolecular hydrogen bonding. It should be noted that although the LOI and HBI indices provided a possible way to qualitatively study the cellulose crystallinity, the values cannot be used as for quantitative predictions because of the complexity of the cellulose transition.

2.3.5 Thermal Stability by TG

TG and DTG curves of raw and treated samples are illustrated in Figure 2.6. Table 2.3 lists onset degradation temperature (T_0, ℃), maximum thermal degradation temperature (T_{max}, ℃), maximum weight loss rate (WLR_{max}, %/℃) and char yields (CY, %) at 600 ℃ for all the samples.

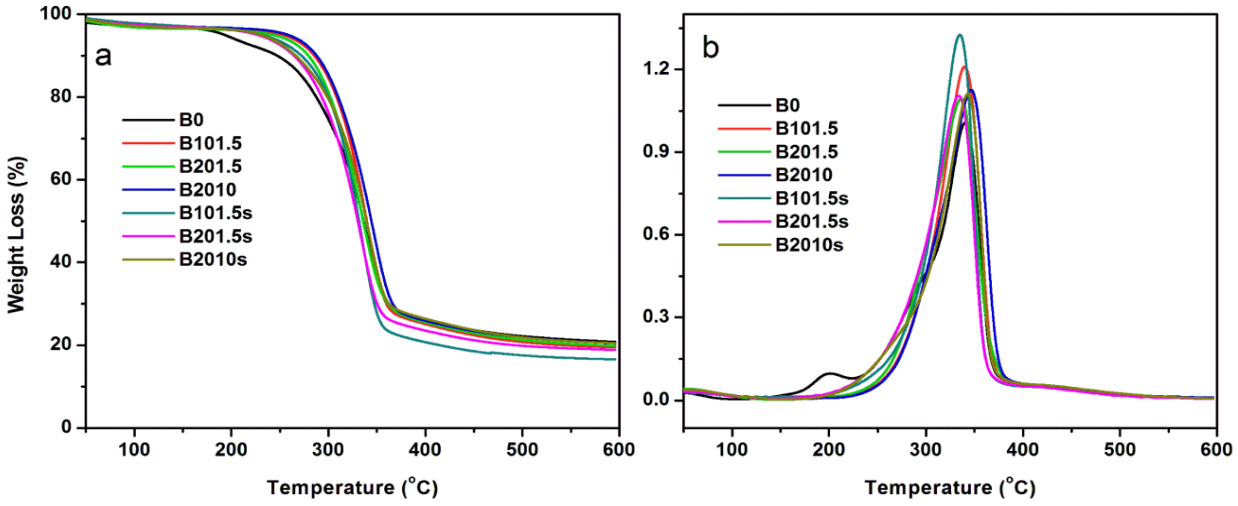

Figure 2.6 TGA (a) and DTG (b) curves of raw fibers (B0), NaOH treated bagasse fibers (B101.5, B201.5 and B2010) and NaOH/$NaClO_2$ treated bagasse fibers (B101.5s, B201.5s and B2010s).

Table 2.3 Summary of thermal de-compositional variables during pyrolysis processes

Sample	T_0 (℃)[a]	Stage I		Stage II		Stage III		CY (%)[d]
		T_{max} (℃)[b]	WLR_{max} (%. ℃$^{-1}$)[c]	T_{max} (℃)	WLR_{max} (%. ℃$^{-1}$)	T_{max} (℃)	WLR_{max} (%. ℃$^{-1}$)	
B0	289.2	200.9	0.10	294.6	0.35	340.0	0.99	20.81
B101.5	300.3	-	-	-	-	342.7	1.18	19.36
B201.5	292.8	-	-	-	-	335.9	0.91	19.83
B2010	303.4	-	-	-	-	346.3	1.00	20.48
B101.5s	295.2	-	-	-	-	335.1	1.33	16.61
B201.5s	287.5	-	-	-	-	333.3	1.01	18.86
B2010s	295.3	-	-	-	-	342.8	1.03	20.48

[a] Onset degradation temperature
[b] Maximum thermal degradation temperature
[c] Maximum weight loss rate
[d] Char yields at 600 ℃
Note: B0- raw fibers; B101.5, B201.5 and B2010- NaOH treated bagasse fibers (designated as Bxy with x= 10, 20 (NaOH concentration/wt%) and y=1.5, 10 (reaction time/hour)); B101.5s, B201.5s and B2010s- `NaOH/$NaClO_2$ treated bagasse fibers (designated as Bxys)

For all the samples, a small initial weight loss was observed at a low temperature (<200 ℃), corresponding to evaporation of loosely bound moisture (Moran et al., 2008; Correa et al., 2010). Due to the hygroscopic nature of the lignocellulose fibers, the amount of physically absorbed water was highly correlated with the ambient humidity and the sample treatment procedures (Hoi and Martincigh, 2013).

At 200 ℃, the DTG curve exhibited several pyrolysis processes (one separated peak and two overlapping peaks) for B0, suggesting the presence of various components (Moran et al., 2008). The initial weight loss observed in the range of 146.9-258.6 ℃ (Table 2.3) was attributed to the beginning of lignin decomposition. The second pyrolysis process ranged from 225.1-

312.6 ℃ with T_{max} at 294.6 ℃ and it was related to the degradation of hemicellulose. The maximum weight loss occurred at high temperature range of 288.3-368.7 ℃ with WLR_{max} of 0.99%/ ℃ which corresponded to the pyrolysis of cellulose. Lignin decomposition was contributed to all the pyrolysis processes due to its wide temperature range of degradation. These results are in agreement with published information in that weight loss of lignin, hemicellulose and cellulose occurs in the range of 160-900 ℃, 220-315 ℃ and 315-400 °C, respectively (Yang et al., 2007a; Moran et al., 2008). The differences in thermal behaviors can be attributed to the different chemical structure of cellulose, hemicellulose and lignin. Compared to cellulose, an ordered polymer of glucose, hemicellulose with a random and amorphous structure is easier to decompose at a lower temperature (Yang et al., 2007a; Hoi and Martincigh, 2013). Lignin is made up of the aromatic rings with various branching structures, the decomposition of the chemical bonds in lignin starts at 200 ℃ and continues up to 600 ℃, which resulting in the degradation of lignin with no maximum weight loss rate occurring in the whole temperature range (Yang et al., 2007a; Moran et al., 2008; Hoi and Martincigh, 2013). When temperature reached 600 ℃, most of the hemicellulose and cellulose were decomposed. Therefore, the high CY (20%) attributed to the un-completing pyrolysis of lignin.

For NaOH treated samples, a unique peak was observed in the range of 230–370 ℃, indicating that most lignin and hemicellulose were removed. Among all of the NaOH treated samples, B2010 showed a remarkable thermal stability, followed by B101.5; whereas B201.5 exhibited relatively lower decomposition temperatures. It was reported that the pyrolysis characteristics were closely correlated with the changes in crystalline structure (Liu and Hu, 2008). At NaOH=10wt%, the concentration of Na^+ ions was too low to form enough Na-cellulose I that allowed for swelling of the fibers. Therefore, B101.5 kept cellulose I structure.

When NaOH ≥ 20wt%, fibril swelling and partial destruction of the amorphous region occurred, resulting in the reduction of degradation temperatures for B201.5. After the NaOH treatment time increased to 10 hour, a new crystalline lattice was formed by a rearranging process, leading to a better thermal behavior for B2010.

For both raw and NaOH treated fibers, CY values at 600 ℃ were around 20%. Changes in solid residue were negligible due to the presence of lignin.

After $NaClO_2$ treatment, B101.5s, B201.5s and B2010s showed one dominating pyrolysis curve which ranged from 200-365 ℃, indicating the purity of cellulose structure. An initial weight loss at low temperature (<200 ℃) was attributed to the departure of physically absorbed water (Yang et al., 2007a; Hoi and Martincigh, 2013). Compared with B101.5s and B201.5s, a small shoulder on the left peak was observed in B2010s, suggesting the presence of amorphous and branched oligomer. This observation can be attributed to the de-polymerization of cellulose to lower molecular weight sugars under severe treatment conditions. It should be noted that although de-polymerization occurring in B2010s, T_0, T_{max}, WLR_{max}, and CY values for B2010s were higher than those for B201.5s and B101.5s (Table 2.3), indicating B2010s had the most stable structure among three NaOH/$NaClO_2$ treated samples.

In addition, compared with the corresponding NaOH treated fibers, B101.5s, B201.5s and B2010s had a lower thermal stability. This means that $NaClO_2$ treatment increased the chances of cellulose chain degradation (Hubbell and Ragauskas, 2010).

2.4 CONCLUSIONS

Cellulose fibers were successfully isolated from energycane bagasse by using a combined NaOH and $NaClO_2$ treatment. After the delignification process, most lignin and hemicellulose were removed with a 27.4wt% yield of cellulose fibers, and the mean diameter of cellulose fibers

decreased from 137±46 to 12±5μm. The higher NaOH concentration and longer treatment time led to the decrease of lignocellulose yield. The crystallinity of cellulose fibers first decreased and then increased during the transformation from cellulose I to II, and the crystallinity decreased through further $NaClO_2$ treatment. The raw bagasse samples showed three-step pyrolysis processes, while NaOH and NaOH/$NaClO_2$ treated fibers had one-step pyrolysis process. Compared with the NaOH treated fibers, the NaOH/$NaClO_2$ treated fibers had a lower thermal stability. The properties of cellulose fibers from energycane bagasse demonstrated in this study are anticipated to provide some fundamental information for improving their potential applications in the field of clothes, cosmetic, pharmaceuticals, biomedicine and smart materials.

2.5 REFERENCES

Aita, G.M., Kim, M., 2011. Pretreatment Technologies for the Conversion of Lignocellulosic Materials to Bioethanol. In: Eggleston, G. (Ed.), Sustainability of the Sugar and Sugar-Ethanol Industries. ACS Press, St. Gabriel, LA, pp. 117-145.

Ben Sghaier, A.E.O., Chaabouni, Y., Msahli, S., Sakli, F., 2012. Morphological and crystalline characterization of NaOH and NaOCl treated *Agave americana* L. fiber. Industrial Crops and Products 36, 257-266.

Bussemaker, M.J., Zhang, D.K., 2013. Effect of Ultrasound on Lignocellulosic Biomass as a Pretreatment for Biorefinery and Biofuel Applications. Industrial and Engineering Chemistry Research 52, 3563-3580.

Correa, A.C., Teixeira, E.D., Pessan, L.A., Mattoso, L.H.C., 2010. Cellulose nanofibers from curaua fibers. Cellulose 17, 1183-1192.

Corredor, D.Y., Salazar, J.M., Hohn, K.L., Bean, S., Bean, B., Wang, D., 2009. Evaluation and characterization of forage sorghum as feedstock for fermentable sugar production. Applied Biochemistry and Biotechnology 158, 164-179.

Gatenholm, P., Klemm, D., 2010. Bacterial Nanocellulose as a Renewable Material for Biomedical Applications. Mrs Bulletin 35, 208-213.

Goshadrou, A., Karimi, K., Taherzadeh, M.J., 2011. Bioethanol production from sweet sorghum bagasse by Mucor hiemalis. Industrial Crops and Products 34, 1219-1225.

Gwon, J.G., Lee, S.Y., Doh, G.H., Kim, J.H., 2010. Characterization of Chemically Modified Wood Fibers Using FTIR Spectroscopy for Biocomposites. Journal of Applied Polymer Science 116, 3212-3219.

Han, J.Q., Zhou, C.J., Wu, Y.Q., Liu, F.Y., Wu, Q.L., 2013. Self-Assembling Behavior of Cellulose Nanoparticles during Freeze-Drying: Effect of Suspension Concentration, Particle Size, Crystal Structure, and Surface Charge. Biomacromolecules 14, 1529-1540.

Hoi, L.W.S., Martincigh, B.S., 2013. Sugar cane plant fibres: Separation and characterisation. Industrial Crops and Products 47, 1-12.

Hubbell, C.A., Ragauskas, A.J., 2010. Effect of acid-chlorite delignification on cellulose degree of polymerization. Bioresource Technology 101, 7410-7415.

Jungnikl, K., Paris, O., Fratzl, P., Burgert, I., 2008. The implication of chemical extraction treatments on the cell wall nanostructure of softwood. Cellulose 15, 407-418.

Khan, M.A., Ashraf, S.M., Malhotra, V.P., 2004. Development and characterization of a wood adhesive using bagasse lignin. International Journal of Adhesion and Adhesives 24, 485-493.

Kim, M., Day, D.F., 2011. Composition of sugar cane, energy cane, and sweet sorghum suitable for ethanol production at Louisiana sugar mills. Journal of Industrial Microbiology & Biotechnology 38, 803-807.

Kljun, A., Benians, T.A.S., Goubet, F., Meulewaeter, F., Knox, J.P., Blackburn, R.S., 2011. Comparative Analysis of Crystallinity Changes in Cellulose I Polymers Using ATR-FTIR, X-ray Diffraction, and Carbohydrate-Binding Module Probes. Biomacromolecules 12, 4121-4126.

Li, J.B., Henriksson, G., Gellerstedt, G., 2007. Lignin depolymerization/repolymerization and its critical role for delignification of aspen wood by steam explosion. Bioresource Technology 98, 3061-3068.

Liu, Y.P., Hu, H., 2008. X-ray diffraction study of bamboo fibers treated with NaOH. Fibers and Polymers 9, 735-739.

Mandal, A., Chakrabarty, D., 2011. Isolation of nanocellulose from waste sugarcane bagasse (SCB) and its characterization. Carbohydrate Polymers 86, 1291-1299.

Martin, C., Alriksson, B., Sjode, A., Nilvebrant, N.O., Jonsson, L.J., 2007. Dilute sulfuric acid pretreatment of agricultural and agro-industrial residues for ethanol production. Applied Biochemistry and Biotechnology 137, 339-352.

Moran, J.I., Alvarez, V.A., Cyras, V.P., Vazquez, A., 2008. Extraction of cellulose and preparation of nanocellulose from sisal fibers. Cellulose 15, 149-159.

Mwaikambo, L.Y., Ansell, M.P., 2002. Chemical modification of hemp, sisal, jute, and kapok fibers by alkalization. Journal of Applied Polymer Science 84, 2222-2234.

O'Connor, R.T., DuPré, E.F., Mitcham, D., 1958. Applications of Infrared Absorption Spectroscopy to Investigations of Cotton and Modified Cottons. Textile Research Journal 28, 382-392.

Oh, S.Y., Yoo, D.I., Shin, Y., Kim, H.C., Kim, H.Y., Chung, Y.S., Park, W.H., Youk, J.H., 2005. Crystalline structure analysis of cellulose treated with sodium hydroxide and carbon dioxide by means of X-ray diffraction and FTIR spectroscopy. Carbohydrate Research 340, 2376-2391.

Park, J.M., Kim, S.J., Jang, J.H., Wang, Z.J., Kim, P.G., Yoon, D.J., Kim, J., Hansen, G., DeVries, K.L., 2008. Actuation of electrochemical, electro-magnetic, and electro-active actuators for carbon nanofiber and Ni nanowire reinforced polymer composites. Composites Part B-Engineering 39, 1161-1169.

Rezende, C.A., de Lima, M.A., Maziero, P., deAzevedo, E.R., Garcia, W., Polikarpov, I., 2011. Chemical and morphological characterization of sugarcane bagasse submitted to a delignification process for enhanced enzymatic digestibility. Biotechnology for Biofuels 4, 1-18.

Singh, S., Bharadwaja, S.T.P., Yadav, P.K., Moholkar, V.S., Goyal, A., 2014. Mechanistic Investigation in Ultrasound-Assisted (Alkaline) Delignification of Parthenium hysterophorus Biomass. Industrial and Engineering Chemistry Research 53, 14241-14252.

Siroky, J., Blackburn, R.S., Bechtold, T., Taylor, J., White, P., 2010. Attenuated total reflectance Fourier-transform Infrared spectroscopy analysis of crystallinity changes in lyocell following continuous treatment with sodium hydroxide. Cellulose 17, 103-115.

Sun, J.X., Sun, X.F., Zhao, H., Sun, R.C., 2004. Isolation and characterization of cellulose from sugarcane bagasse. Polymer Degradation and Stability 84, 331-339.

Sun, R.C., Tomkinson, J., Zhu, W., Wang, S.Q., 2000. Delignification of maize stems by peroxymonosulfuric acid, peroxyformic acid, peracetic acid, and hydrogen peroxide. 1. Physicochemical and structural characterization of the solubilized lignins. Journal of Agricultural and Food Chemistry 48, 1253-1262.

Talebnia, F., Karakashev, D., Angelidaki, I., 2010. Production of bioethanol from wheat straw: An overview on pretreatment, hydrolysis and fermentation. Bioresource Technology 101, 4744-4753.

Wang, Z.G., Yokoyama, T., Chang, H.M., Matsumoto, Y., 2009. Dissolution of Beech and Spruce Milled Woods in LiCl/DMSO. Journal of Agricultural and Food Chemistry 57, 6167-6170.

Yang, H.P., Yan, R., Chen, H.P., Lee, D.H., Zheng, C.G., 2007. Characteristics of hemicellulose, cellulose and lignin pyrolysis. Fuel 86, 1781-1788.

Yue, Y.Y., Han, J.Q., Han,G.P., Zhang, Q.G., French, A.D., Wu, Q.L., 2015. Characterization of cellulose I/II hybrid fibers isolated from energycane bagasse during the delignification process: morphology, crystallinity and percentage estimation. Carbohydrate Polymer 133, 438-447.

Yue, Y.Y., Zhou, C.J., French, A.D., Guan, X., Han, G.P., Wang, Q.W., Wu, Q.L., 2012. Comparative properties of cellulose nano-crystals from native and mercerized cotton fibers. Cellulose 19, 1173-1187.

CHAPTER 3 CHARACTERIZATION OF CELLULOSE I/II HYBRID FIBERS ISOLATED FROM ENERGYCANE BAGASSE DURING THE DELIGNIFICATION PROCESS: MORPHOLOGY, CRYSTALLINITY AND PERCENTAGE ESTIMATION[2]

3.1 INTRODUCTION

Owing to the attractive properties of low density, high strength, high tensile modulus, abundance, eco-friendliness, and sustainability (Lu et al., 2008; Thakur et al., 2013a; Thakur et al., 2013b), cellulose has broad applications, such as pharmaceuticals, chemical feedstocks, papermaking and liquid fuel production (Kumar et al., 2002; Sun et al., 2004c). Cellulose offers light weight, strong reinforcing effects, and improved thermal stability in diverse materials that could be used in automobiles and buildings (Thakur and Thakur, 2014; Thakur et al., 2014).

Energycane, a hybrid of commercial and wild sugarcanes, is cold tolerant and can be grown on fallow land. Compared to sugar cane, it requires less fertilizer and water and it adapts to colder weather (Qiu and Aita, 2013). More importantly, it possesses a high fiber content which provides a more sustainable source of cellulose (Kim and Day, 2011). However, the presence of a hemicellulose and lignin complex reduces accessibility to cellulose microfibrils and hinders cellulose isolation (Hubbell and Ragauskas, 2010). Therefore, delignification is a critical process towards the successful separation of cellulose from the other components of energycane bagasse.

Sodium hydroxide treatment has been used to partially separate the microfibrils from the cell wall, remove natural impurities, and obtain fibers with low lignin and hemicellulose content (Moubarik et al., 2013). It is generally thought that alkali can penetrate the inter-fibril region and cleave α-ether bonds between lignin and hemicellulose (Sun et al., 2000b; Mwaikambo and Ansell, 2002). Besides alkali treatment, acid chlorite (acetic acid and sodium chlorite) treatments

[2] Reprint in part with permission from Carbohydrate Polymer
Yue, Y.Y., Han, J.Q., Han,G.P., Zhang, Q.G., French, A.D., Wu, Q.L., 2015. Characterization of cellulose I/II hybrid fibers isolated from energycane bagasse during the delignification process: morphology, crystallinity and percentage estimation. Carbohydrate Polymer 133, 438-447.

that employ oxidizing agent chorine dioxide (ClO_2^-) for bleaching and disinfection are effective for delignification (Hubbell and Ragauskas, 2010; Agarwal et al., 2013; Moubarik et al., 2013).

The structural transformation from parallel arrangement of cellulose I (native cellulose) to antiparallel-chains structure of cellulose II occurs by NaOH treatment. During this process, the entire fibers are converted into a swollen state and hydroxyl groups on cellulose surface are able to interact with one another to form different type of intra and intermolecular hydrogen bonds. Because of the different supermolecular structure of cellulose I and cellulose II, mechanical, chemical and thermal properties of these two kinds of fibers, such as dimensional stability, fibrillation tendency, tensile strength, dyeability, luster and fabric smoothness, change significantly (Siroky et al., 2010). Cellulose I fibers are widely used in many industries such as clothing, cosmetics and pharmaceuticals. On the other hand, cellulose II fibers have some preferable properties over cellulose I fibers in clothing, smart materials (such as electro-activepaper (EAPap), sensors, actuators), biomedicine (such as tablet excipients), and reinforcing materials (such as filler and binder) (Kumar et al., 2002; Ma et al., 2011).

However, the transformation from cellulose I to cellulose II is not spontaneous. The presence of lignin can somehow prevent or retard chemical penetration and swelling of cellulose, and intermingling of the cellulose molecules from adjacent microfibrils, resulting in cellulose I and II mixture. The presence of a cellulose I and II hybrid affects morphology, thermal stability and mechanical properties of cellulose fibers. Therefore, evaluating the percentage of cellulose I and II in cellulose hybrid fibers plays a crucial role to further utilize cellulose materials. A few researchers mentioned the existence of cellulose I/II mixtures in their studies (Nelson and O'Connor, 1964; Correa et al., 2010). However, little is known about the percentages of cellulose

I and II in cellulose I/II hybrid fibers, and the chemical structural and morphologial properties of these hybrid fibers.

Hence, fundamental research needs to be conducted in order to characterize in detail the cellulose I/II hybrid fibers. In the present work, cellulose I, cellulose II and cellulose I/II hybrid fibers were isolated from energycane bagasse using a combined NaOH/$NaClO_2$ treatment. The objective of this study was to characterize the morphology, crystallinity, percentage and functional groups of the cellulose I/II hybrid fibers obtained during the delignification process. Techniques including XRD, ^{13}C NMR and FTIR were employed for qualitatively investigating crystallinity, crystal form and for estimating the percentage of cellulose I and II in the hybrid fibers.

3.2 MATERIALS AND METHODS

3.2.1 Materials

Energycane bagasse (HO 02-113) from the Audubon Sugar Institute at Louisiana State University Agricultural Center, St. Gabriel, LA, was used as raw material. The bagasse was dried in an oven at 40 ℃ for 48h before use. The dried material was then ground by a CIT-FW-200 grinder (Col-Int Tech, Irmo, SC, USA) until a maximum particle size of 10 mesh (i.e. 2.0 mm) was obtained. Sodium chlorite (80%, RT) and acetic acid (glacial, 99.85%) were purchased from Sigma-Aldrich Inc. (St. Louis, MO, USA). Sodium hydroxide (98.9%, ACS grade) obtained from Fisher Scientific Inc. (Fair Lawn, NJ, USA) was dissolved in distilled water to prepare 10wt% and 20wt% aqueous solutions. All reagents and solvents used were of analytical grade. Distilled water was used in preparation of all solutions.

3.2.2 Isolation of Cellulose

Twenty grams of dried bagasse were first pretreated in hot water at 70 ℃ for 2h and the obtained material was washed with distilled water to remove part of extraneous components, such as fermentable sugars, ash (silicon, calcium, magnesium and sodium) and extractives (phytosterols, fats and fatty acids). Subsequently, it was treated with 10wt% and/or 20wt% NaOH aqueous solution at 98 ℃ for 90min and/or 10h. All the experiments were performed in an oil bath with continuous agitation. After being cooled to 25 ℃, the resultant materials were filtered and thoroughly washed with distilled water until a neutral pH was reached.

Because NaOH treatment might not achieve complete isolation of pure cellulose, acidified $NaClO_2$ was further used to remove the remaining lignin and hemicellulose. The NaOH pretreated cellulose fibers (~1 g) reacted with a $NaClO_2$/glacial CH_3COOH mixture (0.75g $NaClO_2$ to 1g obtained lignocellulose fibers; and 1ml glacial acetic acid to 50ml water) at 75 ℃ for 2h. The reaction environment (pH < 4.0) was maintained by adding $NaClO_2$ and glacial CH_3COOH every half hour. After being cooled to 20 ℃, the bleached cellulose fibers were washed with distilled water to a neutral pH. The obtained cellulose fibers were pure white. If a yellow-color persisted, the $NaClO_2$/glacial CH_3COOH mixture was added for further delignification. The final cellulose fibers were dried at 40 ℃ for 48h in a vacuum oven. The scheme for cellulose isolation procedure is shown in Figure 3.1.

The NaOH treated samples were designated as Bxy with x= 10, 20 (NaOH concentration/wt%) and y=1.5, 10 (reaction time/hour). For example, the sample without NaOH treatment was designated as B0 and the sample treated with 10wt% NaOH solution for 1.5h was designated as B101.5. Similarly, the samples treated by NaOH/$NaClO_2$ were designated as Bxys. Thus, B101.5 became B101.5s after $NaClO_2$ treatment.

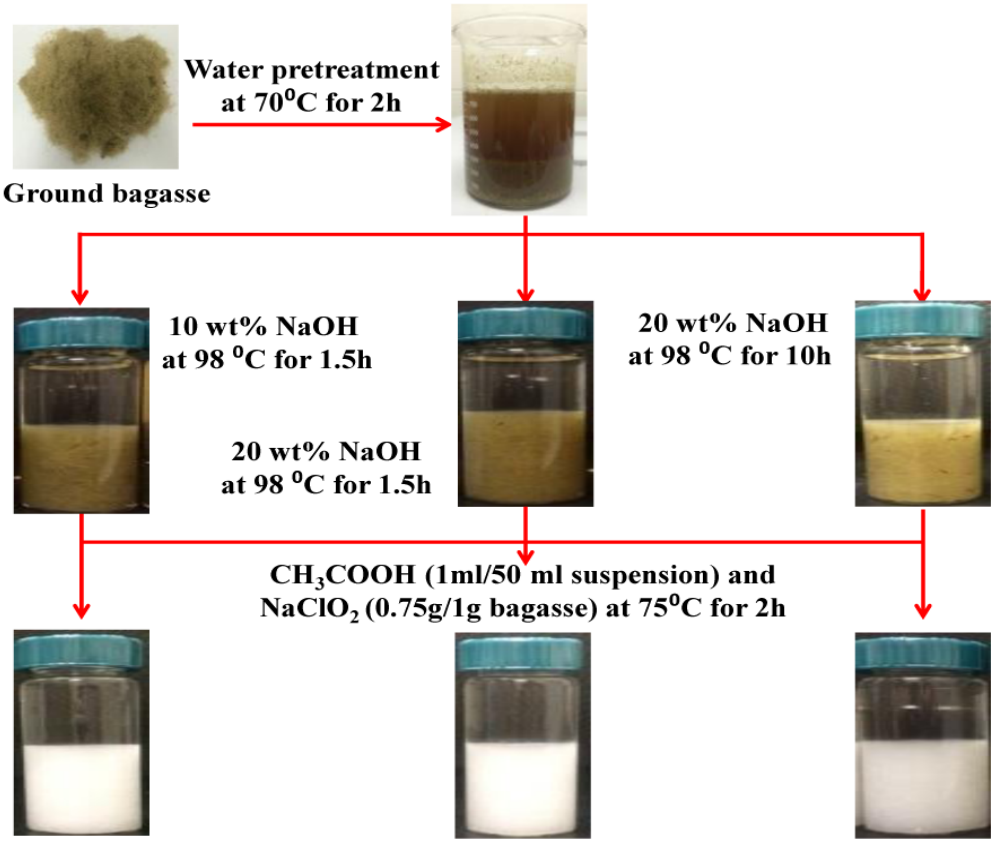

Figure 3.1 Scheme for isolation of cellulose from energycane bagasse

3.2.3 Characterizations

3.2.3.1 Environmental Scanning Electron Microscope (ESEM)

ESEM images were acquired via Quanta 200 F microscope from FEI Company (Hillsboro, OR, USA) at 12.5kV. Prior to the ESEM observation, oven dried lignocellulose fibers were mounted on aluminum stubs with conductive carbon tape and subjected to gold-sputtering by an Electron Microscopy Services 350 sputter coater for 2minutes. For each sample, around 20 fibers were randomly selected and measured from ESEM images. Fiber width defined as the dimension perpendicular to its long axis was measured using Image J software (http://imagej.nih.gov/ij/, 1997-2011).

3.2.3.2 Wide-Angle X-ray Diffraction (WXRD)

Crystalline structures of the lignocellulose fibers were analyzed by a Bruker/ Siemens D5000 automated WXRD (D/max-1200, Rigaku Denki Inc., Tokyo, Japan). The data were generated by a diffractometer with Cu Kα radiation (λ = 1.54Å) at 40 kV and 30 mA over the angular range 2θ = 5 −40° and a step time of 2.0s. A focusing (reflection) powder diffraction method was applied. To increase the density of the samples, pressed pellets presented to the X-ray beam.

The Crystallinity Index (CI) is determined using Equation [3.1]:

$$CI(\%) = (1 - \frac{h_{am}}{h_{\mathrm{Cr}}}) \times 100 \qquad [3.1]$$

where h_{Cr} is the height of highest peak, and h_{am} is the intensity of diffraction attributed to amorphous cellulose. The intensity height for amorphous material is taken near 18 °for cellulose I and around 16 ° for cellulose II (Azubuike et al., 2012). The CI values are calculated from the original data without subtracting background (Segal et al., 1959).

The crystal size of cellulose I and II samples, t (nm), is determined perpendicular to the (200) planes by the Scherrer Equation:

$$t = \frac{K\lambda}{\beta Cos\theta} \qquad [3.2]$$

where K=1.0 is the shape correction factor; λ is the radiation wavelength; β is the corrected angular width at half maximum intensity of diffraction peak in radians; θ is half of the 2θ angle where the highest diffraction peak occurred.

The spacing between the (200) planes, d (nm), is calculated using the Bragg Equation:

$$n\lambda = 2d\sin\theta \qquad [3.3]$$

where n is an integer; λ is the wavelength of incident radiation; and θ is the angle between the incident ray and the scattering plane.

3.2.3.3 Solid-State Cross Polarization/Magic Angle Spinning Nuclear Magnetic Resonance (Solid-state CP/MAS ^{13}C NMR)

Solid-state CP/MAS ^{13}C NMR measurements were recorded at 100MHz on a Bruker AV-400 spectrometer with a wide bore magnet and a 4mm CP/MAS probe (Varian Inc, Lake Forest, CA, USA). ^{13}C CP/MAS data were collected at 20℃ with 50kHz spectra width, 2msec cross-polarization contact time and 0.035s acquisition time. The number of scans was 8196 and rotational velocity of sample was 20Hz. The data were processed using the Bruker TopSpin Software.

3.2.3.4 Fourier Transform Infrared Spectrometry (FTIR)

FTIR spectra of dried samples were measured on a Bruker FTIR analyzer (Tensor-27, Bruker Optics Inc., Billerica, MA, USA) with an attenuated total reflectance (ATR) mode. Each sample was pressed into the chamber of the FTIR equipment and scanned in the range from 4000 to 600cm^{-1} with a resolution of 4 cm^{-1}. 64 repetitious scans were averaged per sample and the background spectra were collected before each sampling. Three replicated measurements were recorded for each condition.

3.3 RESULTS AND DISCUSSION

3.3.1 Fiber Morphology by ESEM

The morphological features of original ground bagasse (Figure 3.2a), the samples after NaOH treatment (Figure 3.2b-d), and the fibers after NaOH/$NaClO_2$ treatments (Figure 3.2e-g) were observed by ESEM. Because the native bagasse fibers were coated and interlinked together with lignin and extractives (Hubbell and Ragauskas, 2010; Santi et al., 2013), the B0 sample

possessed rigid and highly ordered parallel structure with an average width of 137±46μm, and their surfaces were fairly smooth (Figure 3.2a).

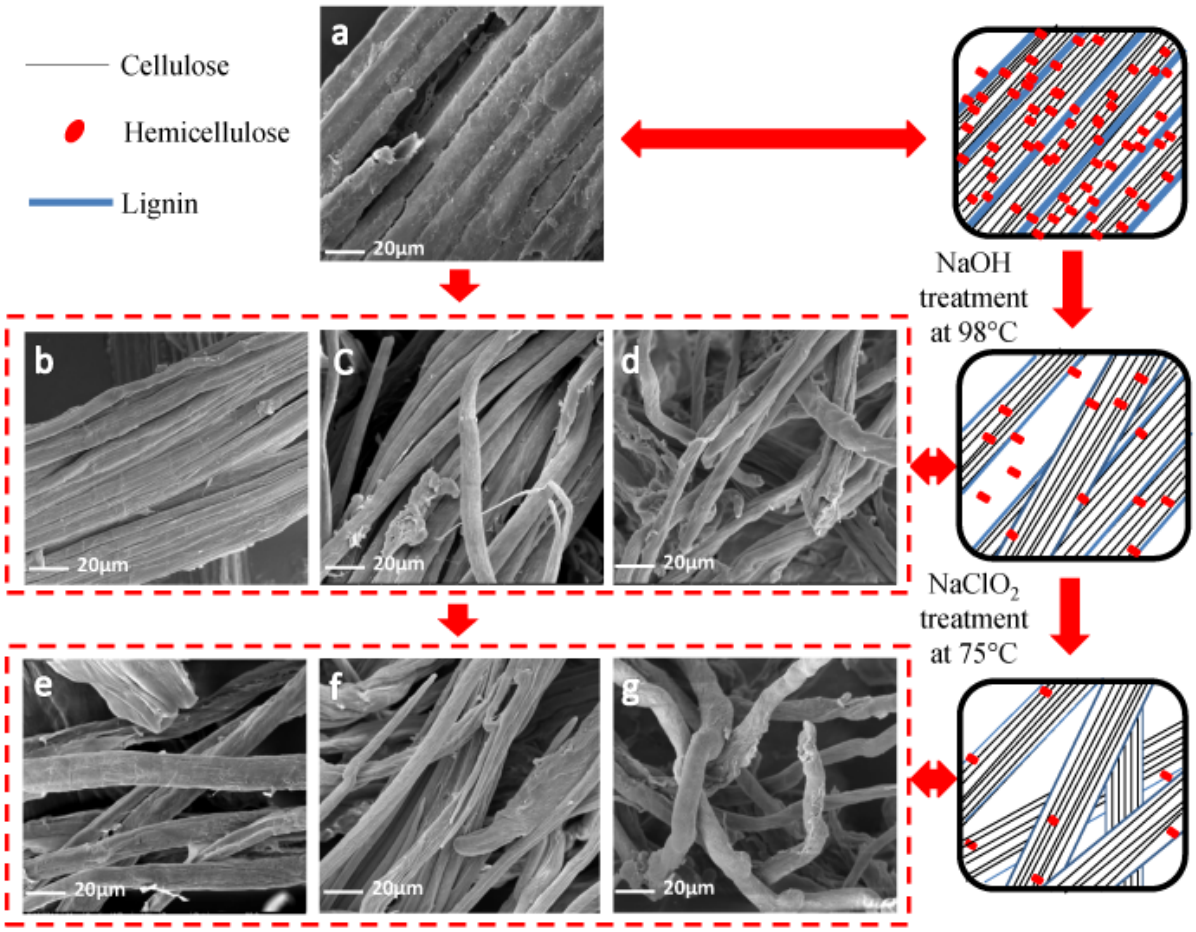

Figure 3.2 ESEM images of raw bagasse fibers B0 (a), NaOH treated fibers: B101.5 (b), B201.5 (c), B2010 (d), and NaOH/$NaClO_2$ treated fibers: B101.5s (e), B201.5s (f), B 2010s (g) with a magnification of 1000.

After being treated with 10wt% NaOH for 1.5h, B101.5 consisted of parallel fiber bundles with a smaller fiber width of 93±38μm, suggesting the decrease of lignin content (Figure 3.2b). At the 20wt% NaOH concentration level, the structure of lignocellulose started to unpack and the cellulose fibers detached from each other. The average fiber width for B201.5 was 47±40 μm and the reduced fiber diameter indicated some fiber bundles were being defibrillated (Figure 3.2c). After the fibers were treated at a higher NaOH concentration for a longer treatment time

(i.e., 20wt% NaOH for 10h) (Figure 3.2d), significant defibrillation of fibrils with the corresponding width decreased to 19±8μm was shown. The mean diameter of the fibers after NaOH treatment was one seventh as much as that of B0, indicating the considerable reduction of interfibrillar lignin and hemicellulose (Rezende et al., 2011). The schematic illustration for the whole delignification process is presented to the right of Figure 3.2.

After the NaOH/$NaClO_2$ treatments, most of the hemicellulose and lignin components were removed and the cellulose fibers were separated into individual microsized fiber. The corresponding fiber width for B101.5s, B201.5s and B2010s were 15±7, 14±8 and 12±5μm (Figure 3.2e-g). The elimination of non-cellulosic components increased the surface area of cellulose, making cellulose more accessible to further treatment (Hubbell and Ragauskas, 2010; Santi et al., 2013).

In addition, the fibers treated with mild alkali for 1.5h (B101.5 and B101.5s) (Figure 3.2b and e) presented a flat shape with a smooth surface. As NaOH concentration and treatment time increased, B2010 and B2010s (Figure 3.2d and g) were converted into a more swollen state with a rougher surface compared to the fibers treated at a lower NaOH concentration for a shorter treatment time.

B2010 and B2010s had smaller lignin content and better defibrillation than the other samples at the corresponding treatment step. However, the super-molecular structure for B2010 and B2010s significantly changed during NaOH/$NaClO_2$ treatments, which was discussed in the following WXRD section.

3.3.2 Percentage Calculation and Crystallinity Index of Cellulose Hybrid fibers by WXRD

The diffraction patterns of raw fibers (B0), NaOH treated fibers (B101.5, B201.5, B2010), and NaOH/$NaClO_2$ treated fibers (B101.5s, B201.5s, B2010s) are shown in Figure 3.3a and b.

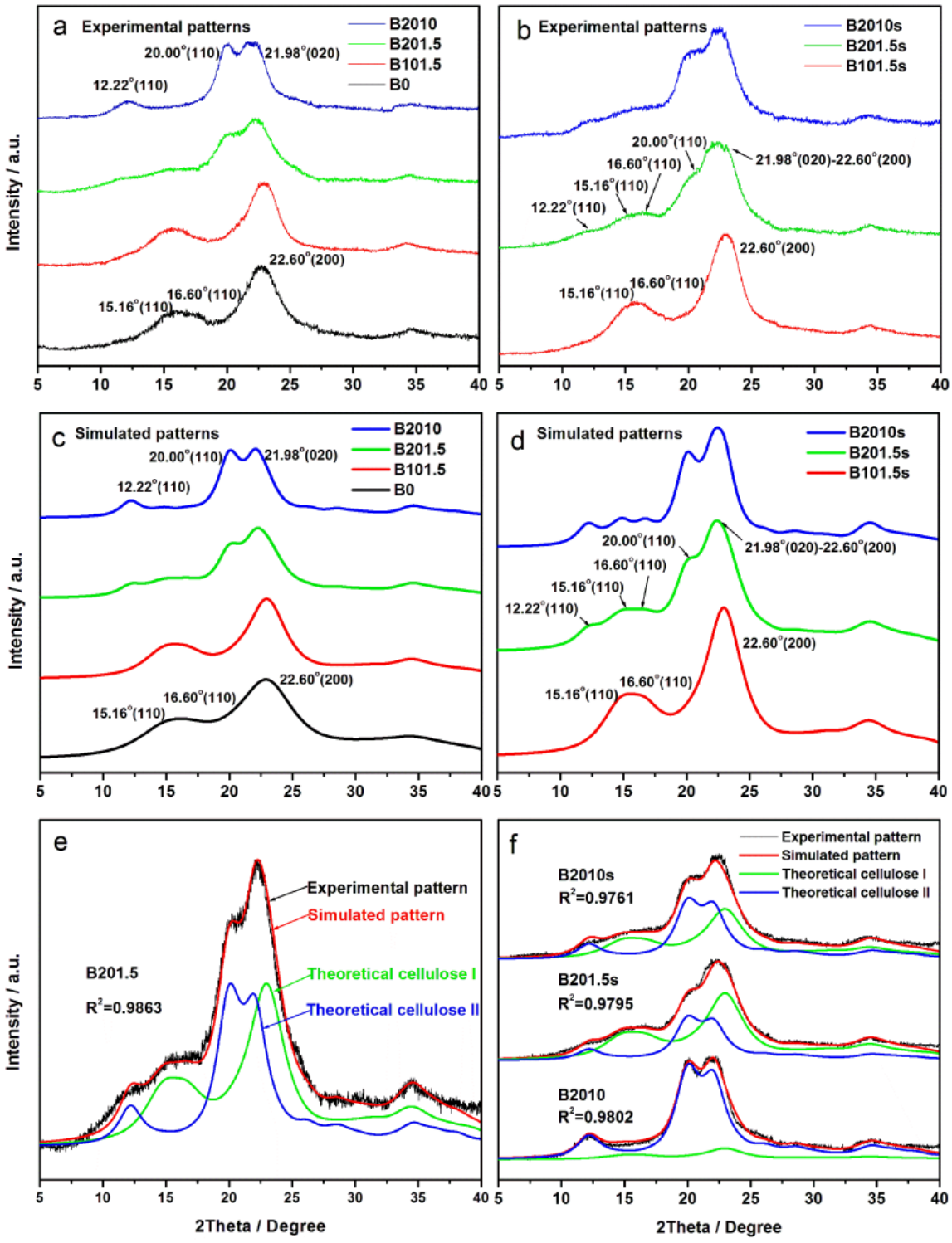

Figure 3.3 X-ray diffraction patterns of lignocellulose fibers under NaOH treatments (a) and NaOH/$NaClO_2$ treatments (b), the corresponding simulated patterns for NaOH treatments (c) and NaOH/$NaClO_2$ treatments (d), and the fitting analysis of cellulose hybrid: B201.5 (e) and B2010, B201.5s and B2010s (f).

B0, B101.5 and B101.5s present a single peak at 2θ=22.60 ° (200) and two overlapped weaker diffraction peaks at 2θ=15.16 ° ($1\bar{1}0$) and 16.60 ° (110), showing a typical cellulose I structure (Kljun et al., 2011; Han et al., 2013d). It was thus concluded that the conversion from cellulose I to cellulose II could not be achieved when NaOH concentration ≤10wt%, which was consistent with our previous study (Yue et al., 2012b).

For samples with a NaOH concentration of 20wt% (B201.5 and B201.5s), the two diffraction peaks at 2θ=15.16 °and 16.60 °decreased and a small peak at 2θ=12.22 °($1\bar{1}0$) formed, indicating the presence of a mixture of cellulose I and II. A possible reason for the existence of cellulose hybrid is that at a lower NaOH concentration level, lignocellulose cannot be completely transferred into the swollen state, and only a portion of parallel cellulose microfibrils can rearrange to cellulose II, leading to the coexistence of cellulose I and II fibers.

Although the phenomenon of cellulose I/ II hybrid was mentioned (Isogai and Atalla, 1998; Qi et al., 2009), little is known about evaluating the percentage of cellulose I and cellulose II in the hybrid. In the present study, the percentages of cellulose I and II were estimated by Mercury software. The theoretical intensities were obtained by inputting the peak widths at half maximum height (PWHM) within the range of 2.0-3.3. All of the intensities of hybrid fibers are obtained using formula [3.4],

$$Intensity_{Hybrid} = Theoretical\ Cellulose\ I\ Data\ \times P_{Cellulose\ I} + Theoretical\ Cellulose\ II\ data \times (1 - P_{Cellulose\ I}) \quad [3.4]$$

where $P_{Cellulose\ I}$ is the percentage of cellulose I which is evaluated by fitting the experimental intensities with the theoretical intensities. The pseudo-Voigt function in Origin software was introduced for correcting the baselines of experimental pattern (Langford and Wilson, 1978), and the Pearson correlations were further employed for evaluating the accuracy of simulation. If the

correlation between experimental and theoretical intensities was poor, other PWHM or $P_{Cellulose\ I}$ was used in order to achieve better estimation. The patterns simulated by Mercury software are shown in Figure 3.3c and d, and the baseline-corrected experimental curve and the simulated pattern for cellulose hybrids are shown in Figure 3.3e and f.

Based on the above method, it was found that B201.5 was composed of 52% cellulose I and 48% cellulose II; and B201.5s contained 61% cellulose I and 39% cellulose II. These results suggested that the increasing of parallel-chain structure of cellulose I and the decreasing of anti-parallel-chain structure of cellulose II occurred during the process of $NaClO_2$ treatment. One possible reason was that part of cellulose I and cellulose II chains were de-crystallization and subsequently rearranged under the action of $NaClO_2$ treatment.

For preparation of pure cellulose II, increased treatment time was considered because complete transition from cellulose I to II was achieved with 20wt% NaOH treatment. In addition, if NaOH concentration ≥25wt%, the percentage of cellulose II rapidly dropped due to the molecular degradation of cellulose chains (Borysiak and Garbarczyk, 2003).

For B2010, the peaks at 2θ=15.16 °and 2θ=16.60 ° disappeared and the intensity of the peak at 2θ=12.22 ° $(1\bar{1}0)$ increased (Figure 3.3a). The main diffraction peaks located at 2θ=12.22 $(1\bar{1}0)$, 20.00 ° (110) and 21.98 ° (020) resulted from a cellulose II crystal structure (Han et al., 2013c; Han et al., 2013d). However, according to the fitting analysis, B2010 was still not pure cellulose II, it contained 95% cellulose II and 5% cellulose I. After a further $NaClO_2$ treatment, B2010s was composed of 44% cellulose I and 56% cellulose II. The possible reason is that the strong oxidizing properties of $NaClO_2$ could partly destroy intermolecular or/ and intramolecular hydrogen bond network at the time of removing lignin, thereby allowing fibers converting into a swollen state, leading to the second time rearrangement of cellulose chains.

The percentage of cellulose I in cellulose I/II hybrid, crystallinity index (CI), peak widths at half of the maximum peak intensity (PWHM), d-spacing of the planes (nm) and crystal size perpendicular to the planes (nm) are shown in Table 3.1.

Table 3.1 The percentage of cellulose I, PWHM, d-spacing, crystal size and crystallinity values of raw and treated fibers by different analytical techniques and calculation approaches

Sample No.	Percentage of cellulose I	PWHM[a]	d-spacing (nm)[b]	Crystal size (nm)[c]	CI (XRD, %)[d]	CI (^{13}C NMR, %)[e]	TCI (FTIR)[f]
B0	100	3.3	0.386	2.73	32.4	23.7	1.62
B101.5	100	3.3	0.386	2.73	58.2	35.7	1.73
B201.5	52	-	-	-	-	-	1.57
B2010	5	2.2	0.446	4.07	68.8	39.3	1.66
B101.5s	100	3.3	0.386	2.73	56.7	34.3	1.69
B201.5s	61	-	-	-	-	-	1.45
B2010s	44	-	-	--	-	-	1.50

a Peak widths at half of the maximum peak intensity
b d-spacing of the planes, calculated using the Bragg's equation
c Calculated using the Scherrer equation, with K=1.0
d Crystallinity indexes based on the empirical Segal's equation
e Crystallinity indexes based on the method of NMR C4 region integration
f Total Crystallinity Index, calculated using the ratio of the absorption bands at 1371 cm^{-1} and 2900 cm^{-1}
Note: B0- raw fibers; B101.5, B201.5 and B2010- NaOH treated bagasse fibers (designated as Bxy with x= 10, 20 (NaOH concentration/wt%) and y=1.5, 10 (reaction time/hour)); B101.5s, B201.5s and B2010s- NaOH/$NaClO_2$ treated bagasse fibers (designated as Bxys)

B0 presented the lowest CI value (32.4) due to the presence of non-crystalline components (hemicellulose and lignin). After NaOH treatment, the CI of B101.5 and B2010 significantly increased, indicating the considerable reduction of inter/ intra-fibrillar lignin. In

addition, although the CI for cellulose I (B101.5) and II (B2010) cannot be directly compared, comparable crystallinities of I and II should lead to substantially higher CI values for cellulose II (Han et al., 2013c; Han et al., 2013d). A higher CI value along with the larger inter-planar spacing and crystal size for cellulose II fibers indicated agglomeration of the chain or arrangement of strong intermolecular hydrogen bond occurred through the conversion from cellulose I to cellulose II. Unfortunately, the Segal CI values, d-spacing and crystal size cannot be determined for cellulose I/II hybrid (B201.5). The problem was that the peaks in WXRD patterns were overlapped with the regions where the amorphous intensity was measured (French and Santiago Cintrón, 2013). After a further $NaClO_2$ treatment, the CI of B101.5s was lower than that of B101.5, indicating the NaOH/$NaClO_2$ treatments were strong enough to cause decrystallization. The same d-spacing value (0.386) along with crystal size value (2.73nm) for B0, B101.5 and B101.5s indicated the similar crystal structures.

3.3.3 Lignin Content, Composition and Cellulose Crystallinity Index by CP/MAS ^{13}C NMR

The CP/MAS ^{13}C NMR spectra of the raw and NaOH treated lignocelluloses are shown in Figure 3.4a. After NaOH treatment, the signals at 152.7, 148.1, 56.4 and 33.1-33.2 ppm relating to the aromatic groups of lignin significantly decreased and the bands at 172.8 and, 21.4 ppm corresponding to acetyl group of hemicelluloses disappeared, indicating that NaOH treatment was an effective method to remove lignin and hemicellulose components. Specifically, the syringyl (S) and guaiacyl (G) units contributed to signals at 152.7 ppm and 148.1ppm, respectively (Sun et al., 2000b). The noticeable signal observed at 56.4 ppm was assigned to methoxyl in lignin (Moubarik et al., 2013). The signal at 33.1 ppm was related to methyl and methylene groups and the signals at 172.8, 21.4 ppm corresponded to acetyl group of hemicelluloses (Sun et al., 2000b; Wen et al., 2013).

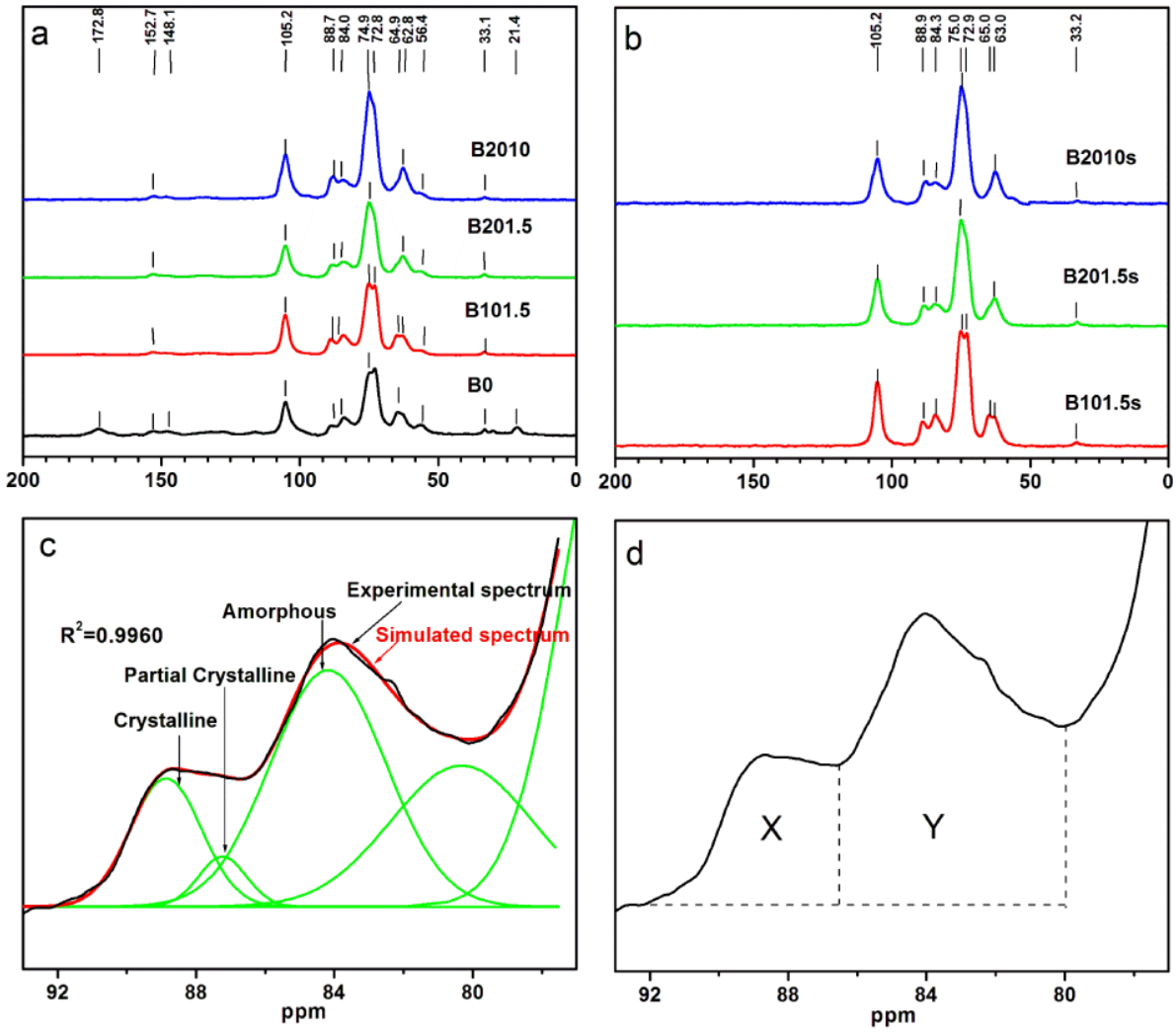

Figure 3.4 CP/MAS 13C NMR spectra of original and NaOH treated fibers (B0, B101.5, B201.5, B2010) (a), NaOH/$NaClO_2$ treated fibers (B101.5s, B201.5s B2010s) (b); the fitted curve of C4 region (c) and the crystallinity calculation of C4 region (d).

The signals from 60 to 70 ppm corresponded to C6 which provided the detailed information on orientation of the O6 group (Yoneda et al., 2008). It was reported that a signal at 65 ppm and an upfield shoulder near 63 ppm described the characteristic of cellulose I; whereas cellulose II possessed a broad peak at 63 ppm (Kamide et al., 1985; Zuckerstätter et al., 2013; Miura and Nakano, 2015). In Figure 3.4a, sample B101.5 consisted of two resonances (64.9 ppm, 62.8 ppm) and the dominated resonance was at 64.9 ppm; whereas B201.5 and B2010 had a

sharp peak at 62.8 ppm, indicating cellulose I structure of B101.5 and cellulose II characteristic of B201.5 and B2010.

The resonance at 105.2 ppm arose from C1 of cellulose. B0, B101.5 and B201.5 displayed a sharp peak and B2010 had a shoulder signal. According to the previous study, the C1 peak that responded to glycosidic linkage conformations along the molecular chain was a sharp singlet for cellulose I and a doublet for cellulose II (Kamide et al., 1985; Newman et al., 1996; Miura and Nakano, 2015). Therefore, B0, B101.5 and B201.5 had the feature of cellulose I and B2010 possessed the characteristics of cellulose II. In addition, according to the results of C6 and C1 analysis, B201.5 had the characteristics of both cellulose I and II, it was most likely that B201.5 consisted of a hybrid of cellulose I and II, which was identical with the XRD results.

The two peaks at 88.7-87.9 and 84.0 ppm for C4 of the various bagasse samples were attributed to well-ordered and noncrystaline cellulose, respectively (Sun et al., 2004a). The C4 resonance at 88.7 ppm increased and the signal at 84.0 ppm decreased during the structural transformation from B0 to B2010, suggesting that B2010 had a larger crystalline extent compared with the other samples. Furthermore, the C4 peak was observed at 88.7 ppm for cellulose I (B0 and B101.5), while it was at 87.9 ppm for cellulose I/II hybrid (B201.5 and B2010), suggesting the chemical shifts of C4 occurred during the transformation from cellulose I to II. The conformational non-equivalence was the most important reason for peak shifting (Vanderhart et al., 1981).

In contrast to well-separated resonances of C1, C4 and C6, the C2, C3 and C5 carbon peaks were not easily distinguishable since they were overlapped in the range 77-73 ppm (Sun et al., 2004a; Sun et al., 2004c). B0 and B101.5 presented two separated peaks around 74.9 ppm and 72.8 ppm, whereas only the sharp peak at 74.9 ppm was present for B201.5 and B2010,

indicating cellulose I and cellulose I/II hybrids had different resonance shapes in the patterns for C2, C3 and C5.

Figure 3.4b illustrates the CP/MAS ^{13}C NMR spectra of the bagasse fibers treated with NaOH/$NaClO_2$. Most lignin-related signals were unnoticeable and the typical cellulose spectra distributed in the region between 60.0 and 110.0 were shown, suggesting that relative pure cellulose were achieved. In addition, the effect of the NaOH and $NaClO_2$ treatments on crystal forms of cellulose I, II, and cellulose hybrids were studied. The signals occurring at 105.2 ppm (C1), 65.0 ppm and 63.0 ppm (C6) implied the cellulose I structure of B101.5s, whereas a broad peak around 63.0 ppm (C6) and two sharp resonances at 105.2 and 107.4 ppm indicated the characteristics of cellulose II (Kamide et al., 1985; Miura and Nakano, 2015). Although B201.5s and B2010s possessed the peaks at 63.0 and 105.2 ppm, the missing resonances at 65.0 and 107.4 ppm suggested that these two samples were cellulose I/II hybrids. It should be noted that cellulose II content in B2010s was larger than that in B201.5s, because a downfield shoulder at 107.4 ppm was appeared in B2010s.

In order to further analyze crystal forms, the C4 region was fitted using peak de-convolution method. This fitting process was performed using the peak analyzer tool within Origin software and the simulated spectra were generated with a Gaussian curve shape. As shown in Figure 3.4c, the complex experimental data can be simulated by several separable crystalline and amorphous curves (Sun et al., 2004c; Zuckerstätter et al., 2009). The peak attributed to crystalline-interior (ordered) sites was at 88.9 ppm. The peak corresponding to surface-crystalline site (partially-ordered) was at 87.3 ppm, and the peak assigned to noncrystalline (amorphous) sites was at 84.1 ppm. Generally, the peaks in the region of 86.5-93 ppm and 80-86.5 ppm were believed as crystalline and amorphous domain, respectively

(Newman et al., 1996; Mansfield and Meder, 2003; Zuckerstätter et al., 2009). Then NMR-CI values were calculated by dividing the region of X (crystalline domain) by the total area of X+Y (Figure 3.4d).

The NMR-CI values for raw and treated bagasse fibers are listed in Table 3.1. B0 had a lower NMR-CI than that of the NaOH treated samples, indicating that the treatment successively removed hemicellulose and lignin from the natural fibers. The near absence of aromatic signals at 105.2-160 ppm and 20-60 ppm for NaOH treated fibers further confirmed this conclusion. Also, the NMR-CI of B2010 was found to be 39.5%, which was larger than that of B101.5, indicating the crystallinity of cellulose II is higher than that of cellulose I (although the fibers B2010 were not pure cellulose II, it possessed cellulose II characteristic due to its tiny content of cellulose I). The crystallinity for B201.5 was not listed because the conformational and/or environmental transformation processes of cellulose hybrid were quite complicated and none of the measurement techniques have been used to estimate their crystallinity so far. After $NaClO_2$ treatment, B101.5s had a smaller crystallinity compared to B101.5, indicating that $NaOH/NaClO_2$ treatment did break the cellulose super-molecular structure.

CI values obtained from XRD and NMR measurements agreed qualitatively with each other, but NMR results provided much smaller CI values than the XRD data. Due to signal overlap, crystallite signals may also be detected in amorphous region, and then deviations of crystallinity were observed from the results of XRD and ^{13}C NMR analysis. The phenomenon was consistent with the previous result that the crystallinity measured by different characterization methods produced significantly different values (Zuckerstätter et al., 2009; Park et al., 2010).

3.3.4 Hydrogen Bonding and Crystallinity Index by FTIR

FTIR spectra within the range of 3600-2800cm^{-1}, 1800–1400cm^{-1}, 1400–1150cm^{-1} and 1150–800cm^{-1} are illustrated in Figure 3.5a-d, respectively. The absorbance band at 1632cm^{-1}was observed in all spectra, suggesting that absorbed water bending was not significantly affected by the delignification treatments (Figure 3.5b) (Han et al., 2013d).

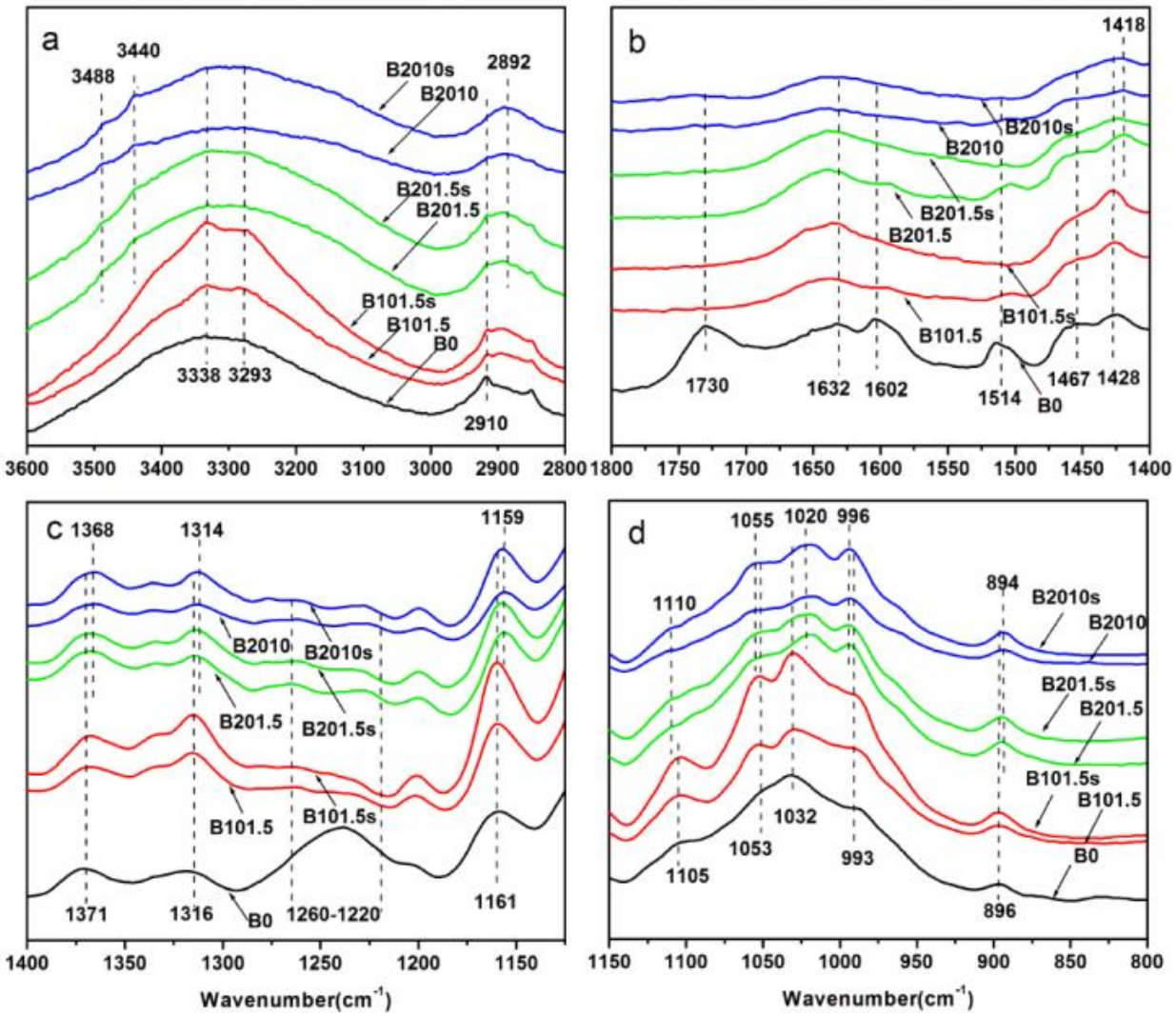

Figure 3.5 FTIR spectra of raw bagasse fibers (B0), NaOH treated fibers (B101.5, B201.5 and B2010) and NaOH/$NaClO_2$ treated fibers (B101.5s, B201.5s and B2010s) with the wavenumber ranges of 3600-2800 cm-1 (a), 1800-1400 cm-1 (b), 1400-1125 cm-1 (c) and 1150-800 cm-1 (d) respectively

The peak within 1740 and 1710cm^{-1} was corresponded to –COOH stretching of the ferulic and p-coumaric acids in lignin. The band at 1467cm^{-1} was arisen from methyl group deformations and lignin aromatic ring vibrations. In addition, the peaks at 1602cm^{-1} attributed to C=O stretching, 1514cm^{-1} related to aromatic skeleton vibrations, and 1250 cm^{-1} originating from C–O stretching in guaiacyl ring further indicated the presence of lignin and hemicellulose. For B0, the stronger intensity of these signals clearly showed the higher amount of non-cellulosic component (Sun et al., 2000b; Sun et al., 2004b; Sun et al., 2004c; Yang et al., 2007b; Mandal and Chakrabarty, 2011; Moubarik et al., 2013).

After the NaOH treatment, significant characteristics in crystal structure transition from cellulose I to II were seen within 3600-3000 cm^{-1} that corresponded to hydrogen bond O–H stretching (Figure 3.5a). When NaOH =10wt%, for B0, B101.5 and B101.5s, the bands related to the intramolecular hydroxyl groups of 3-OH…O-5 and intermolecular hydrogen bonds of 6-OH…O-3’ were observed at 3338 and 3293 cm-^{1} (Oh et al., 2005; Siroky et al., 2010). The maximum absorbance of C–H stretching influenced by the change of intra- and intermolecular bonds was observed at 2910 cm^{-1}. When NaOH = 20wt%, for B201.5, B201.5s, B2010 and B2010s, the absorbance band at 3338 cm^{-1} was absent. New absorbance bands at 3488 cm and 3440 cm^{-1} corresponding to the vibration of 2-OH…O-6 intramolecular hydrogen bond (Carrillo et al., 2004; Oh et al., 2005; Siroky et al., 2010), and the band at 3340–3230 cm^{-1} assigned to intermolecular hydrogen bond of 6-OH…O-2’ and intra-planar bonding of 6-OH…O-3’ and 2-OH…O-6 appeared, indicating that the development of new inter- and intramolecular hydrogen bonds (Oh et al., 2005; Siroky et al., 2010). The maximum absorbance band at 2910 cm^{-1} disappeared and the broader peak at 2892 cm^{-1} was observed.

Besides the differences influenced by hydrogen bond, the crystal structure transformation from the spectra of B201.5, B201.5s, B2010 and B2010s to B101.5 and B101.5s were also seen in the following regions. The strong band attributed to CH_2 bending with aromatic ring stretching vibrated at 1428 cm^{-1} and it turned into a weaker band and shifted to 1418 cm^{-1} after transition (Figure 3.5b) (Carrillo et al., 2004; Oh et al., 2005). The bands at 1316 cm^{-1} attributed to CH_2 wagging, 1371 cm^{-1} arisen from the C-H bending, 1161 cm^{-1} influenced by C-O-C asymmetric bridge stretching, 1105 cm^{-1} originating from anti-symmetric ring stretch, 1053 cm^{-1} corresponding to the C–O bond of aliphatic C–OH vibration, 1032cm^{-1} assigned as C-O-C pyranose ring skeletal vibration, 993cm^{-1} arisen from C–O valence vibration, 896 cm^{-1} assigned as C-O-C stretching at the β-(1→4)- glycosidic linkages between glucose units were shifted to 1314, 1368, 1159, 1110, 1055, 1020, 996 and 894cm^{-1}, respectively, indicating the changing of cellulose crystal structure (Carrillo et al., 2004; Sun et al., 2004a; Sun et al., 2004c; Oh et al., 2005; Kuo and Lee, 2009; Siroky et al., 2010; Chen et al., 2011). In addition, the decreased intensity of the bands near 1316, 1105, 1053 and 1032cm^{-1} and the increased intensity of the band around 993 cm^{-1} also suggested the formation of new crystal structure with cellulose II characteristic (Figure 3.5c and d). The main infrared absorbance bands corresponded to lignin polymer and crystalline cellulose are listed in Table 3.2.

As mentioned above, the crystallinity index for cellulose hybrid cannot be directly investigated by XRD and ^{13}C NMR. However, FTIR spectra can provide useful assessment of the crystallinity status for lignocellulose (Oh et al., 2005; Kljun et al., 2011; Moubarik et al., 2013). Nelson and O'Connor (1964) proposed a crystallinity index from the ratio of the bands at 1371 and 2900 cm^{-1} , called ''Total Crystallinity Index'' (TCI) . The TCI can be used to detect

even small changes in fiber crystallinity (Nelson and O'Connor, 1964; Siroky et al., 2010). In this study, crystallinity changes observed through infrared spectra were compared using the TCI.

Table 3.2 Comparison of wavenumbers of absorbance band before and after crystal transformation

No	Wavenumber (cm^{-1}) before crystal transformation	Wavenumber (cm^{-1}) after crystal transformation	Interpretation
1	-	3488	Vibration of intramolecular hydrogen-bond
2	-	3440	2-OH…O-6 intramolecular hydrogen bonds
3	3338-3293	-	3-OH…O-5 intramolecular and 6-OH…O-3’ intermolecular hydrogen bonds
4	-	3340–3230	6-OH…O-2’intermolecular and 6-OH…O-3’, 2-OH…O-6 intra-planar hydrogen bonds
5	2910	2892	C–H stretching
6	1740-1710	1740-1710	Carboxylic and/or ester groups
7	1632	1632	Absorbed water bending
8	1602	1602	Guaiacyl ring vibration and C=O stretching
9	1514	1514	Guaiacyl ring vibration

(Table 2.2 continued)

No	Wavenumber (cm^{-1}) before crystal transformation	Wavenumber (cm^{-1}) after crystal transformation	Interpretation
10	1467	1467	Methyl group deformations and aromatic skeletal vibrations
11	1428	1418	CH_2 bending with aromatic skeletal stretching
12	1371	1368	C-H bending
13	1316	1314	CH_2 wagging
14	1260-1220	1260-1220	C–O stretching in guaiacyl ring
15	1161	1159	C-O-C asymmetric bridge stretching
16	1105	1110	Anti-symmetric ring stretch
17	1053	1055	C–O bond of aliphatic C–OH vibration
18	1032	1020	C-O-C pyranose ring skeletal vibration
19	996	993	C–O valence vibration
20	896	894	C–O–C stretching at the β-(1→4)-glycosidic linkages

As shown in Table 3.1, the values derived from FTIR spectra and the results received from XRD and ^{13}C NMR patterns presented the same trend. The TCI value of B0 was smaller

than that of B201.5. The reason for lower crystallinity was because proportionally less cellulose existed in B0. After the NaOH treatment, the TCI value decreased from B101.5 to B201.5, and then it increased for B2010. This phenomenon can be explained as follows. Mercerization included three distinct processes: micro-fibril swelling, crystalline area disruption, and new crystalline lattice formation (Yue et al., 2012b). At lower NaOH concentrations (e.g. 10wt%), the number and size of NaOH hydrates were not large enough to destroy the cellulose lattice and cellulose crystal maintained its parallel-chain structure (B101.5). As NaOH concentration increased, the inter-fibrillar regions of cellulose were less rigid and a swollen state formed (Keusch and Haessler, 1999). Therefore, TCI value of B201.5 decreased in comparison with B0 and B101.5. When treatment time was increased to 10h, anti-parallel molecular structure of cellulose II was obtained by cellulose chain rearrangement, leading to an increased TCI value. However, TCI value of B2010 was lower than that of B101.5. The possible reason was that B2010 was not pure cellulose II and the mercerization was not completely finished. Because pyrolysis characteristics are highly correlated with the cellulose structure (Liu and Hu, 2008), the changed crystallinity and percentages of cellulose I/II hybrid fibers also contribute to define the thermal stability of the fibers. Yue et al. (2015) reported that B2010 had a remarkable thermal stability, followed by B101.5; whereas B201.5 showed relatively lower decomposition temperatures. This trend was basically following the changing in crystallinity of these fibers (B101.5> B2010> B201.5). It should be noted that although the transition from cellulose I to II was not fully finished, B2010 (5% cellulose I and 95% cellulose II) exhibited better thermal stability than B101.5 (cellulose I), indicating the thermal stability of cellulose II was superior to cellulose I.

In addition, compared with the origin and NaOH treated fibers, B101.5s, B201.5s and B2010s exhibited lower TCI values, indicating a less crystalline structure and lower thermal stability (Yue et al., 2015c). The phenomenon was caused by the strong destructive effect of $NaClO_2$. Although the TCI indices provided a practical way to qualitative study the cellulose hybrid, the values cannot be used in quantitative analysis because of the complexity of the cellulose transition.

3.4 CONCLUSIONS

In this work, cellulose I, cellulose II and cellulose I/II hybrid fibers were successfully produced from energycane bagasse using a combined NaOH pretreatment and $NaClO_2$ treatment. The definitive defibrillation effect with an average width of $12 \pm 5\mu m$ was observed for the fibers treated with 20wt% NaOH for 10h and $NaClO_2$ for 2h. The ribbon shaped cellulose I fibers were converted to a swollen state with a rougher surface by 20wt% NaOH treatment for 10h. The higher NaOH concentration and longer NaOH treatment time contributed to the transition from cellulose I to II. Based on the XRD results, the percentage of cellulose I decreased from 100% to 5%, and the CI values increased from 58.2% to 68.8% during the conversion from cellulose I to II. After a further $NaClO_2$ treatment, the CI values for the corresponding samples decreased due to partial destruction of intermolecular or/ and intramolecular hydrogen bond network. The CI (TCI) values for cellulose I/II hybrid fibers were smaller than that of pure cellulose I or cellulose II. The properties of cellulose I/II hybrid characterized in this study can provide some fundamental information for the potential application of cellulose I/II hybrid fibers in some anticipated fields, such as clothing, cosmetic, pharmaceuticals, biomedicine and smart materials.

3.5 REFERENCES

Agarwal, U.P., Zhu, J.Y., Ralph, S.A., 2013. Enzymatic hydrolysis of loblolly pine: effects of cellulose crystallinity and delignification. Holzforschung 67, 371-377.

Azubuike, C.P., Rodriguez, H., Okhamafe, A.O., Rogers, R.D., 2012. Physicochemical properties of maize cob cellulose powders reconstituted from ionic liquid solution. Cellulose 19, 425-433.

Borysiak, S., Garbarczyk, J., 2003. Applying the WAXS method to estimate the supermolecular structure of cellulose fibres after mercerisation. Fibres and Textiles in Eastern Europe 11, 104-106.

Carrillo, A., Colom, X., Sunol, J.J., Saurina, J., 2004. Structural FTIR analysis and thermal characterisation of lyocell and viscose-type fibres. European Polymer Journal 40, 2229-2234.

Chen, W.H., Tu, Y.J., Sheen, H.K., 2011. Disruption of sugarcane bagasse lignocellulosic structure by means of dilute sulfuric acid pretreatment with microwave-assisted heating. Applied Energy 88, 2726-2734.

Correa, A.C., Teixeira, E.D., Pessan, L.A., Mattoso, L.H.C., 2010. Cellulose nanofibers from curaua fibers. Cellulose 17, 1183-1192.

French, A.D., Santiago Cintrón, M., 2013. Cellulose polymorphy, crystallite size, and the Segal Crystallinity Index. Cellulose 20, 583-588.

Han, J.Q., Zhou, C.J., French, A.D., Han, G.P., Wu, Q.L., 2013a. Characterization of cellulose II nanoparticles regenerated from 1-butyl-3-methylimidazolium chloride. Carbohydrate Polymers 94, 773-781.

Han, J.Q., Zhou, C.J., Wu, Y.Q., Liu, F.Y., Wu, Q.L., 2013b. Self-Assembling Behavior of Cellulose Nanoparticles during Freeze-Drying: Effect of Suspension Concentration, Particle Size, Crystal Structure, and Surface Charge. Biomacromolecules 14, 1529-1540.

Hubbell, C.A., Ragauskas, A.J., 2010. Effect of acid-chlorite delignification on cellulose degree of polymerization. Bioresource Technology 101, 7410-7415.

Isogai, A., Atalla, R.H., 1998. Dissolution of cellulose in aqueous NaOH solutions. Cellulose 5, 309-319.

Kamide, K., Kowsaka, K., Okajima, K., 1985. Determination of intramolecular hydrogen bonds and selective coordination of sodium cation in alkali cellulose by CP/MASS 13C NMR. Polymer Journal 17, 707-711.

Keusch, S., Haessler, R., 1999. Influence of surface treatment of glass fibres on the dynamic mechanical properties of epoxy resin composites. Composites Part a-Applied Science and Manufacturing 30, 997-1002.

Kim, M., Day, D.F., 2011. Composition of sugar cane, energy cane, and sweet sorghum suitable for ethanol production at Louisiana sugar mills. Journal of Industrial Microbiology & Biotechnology 38, 803-807.

Kljun, A., Benians, T.A.S., Goubet, F., Meulewaeter, F., Knox, J.P., Blackburn, R.S., 2011. Comparative Analysis of Crystallinity Changes in Cellulose I Polymers Using ATR-FTIR, X-ray Diffraction, and Carbohydrate-Binding Module Probes. Biomacromolecules 12, 4121-4126.

Kumar, V., Reus-Medina, M.D.L., Yang, D., 2002. Preparation, characterization, and tabletting properties of a new cellulose-based pharmaceutical aid. International Journal of Pharmaceutics 235, 129-140.

Kuo, C.H., Lee, C.K., 2009. Enhancement of enzymatic saccharification of cellulose by cellulose dissolution pretreatments. Carbohydrate Polymers 77, 41-46.

Langford, J.I., Wilson, A.J.C., 1978. Scherrer after sixty years: a survey and some new results in the determination of crystallite size. Journal of Applied Crystallography 11, 102-113.

Liu, Y., Hu, H., 2008. X-ray diffraction study of bamboo fibers treated with NaOH. Fibers and Polymers 9, 735-739.

Lu, J., Askeland, P., Drzal, L.T., 2008. Surface modification of microfibrillated cellulose for epoxy composite applications. Polymer 49, 1285-1296.

Ma, H., Zhou, B., Li, H.S., Li, Y.Q., Ou, S.Y., 2011. Green composite films composed of nanocrystalline cellulose and a cellulose matrix regenerated from functionalized ionic liquid solution. Carbohydrate Polymers 84, 383-389.

Mandal, A., Chakrabarty, D., 2011. Isolation of nanocellulose from waste sugarcane bagasse (SCB) and its characterization. Carbohydrate Polymers 86, 1291-1299.

Mansfield, S.D., Meder, R., 2003. Cellulose hydrolysis - the role of monocomponent cellulases in crystalline cellulose degradation. Cellulose 10, 159-169.

Miura, K., Nakano, T., 2015. Analysis of mercerization process based on the intensity change of deconvoluted resonances of 13C CP/MAS NMR: Cellulose mercerized under cooling and non-cooling conditions. Materials Science and Engineering: C 53, 189-195.

Moubarik, A., Grimi, N., Boussetta, N., 2013. Structural and thermal characterization of Moroccan sugar cane bagasse cellulose fibers and their applications as a reinforcing agent in low density polyethylene. Composites Part B-Engineering 52, 233-238.

Mwaikambo, L.Y., Ansell, M.P., 2002. Chemical modification of hemp, sisal, jute, and kapok fibers by alkalization. Journal of Applied Polymer Science 84, 2222-2234.

Nelson, M.L., O'Connor, R.T., 1964. Relation of certain infrared bands to cellulose crystallinity and crystal lattice type. Part II. A new infrared ratio for estimation of crystallinity in celluloses I and II. Journal of Applied Polymer Science 8, 1325–1341.

Newman, R.H., Davies, L.M., Harris, P.J., 1996. Solid-state C-13 nuclear magnetic resonance characterization of cellulose in the cell walls of Arabidopsis thaliana leaves. Plant Physiology 111, 475-485.

Oh, S.Y., Yoo, D.I., Shin, Y., Kim, H.C., Kim, H.Y., Chung, Y.S., Park, W.H., Youk, J.H., 2005. Crystalline structure analysis of cellulose treated with sodium hydroxide and carbon dioxide by means of X-ray diffraction and FTIR spectroscopy. Carbohydrate Research 340, 2376-2391.

Park, S., Baker, J.O., Himmel, M.E., Parilla, P.A., Johnson, D.K., 2010. Cellulose crystallinity index: measurement techniques and their impact on interpreting cellulase performance. Biotechnology for Biofuels 3, 1-10.

Qi, H.S., Cai, J., Zhang, L.N., Kuga, S., 2009. Properties of Films Composed of Cellulose Nanowhiskers and a Cellulose Matrix Regenerated from Alkali/Urea Solution. Biomacromolecules 10, 1597-1602.

Qiu, Z.H., Aita, G.M., 2013. Pretreatment of energy cane bagasse with recycled ionic liquid for enzymatic hydrolysis. Bioresource Technology 129, 532-537.

Rezende, C.A., de Lima, M.A., Maziero, P., deAzevedo, E.R., Garcia, W., Polikarpov, I., 2011. Chemical and morphological characterization of sugarcane bagasse submitted to a delignification process for enhanced enzymatic digestibility. Biotechnology for Biofuels 4, 1-18.

Santi, C., Milagres, A.M.F., Ferraz, A., Carvalho, W., 2013. The effects of lignin removal and drying on the porosity and enzymatic hydrolysis of sugarcane bagasse. Cellulose 20, 3165-3177.

Segal, L., Creely, J., Martin, A., Conrad, C., 1959. An empirical method for estimating the degree of crystallinity of native cellulose using the X-Ray diffractometer. Textile Research Journal 29, 786-794.

Siroky, J., Blackburn, R.S., Bechtold, T., Taylor, J., White, P., 2010. Attenuated total reflectance Fourier-transform Infrared spectroscopy analysis of crystallinity changes in lyocell following continuous treatment with sodium hydroxide. Cellulose 17, 103-115.

Sun, J.X., Sun, X.F., Zhao, H., Sun, R.C., 2004a. Isolation and characterization of cellulose from sugarcane bagasse. Polymer Degradation and Stability 84, 331-339.

Sun, J.X., Xu, F., Sun, X.F., Sun, R.C., Wu, S.B., 2004b. Comparative study of lignins from ultrasonic irradiated sugar-cane bagasse. Polymer International 53, 1711-1721.

Sun, R.C., Tomkinson, J., Zhu, W., Wang, S.Q., 2000. Delignification of maize stems by peroxymonosulfuric acid, peroxyformic acid, peracetic acid, and hydrogen peroxide. 1. Physicochemical and structural characterization of the solubilized lignins. Journal of Agricultural and Food Chemistry 48, 1253-1262.

Sun, X.F., Sun, R.C., Su, Y.Q., Sun, J.X., 2004c. Comparative study of crude and purified cellulose from wheat straw. Journal of Agricultural and Food Chemistry 52, 839-847.

Thakur, V.K., Thakur, M.K., 2014. Processing and characterization of natural cellulose fibers/thermoset polymer composites. Carbohydrate Polymers 109, 102-117.

Thakur, V.K., Thakur, M.K., Gupta, R.K., 2013a. Rapid synthesis of graft copolymers from natural cellulose fibers. Carbohydrate Polymers 98, 820-828.

Thakur, V.K., Thakur, M.K., Gupta, R.K., 2013b. Synthesis of lignocellulosic polymer with improved chemical resistance through free radical polymerization. International Journal of Biological Macromolecules 61, 121-126.

Thakur, V.K., Thakur, M.K., Gupta, R.K., 2014. Review: Raw Natural Fiber-Based Polymer Composites. International Journal of Polymer Analysis and Characterization 19, 256-271.

Vanderhart, D.L., Earl, W.L., Garroway, A.N., 1981. Resolution in 13C NMR of organic solids using high-power proton decoupling and magic-angle sample spinning. Journal of Magnetic Resonance 44, 361-401.

Wen, J.L., Sun, S.N., Yuan, T.Q., Xu, F., Sun, R.C., 2013. Fractionation of bamboo culms by autohydrolysis, organosolv delignification and extended delignification: Understanding the fundamental chemistry of the lignin during the integrated process. Bioresource Technology 150, 278-286.

Yang, H.P., Yan, R., Chen, H.P., Lee, D.H., Zheng, C.G., 2007. Characteristics of hemicellulose, cellulose and lignin pyrolysis. Fuel 86, 1781-1788.

Yoneda, Y., Mereiter, K., Jaeger, C., Brecker, L., Kosma, P., Rosenau, T., French, A., 2008. van der Waals versus Hydrogen-Bonding Forces in a Crystalline Analog of Cellotetraose: Cyclohexyl 4 '-O-Cyclohexyl beta-D-Cellobioside Cyclohexane Solvate. Journal of the American Chemical Society 130, 16678-16690.

Yue, Y.Y., Han, J.Q., Han, G.P., Aita, M.G., Wu, Q.L., 2015. Cellulose fibers isolated from energycane bagasse using alkaline and sodium chlorite treatments: structural, chemical and thermal properties. Industrial Crops and Products 76, 355-363.

Yue, Y.Y., Zhou, C.J., French, A.D., Xia, G., Han, G.P., Wang, Q.W., Wu, Q.L., 2012. Comparative properties of cellulose nano-crystals from native and mercerized cotton fibers. Cellulose 19, 1173-1187.

Zuckerstätter, G., Schild, G., Wollboldt, P., Röder, T., Weber, H.K., Sixta, H., 2009. The elucidation of cellulose supramolecular structure by 13 C CP-MAS NMR. Lenzinger Berichte 87, 38-46.

Zuckerstätter, G., Terinte, N., Sixta, H., Schuster, K.C., 2013. Novel insight into cellulose supramolecular structure through 13C CP-MAS NMR spectroscopy and paramagnetic relaxation enhancement. Carbohydrate Polymers 93, 122-128.

CHAPTER 4 NANOCELLULOSE REINFORCED SODIUM ALGINATE-POLYVINYL ALCOHOL HYDROGELS: CORE-SHELL STRUCTURE FORMATION AND PROPERTY CHARACTERIZATION

4.1 INTRODUCTION

Hydrogels, which can hold a large amount of water, may be constructed from biocompatible and biodegradable materials. The characteristics of hydrogels can be tuned to be similar to human tissues, making them particularly attractive in the fields of implantable artificial organs, drug delivery, cell encapsulation and biosensors (Cushing and Anseth, 2007; Seliktar, 2012; Perez et al., 2015). However, most hydrogels are soft. Their low mechanical strength and variable dimensions with water content changes severely restrict their range of applications (Sun et al., 2012; Zhang et al., 2015). Increased attention has thus been paid to novel hydrogel architectures including core–shell and interpenetrating network (IPN) structures that offer improved strength and smaller swelling ratios (Yang et al., 2014; Zhang et al., 2015). In recent years, core-shell or IPN structured hydrogels have found use as biomaterials and adsorbents (Kan et al., 2014; Perez et al., 2015; Zhang et al., 2015). IPNs can be classified as either semi-IPNs (SIPN) or full-IPNs. SIPNs are cross-linked linear polymer structures and IPNs consist of at least two polymers, in which one polymer networks is cross-linked in the presence of the other polymer network (Dragan, 2014; Berrebi et al., 2015; Zhang et al., 2015). IPN and SIPN structures can improve the mechanical performance and dimensional stability of functional hydrogels (Yang et al., 2014; Berrebi et al., 2015).

Sodium alginate (SA) is a linear polymer comprising 1,4-linked-β-D-mannuronic acid (M) and α-L-guluronic acid (G) units, combined in blocks of M-M, G-G and M-G (Lee and Mooney, 2012; Bidarra et al., 2014). Due to its aqueous-solubility, biocompatibility, non-toxicity, non-immunogenicity, biodegradability and acceptance by human body (Yang et al., 2014; Zhang et

al., 2015), SA is a valuable biopolymer that is widely used in the textile industry (as a base for dyes), foods, biomedicines, pharmaceuticals and encapsulation materials (Lee and Mooney, 2012; Bidarra et al., 2014; Dragan, 2014). SA is hydrophilic, absorbing water quickly. Its –COOH and –OH groups participate in hydrogen bonding and van der waals force; therefore, it is an excellent natural adsorbent and is commonly used for removal of water pollutants, such as heavy metal ions, dyes, fertilizer, microorganisms and enzymes (Papageorgiou et al., 2012; Aftab et al., 2014). At a pH level of 4, the maximum amounts of –COOH groups in G units are deprotonated to -COO^-, which permits facile cross-linking by multivalent cations, such as Ca^{2+}, to form SIPN by chelation (Sun et al., 2012; Bidarra et al., 2014; Dragan, 2014; Samanta and Ray, 2014). Usually, the SA-Ca^{2+} structure is formed only in the shell of hydrogels (Dragan, 2014). Compared to the rigid SA, poly (vinyl alcohol) (PVA), with one –OH group in each repeating unit, is more flexible (Cho et al., 2009). Therefore, PVA can be blended with SA to improve the flexibility of SA matrixes. PVA/SA blends exhibit good compatibility in aqueous solutions (Cho et al., 2009), and they can be chemically crosslinked with glutaraldehyde (GA), a commonly used crosslinking agent, to form IPN (Jao et al., 2009).

Although core-shell structures can significantly enhance the toughness of hydrogels by three-dimensional physical and/or chemical cross-linkages (Cushing and Anseth, 2007; Perez et al., 2015), the mechanical behavior of most hydrogels is still not satisfactory for some applications. To further improve hydrogel performance, adsorption capability, and dimensional stability, cellulose nanoparticles (CNPs) extracted from energycane bagasse were used to reinforce hydrogels (Thakur and Thakur, 2014). Compared to other nanofillers, such as resin, metallic, or silica nanoparticles as well as carbon nanotubes, CNPs are attractive, due to the characteristics of biocompatibility, availability, low density, non-toxicity, hydrophilicity,

biodegradability and high crystallinity (Dash et al., 2013; Yang et al., 2013; Mounika and Ravindra, 2015; Ummartyotin and Manuspiya, 2015). Because of the hydrophilic nature of PVA and SA, the CNPs could crosslink with hydrogen bond of the PVA/SA matrix to stabilize hydrogel (Ummartyotin and Manuspiya, 2015). Moreover, CNPs with high tensile modulus can act as decelerators of propagating cracks and retard the failure of the hydrogel (Shin et al., 2009).

In the present study, novel hydrogels with core-shell structures were fabricated by casting PVASA-GA complexes (IPN core) in $CaSO_4$ solution to form robust a Ca^{2+}-SA shells. The objective was to determine the structure and characteristics of the hydrogels with and without the CNFs to learn their effects on the characteristics of the hydrogel. These hydrogels exhibited promising properties, including high mechanical strength and excellent adsorption-desorption capacity. Specifically, the effects of CNPs on the morphology, light transmittance, compression modulus, and dye adsorption-desorption behavior were studied. Insights into the viscoelastic changes and thermal stability that occurred when incorporating CNPs were obtained from oscillation rheology and thermal degradation tests. A gelation mechanism for the hydrogel was also proposed for a better understanding of the core-shell 3D network structure. To the best of our knowledge, we are unaware of any work on IPN core-SIPN shell structured hydrogels. In addition, the impacts of cellulose I/II hybrid extracted from energycane bagasse on IPN networks have not been assessed. The designed structure of a good ductility core and a high strength shell greatly improved the performance of the hydrogel, making it a suitable candidate in the areas of biosensors.

4.2 MATERIALS AND METHODS

4.2.1 Materials

Cellulose I and cellulose I/II hybrid fibers (44% cellulose I and 56% cellulose II) were isolated from energycane bagasse by $NaOH/NaClO_2$ treatment as described in our previous work (Yue et al., 2015a; Yue et al., 2015b). Poly (vinyl alcohol) (PVA) (average M_w 30,000-70,000), sodium alginate (SA) and methyl blue (MB) were obtained from Sigma-Aldrich Inc (St. Louis, MO, USA). Glutaraldehyde (25%) (GA) and sodium hydroxide were purchased from Fisher Scientific Inc (Fair Lawn, NJ, USA). Calcium sulfate and sodium phosphate were supplied by EMD Chemicals (Billerica, MA, USA). Distilled water was used in the preparation of all solutions.

4.2.2 Preparation of CNFs and CNCs

To obtain nanocrystals with the cellulose I structure (CNC I), the pretreated cellulose I fibers were dispersed in sulfuric acid (64 wt%) with a fiber-to-acid weight ratio of 1:10 at 45 ℃. The mixture was continuously agitated for 1h and diluted 5-fold to stop the reaction. The suspension was then centrifuged at 12,000 rpm for 10 min. The resulting sediment was washed with distilled water five times to separate the cellulose slurry from the acid solution. The slurry was then placed in regenerated dialysis tubes (Fisher Scientific, Pittsburgh, PA, USA) with a molecular weight cutoff of 12,000–14,000 and dialyzed against distilled water until neutral pH was reached. To further disperse and reduce the size of the cellulose fragments, the dialyzed suspension was processed through a high-pressure homogenizer (Microfluidizer M-110P, Microfluidics Corp., Newton, MA, USA) equipped with a pair of Z-shaped interaction chambers (one 200 μm ceramic, and one 87 μm diamond) under an operating pressure of 207 MPa for 10 passes.

The cellulose I/II structure fibers were utilized to produce cellulose nanocrystals with cellulose I/II hybrid structure (CNC I/II), and all the treatment processes were the same as those applied for CNC I. For the cellulose I and cellulose I/II nanofibers (CNF I and CNF I/II), sulfuric acid (48 wt%) was employed and the other treatments were identical with those for CNC I. The resulting cellulose aqueous suspensions were adjusted to a 1.0% concentration level and then stored in a refrigerator at 10 ℃. All the cellulose samples were designated as CNPs.

4.2.3 Preparation of core-shell structure hydrogels

The core-shell structured hydrogels were prepared by crosslinking PVA and SA using GA and calcium sulfate with or without the presence of CNPs (Figure 4.1). PVA (2.0 w/v%) and SA powder (2.0 w/v%) were slowly added in 1.0 wt% CNP aqueous suspension at 20 ℃. After 4h of vigorous mechanical stirring at a speed of 300 rpm/min, homogeneous suspensions were obtained. H_2SO_4 (20 wt%) was then added to the suspension to reach the target pH of 4. The resultant materials were then cross-linked with GA (3.0 v/v%) in nitrogen atmosphere for 2 days to form the hydrogel core. After the semi-fluid core materials were obtained, they were transferred to a mold placed in a glass beaker and an aqueous solution mixture with $CaSO_4$ (0.015mol/L) and anhydrous Na_2HPO_4 (0.015mol/L) was poured into the beaker to form the shell. After 30 minutes of immersion, core-shell structured hydrogels were formed. Core-Shell-CNP was used as a generic designation for hydrogel with CNPs (CNC I, CNC I/II, CNF I and CNF I/II) in comparison with the hydrogel without CNPs (Core-Shell). The core, crosslinking of PVA/SA with GA, was designated as PSG, whereas the shell, chelating of calcium ions with alginate, was designated as CA. For example, the hydrogel without CNPs is designated as PSG-CA and the hydrogel with CNC I is designated as PSG-CA-CNC I. For purposes of analysis, shells were separated from the core-shell hydrogels by cutting open the hydrogel and rinsing out

the core. For separate core samples, some hydrogel was selected prior to the step of placing in the mold and adding $CaSO_4$. The cores and shells were then freeze-dried using a freeze-dryer (FreeZone, 2.5 plus, Labconco Corp., Kansas City, MO, USA) for further analysis.

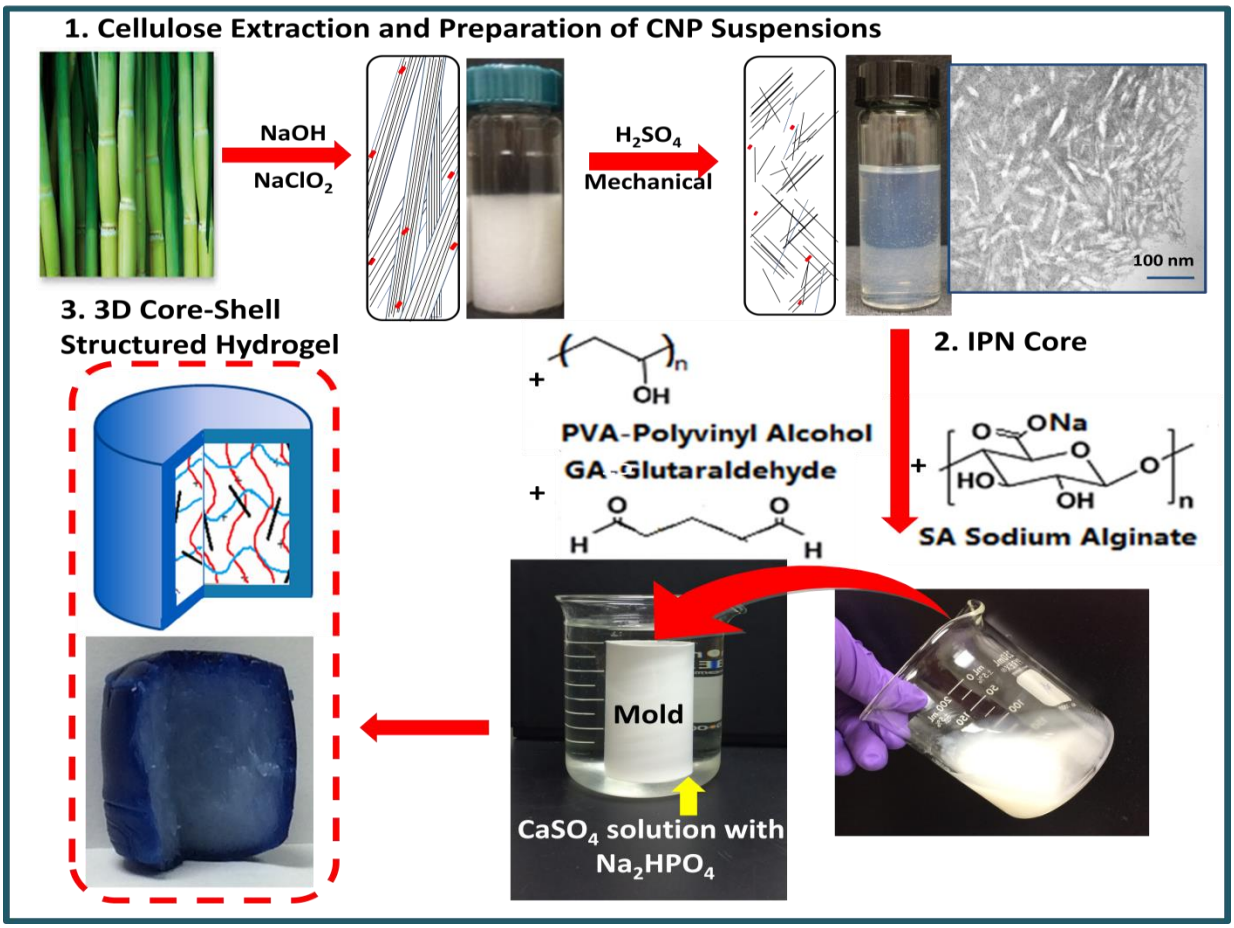

Figure 4.1 Scheme for preparation of 3D core-shell structured PSG-CA-CNPs hydrogel.

4.2.4 Characterizations

4.2.4.1 Morphology of CNPs

Transmission Electron Microscopy (TEM) (JEOL 100CX, JEOL USA, Inc) with an accelerating voltage of 80 kV was used to investigate the morphology of CNPs. A droplet of CNP (0.1 wt%) aqueous suspension was spread on a carbon coated copper grid. After a few minutes drying in air and adsorbing with filter paper, a small drop of uranyl acetate (2 wt%) was

used to stain the sample to improve the contrast. The dimensions of captured CNPs were measured using Image J. For each sample, over 50 samples were randomly selected and averaged for the results.

4.2.4.2 Morphology of core-shell hydrogels

The morphology of the freeze-dried hydrogels were characterized using an environmental scanning electron microscope (ESEM) (FEI QuantaTM 3D FEG Dual Beam SEM/ FIB, Hillsboro Oregon, USA). Prior to analysis, the samples with the diameter of 10 mm were cooled by liquid nitrogen for 15 min and then impact fractured. The fractured face was sputter coated with Au and scanned at 5kV.

4.2.4.3 Fourier Transform Infrared Spectrometry (FTIR)

All the freeze-dried hydrogel samples were characterized in the dry state by a Bruker FTIR analyzer (Tensor-27, Bruker Optics Inc., Billerica, MA, USA) with an attenuated total reflectance (ATR) mode. Measurements were taken in the range of 4000-600 cm−1 with a resolution of 4 cm−1. An average of 64 scans was collected in each of three replicated measurements.

4.2.4.4 Thermal Degradation

Thermal pyrolysis characterization of the freeze dried shell and core was performed with a TGA Q50 Analyzer (TA Instruments, New Castle, DE, USA) under N_2 purge at a flow rate of 60 ml/min. Before measurement, each sample was oven-dried at 40 ℃ for 2h to remove the moisture in hydrogels. The samples (3-10 mg) were equilibrated at 30 ℃ and kept for 4 min to obtain an isothermal condition. The specimen was then heated from 30 to 600 ℃ at a heating rate of 10 ℃ /min. Three repeated experiments were conducted for each measurement.

4.2.4.5 UV Absorbance

Transmittance of the hydrogel and CNP suspensions was studied with a UV-vis spectrophotometer (Evolution 600 PC, Thermo Electron Co., Waltham, MA, USA). The diameter of the hydrogel sample was in the range of 9-11 mm. Each sample was placed into a UV quartz cuvette with PTFE cover (dimension of 45 ×12.5× 12.5 mm). The wavelength was monitored from 300 to 800 nm with a scan speed of 240nm/min. Distilled water was used as reference for all of the samples. Each sample was measured three times and all tests were carried out at 20 ℃.

4.2.4.6 Dynamic Oscillation Rheology Measurements

The rheological experiments were carried out with an AR-2000EX rheometer (TA Instruments, New Castle, DE) for dynamic strain, frequency and flow sweep tests. Before the viscoelastic measurements, dynamic strain sweep was run using parallel-plate geometry (40 mm diameter) to determine the linear viscoelastic region (LVR). The sweep of strain (ε) from 0.05 to 100% was selected for the tests. The frequency sweep was carried out to measure shear storage modulus (G') and loss modulus (G'') as functions of angular frequency (ω) over the range of 1 to 100 rad/s. To determine the viscosity (η) for PSG-CA-CNP cores and the 1.0 wt% CNP colloidal suspensions, dynamic flow sweep was investigated with the shear rate (γ) from 0.1 to 100 s^{-1} using cone-plate geometry (40 mm diameter, 1°59’42” cone angle, truncation cap 52 μm). All the experiments were carried out at 25 ° C and all samples were equilibrated for 2 min before measurements. To prevent evaporation of moisture, the edge around the plate was sealed with low viscosity silicon oil and the solvent trap cover was placed on the plate. Each measurement was repeated three times.

4.2.4.7 Density, Water content and Compression Tests

The density (ρ, g/cm^3) of hydrogel was calculated based on its weight (M_d) and volume (V_d) using the Equation [4.1]. The water content of the hydrogel was determined by gravimetric methods and calculated according to Equation [4.2]:

$$\rho = \frac{M_d}{V_d} \qquad [4.1]$$

$$W_c = \frac{M_h - M_o}{M_o} \times 100\% \qquad [4.2]$$

where M_h is the initial weight of hydrogel and M_o is the weight of the hydrogel after drying in a vacuum oven at 40 ℃ until the weight is constant.

Compression tests were performed on the hydrogels using an AR-2000EX rheometer (TA Instruments, New Castle, DE). The hydrogel samples, 40 mm in diameter and 20 mm in height, were placed on the stationary peltier plate, and a uniaxial parallel plate with a diameter of 40 mm was used to press against the sample at a cross head speed of 20 μm/s and 25 ℃. The normal force was set at 50 N to make sure that the measurements were ended when the maximum loading reached 50 N. Compressive stress and strain were obtained from measured force and displacement based on initial height of the hydrogels. To examine the reproducibility of the results from compressive tests, replicate measurements were performed.

4.2.4.8 Adsorption and desorption of MB

Adsorption experiments were carried out in 100 ml MB solution with concentration ranging from 0.05 to 0.15 g/L at 25 ℃. Hydrogel (0.1g-0.4g) was added into the MB solution and removed after reaching absorbent equilibrium. The adsorption capacity of PSG-CA-CNC I, PSG-CA-CNC I/II, PSG-CA-CNF I, PSG-CA-CNF I/II, PSG-CA was determined by UV–vis spectrophotometer (Evolution 600 PC, Thermo Electron Co., Waltham, MA, USA) at the

wavelength of 664 nm. The amount of MB adsorbed per unit hydrogel mass at equilibrium q_e (mg/g) was calculated from the following mass balance equation.

$$q_e = (C_0 - C_e) \times \frac{V}{m} \qquad [4.3]$$

Where C_0 and C_e (mg/L) are the initial and equilibrium MB concentrations, respectively; V(L) is the volume of the MB solution, and m(g) is the mass of hydrogel.

Desorption was effected by washing the hydrogel surface with distilled water at room temperature for 10 min.

4.3 RESULTS AND DISCUSSION

4.3.1 Morphology of CNP colloidal suspensions

Figure 4.2 presents the dimension of CNPs by different chemical treatments. The dimensions of CNPs were significantly different depending on the preparation approach, showing that the particle size can be successfully controlled by changing acid and alkali concentrations. Both CNP I (native cellulose) and CNP I/II hybrid were utilized in this study. CNP I/II hybrid was choosen because it offered the favorable morphology, thermal stability and mechanical properties properties of both CNP I and CNP II (Yue et al., 2015b). The four kinds of CNPs as shown in Table 4.1 were used for the subsequent tests. The lengths of CNC I isolated from bagasse and their aspect ratio were in accordance with those of previous work (Bras et al., 2011). However, the lengths of obtained CNF I were shorter than those of reported CNFs obtained from wood (Han et al., 2013b), suggesting that the particle sizes were affected by material sources and/or treatment conditions. In this study, CNPs were obtained by a combination of NaOH, $NaClO_2$, H_2SO_4 and mechanical treatments (step 1 in Figure 4.1). Thus, these treatment conditions contributed to the smaller CNP dimensions.

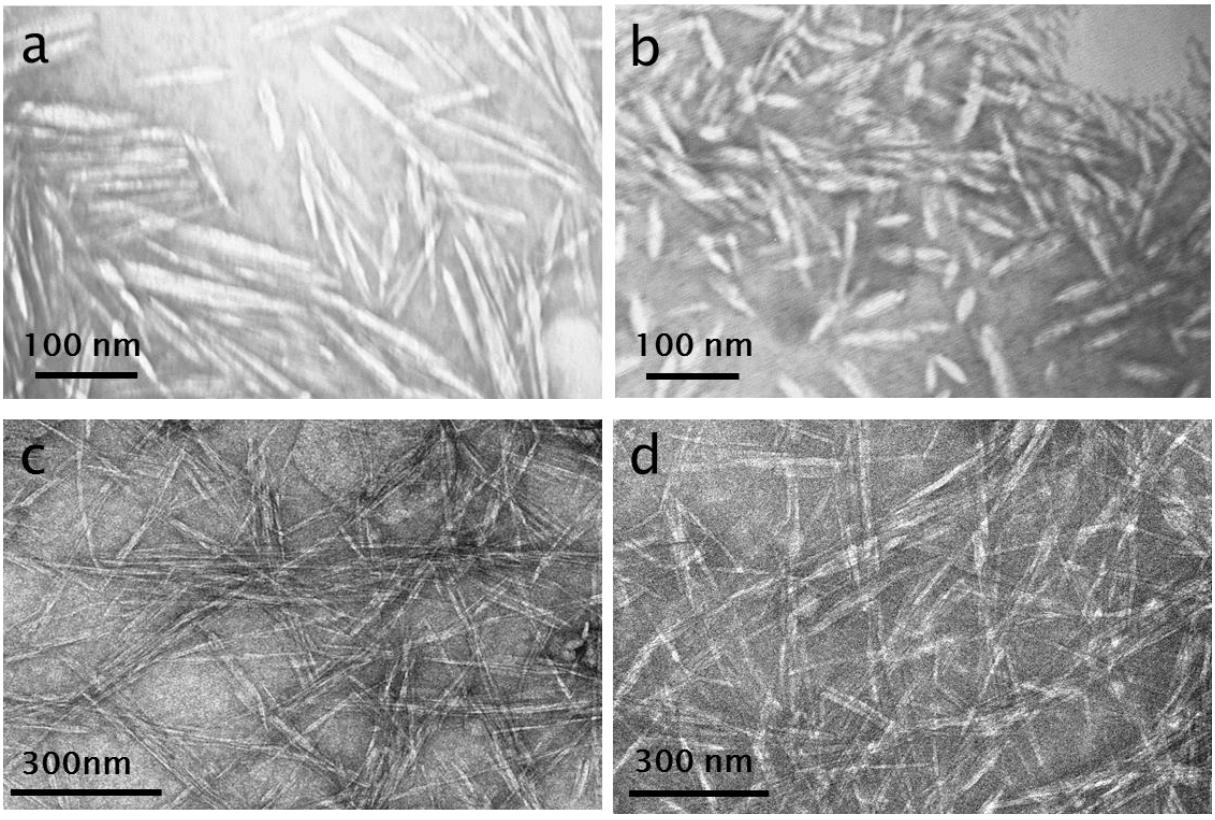

Figure 4.2 TEM pictures of (a) CNC I; (b) CNC I/II; (c) CNF I; (d) CNF I/II at the 1.0 wt% concentration level.

Table 4.1 The dimension of cellulose nanoparticles after various treatments

parameter	CNC I	CNC I/II	CNF I	CNF I/II
Length	154 ±72	98 ±54	485 ±168	367 ±103
width	11 ±4	9 ±3	21 ±7	17 ±6
Aspect ratio	14.00	10.89	23.10	21.59

4.3.2 Microstructure core-shell structured hydrogel

The core-shell structured hydrogels were prepared as illustrated in Figure 4.1 (steps 2 and 3) and the SEM images of the hydrogels are shown in Figure 4.3. Figures 4.3a and b show that the hydrogels possessed a micro-porous shell and a macro-porous core. Pores with diameters ranging from 5 to 40 μm were formed in the core due to high water content (≥ 93%) in the cores

(Figure 4.3c), demonstrating that PVA-SA hydrogels possessed comparatively large surface area and porous structure (Thankam et al., 2013). The shell is a compact membrane wrapping the core. Figure 4.3d displays the rough and crazed shell surface. The thickness of the shell was 60 ± 11 μm and pores in the cross-section of the shell were around 2 ± 0.8 μm (Figure 4.3e). Apparently, the morphology of the core–shell structure was strongly affected by the formation of the chemical bonds. The egg box junctions between Ca^{2+} and $–COO^-/OH^-$ resulted in a compact, dense, micro-porous structure in the shell and the covalent bonding though PVA-SA and GA led to a looser, macro-porous structure in the core. To further illustrate the core-shell structure, the hydrogel was immersed in methyl blue for 10 minutes and then washed with distilled water several times. Because of the compactness of the shell, incomplete washing could not fully desorb the dye from the shell. However, the dye in the core area was rinsed out owing to the macro-porous and loose nature of the core, resulting in the stained shell and uncolored core (Figure 4.3f).

The morphology of the PSG-CA-CNC I and PSG-CA-CNF I cores are detailed in Figures 4.3g-j. Both CNF I and CNC I are agglomerated into micro-sized bundles by strong hydrogen bonding, and these CNP bundles are well dispersed in the PVA/SA matrix, resulting in significantly improved mechanical performance. Moreover, the porous macro-structure significantly enlarged the surface area in the core, and it facilitated the movement of dye particle and metal ions within the core network. This resulted in a high adsorption capability. As discussed later, the improved mechanical and adsorption characteristics were further verified by compression stress-strain and adsorption tests.

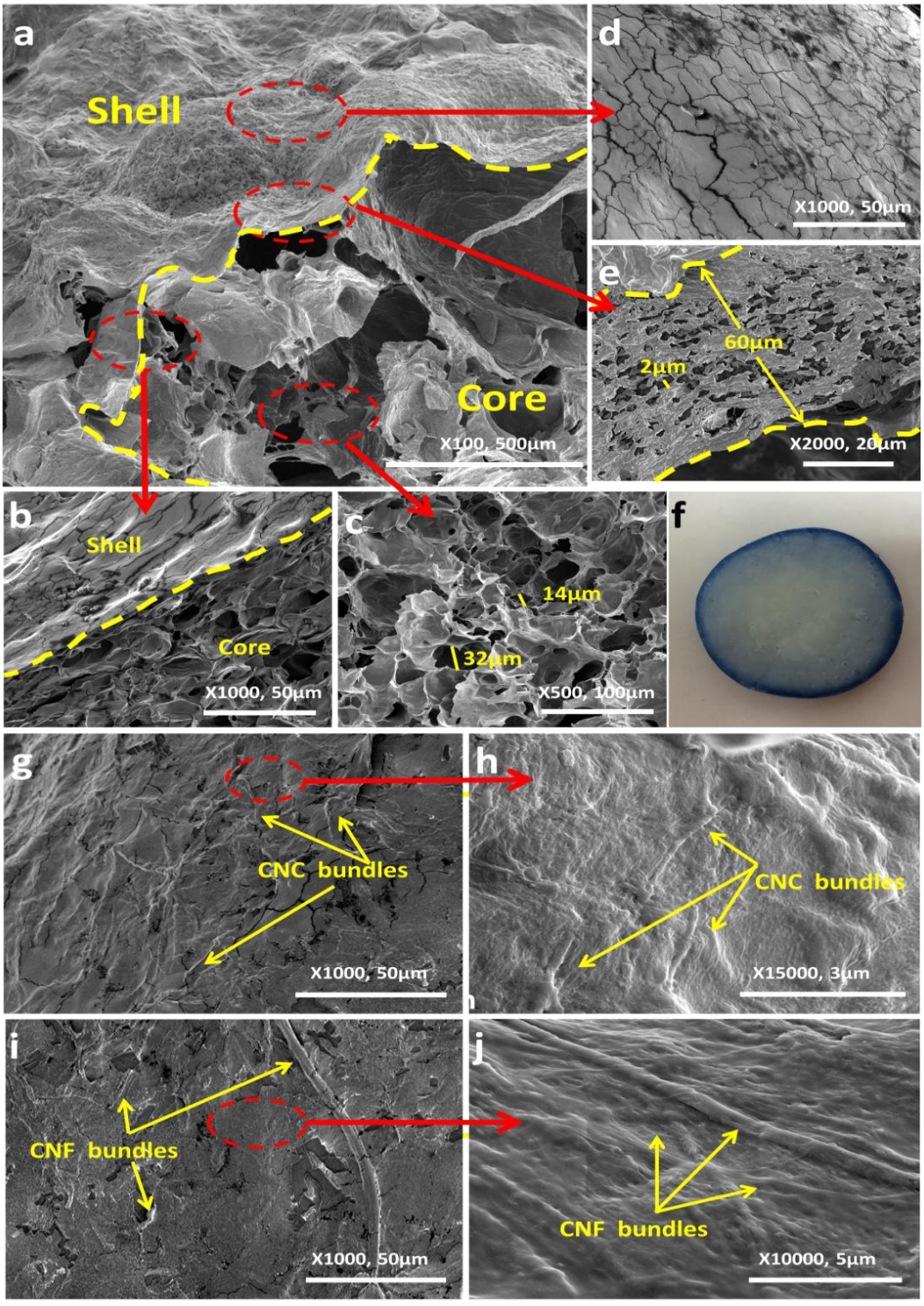

Figure 4.3 The morphology of hydrogels: (a) SEM images of freeze-dried core-shell structured hydrogel, (b-e) enlarged view of the marked areas in (a); and (f) optical micrograph of a cross section of core-shell structured hydrogel after dyeing and rinsing; (g) hydrogel core with 1.0 wt% CNC I and (h) enlarged view of the marked regions in (g); (i) hydrogel core with 1.0 wt% CNF I and (j) amplified view of the marked regions in (i).

4.3.3 PVA/SA Complex Structure by FTIR

Figure 4.4 shows the FTIR spectra of CNC I, CNC I/II, as well as the spectra of the core and shell networks with different types of CNPs. Because the chemical composition of CNCs and CNFs are almost identical, the spectra for PSG-CA-CNC I and PSG-CA-CNC I/II are displayed as examples. Also, the chemical structure change in the shell was basically unnoticeable by FTIR with the incorporation of small amount of CNPs, leading to similar FTIR spectra for all prepared shells. Therefore, only one curve for the shell is exhibited in Figure 4.4.

For CNPs, after alkali treatment, the bands arising from the intramolecular –OH groups at 3338 cm^{-1} disappeared and the new absorbance bands at 3488 cm and 3440 cm^{-1} were observed, indicating that the inter- and intramolecular hydrogen bond interactions were changed. In addition, the decreasing intensity of the bands at 1428, 1032 and 1110 cm^{-1}, originating from CH_2 wagging, C-O-C skeletal vibration and anti-symmetric ring stretching, evidenced that the new cellulose II crystals had formed (Yue et al., 2015b).

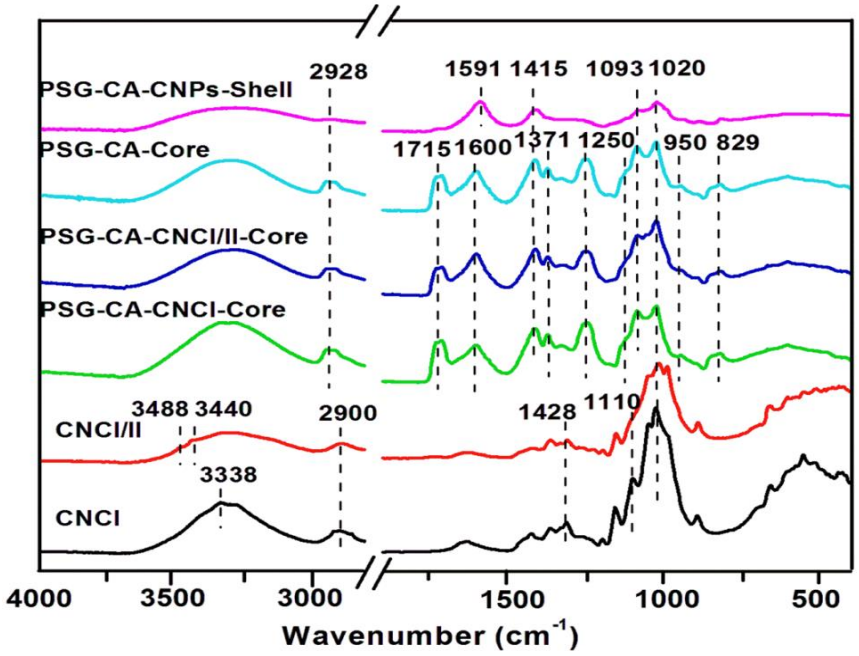

Figure 4.4 FTIR spectra of CNC I, CNC I/II, the core of PSG-CA-CNC I, PSG-CA-CNC I/II, PSG-CA and shell of PSG-CA-CNPs.

For the hydrogels, the bands around 3000-3600 cm^{-1} were assigned to –OH vibration for both core and shell in PSG-CA-CNPs. The intensities of these peaks for the shell were smaller than those for the core. A possible reason was that although the number of free -OH groups in the core of PSG-CA, PSG-CA-CNC I and PSG-CA-CNC I/II was reduced by the crosslinking, the excess of -OH groups in PVA still resulted in the increased intensity of the peaks. In addition, the band at 2928 cm^{-1} was attributed to C-H stretching and the bands at 1093 cm^{-1} and 1020 cm^{-1} were assigned to C-O stretching for both core and shell (Kahya et al., 2010; Thankam et al., 2013). Compared to the core, a small peak at 2928 cm^{-1} and the small peaks at 1093 cm^{-1} and 1020 cm^{-1} evidenced a small number of C-H and C-O groups in alginate (Jao et al., 2009; Thankam et al., 2013; Bekin et al., 2014).

A schematic representation of crosslinking reaction in core and shell is shown in Figure 4.5. The shell of PSG-CA-CNPs possessed SIPN structure, which was achieved through crosslinking of G units in alginate chains through Ca^{2+} cations in the presence of PVA (Sun et al., 2012; Thankam et al., 2013; Samanta and Ray, 2014). During this process, Na_2HPO_4, working as a crosslinking retardation agent, was used to slow gelation rates to form a uniform outer layer, resulting in dense and compact egg box junctions in a hydrogel shell (Cho et al., 2009; Dragan, 2014). The peaks around 1591 and 1415 cm^{-1} represented the anti-symmetric and symmetric stretching vibrations of $–COO^-$ groups in the shell, confirming the formation of SIPN (Kahya et al., 2010; Bekin et al., 2014). The core contained PVA and SA, and these two polymers reacted with GA independently (Zhang et al., 2015). The IPN structure was a "double network", generated by crosslinking -CHO groups in GA with –OH groups in PVA and SA to form acetals and ether linkages. This conclusion was supported by absorbance bands at 1371, 1250 and 950 cm^{-1} (Yeom and Lee, 1996; Kim et al., 2003). Besides the IPN structure, PVA and SA could be

cross-linked through hydrogen bonding and van der Waals forces, contributing to a physical entanglement and chemical crosslinked 3D network in the core. After crosslinking of PVA-SA and GA, the characteristic band at 1591 cm^{-1} corresponding to $-COO^-$ groups in alginate was shifted to 1600 cm^{-1}, which might be caused by the formation of IPN structure (Kahya et al., 2010). Apart from these peaks, the peak located at 1715 cm^{-1} arose from the stretching vibration of the C=O group in excess of GA (Yeom and Lee, 1996). The band at 829 cm^{-1} corresponded to the presence of Na-O bonds in sodium alginate (Bekin et al., 2014).

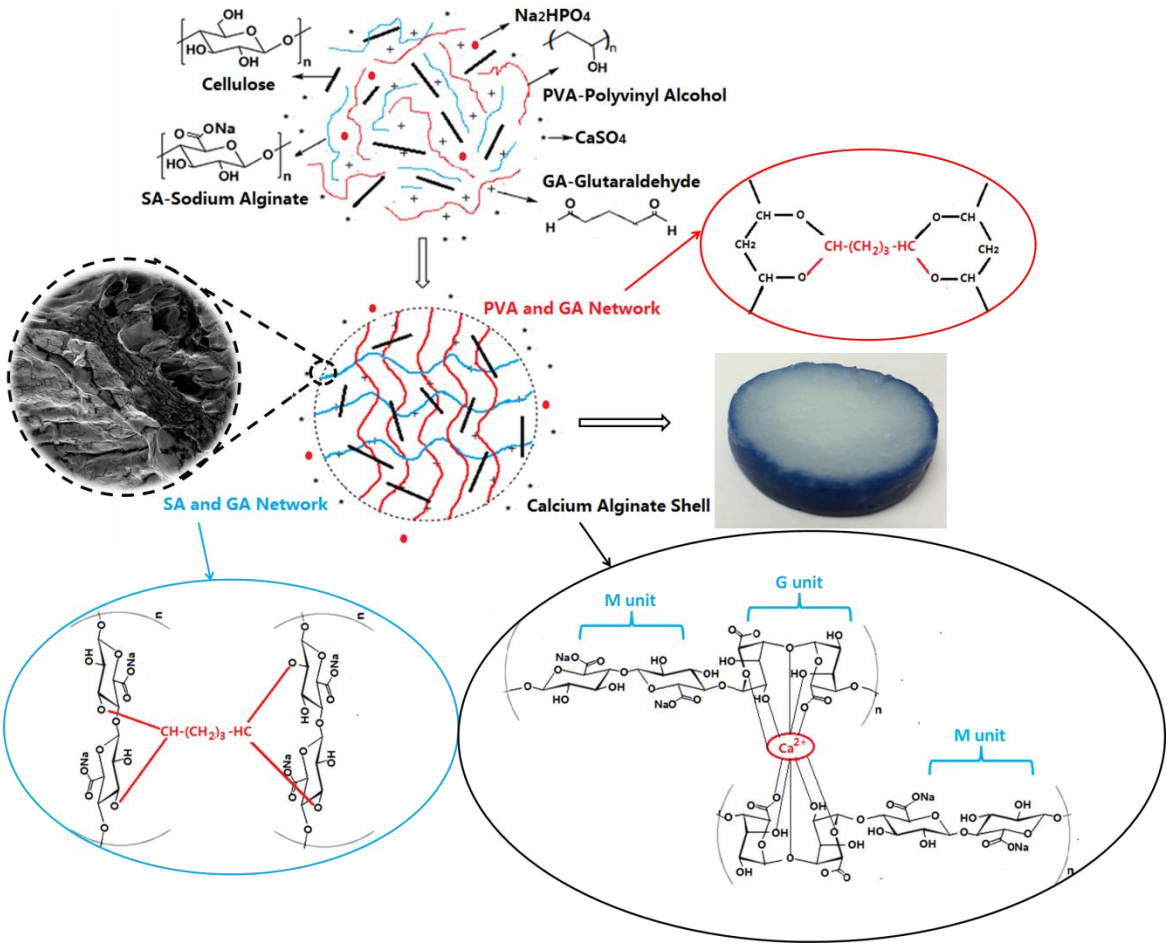

Figure 4.5 A schematic representation of the core-shell structured hydrogels

Compared to the egg box junctions in the shells, the crosslinking of PVA-SA with GA can be controlled more easily, and a longer crosslink length can be obtained (Bekin et al., 2014).

Owing to the loose and porous structure of the core, its strength and thermal stability were lower than those of the shell. However, the viscoelastic core can adsorb and distribute applied force under deformation, providing inner support for the hydrogels. Therefore, the combination of ductile core and rigid shell gives the hydrogels an ideal structure that can sustain a high stress.

4.3.4 Thermal Stability by TG

The TGA and DTG curves of core and shell incorporated CNPs are shown in Figure 4.6a and b, respectively. Table 4.2 lists the onset degradation temperature (T_0, ℃), maximum thermal degradation temperature (T_{max}, ℃), maximum weight loss rate (WLR_{max}, %/℃) and char yields (CY, %) at 600 ℃ for all the samples. A small weight loss in the range of 50-150 ℃ was ascribed to the loss of bound water (Yang et al., 2014; Lu et al., 2015). These bound water molecules did not release under previous drying at 40 ℃, implying they were tied to the PVA-SA chains through strong hydrogen bonds (Sajjan et al., 2013).

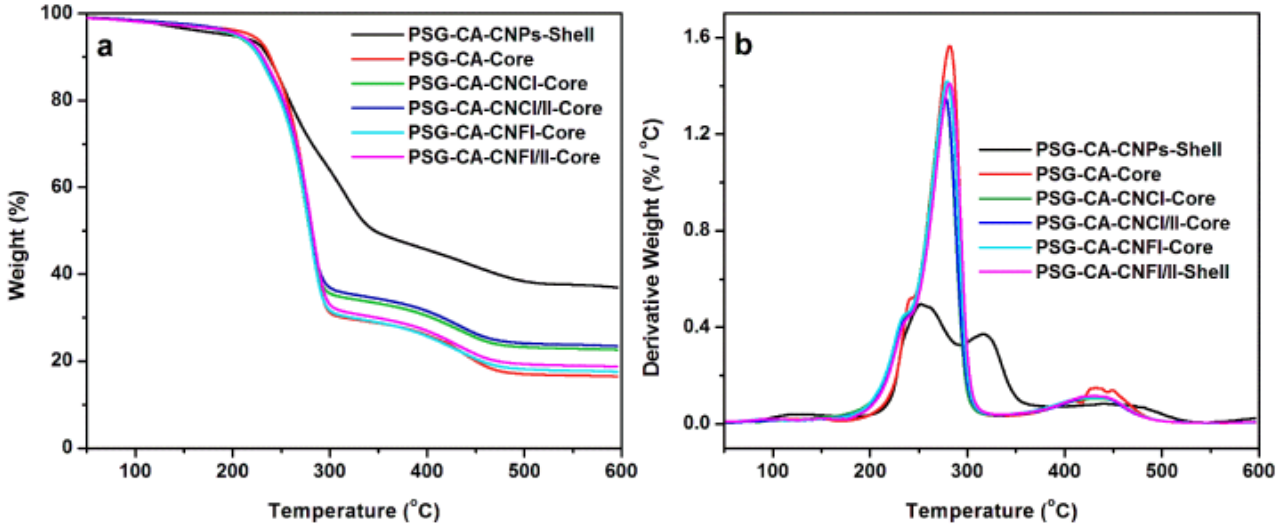

Figure 4.6 TGA (a) and DTG (b) curves of shell, PSG-CA core, PSG-CA-CNC I core, PSG-CA-CNC I/II core, PSG-CA-CNF I core, PSG-CA-CNF I/II core.

Table 4.2 Summary of thermal de-compositional variables during pyrolysis processes

Sample	T_0 (℃)[a]	Stage I		Stage II		Stage III		CY (%)[d]
		T_{max} (℃)[b]	WLR_{max} (%.℃$^{-1}$)[c]	T_{max} (℃)	WLR_{max} (%.℃$^{-1}$)	T_{max} (℃)	WLR_{max} (%.℃$^{-1}$)	
Shell of PSG-CA	230.7	256.1	0.49	316.7	0.37	457.7	0.08	37.31
Core of PSG-CA	227.4	243.4	0.52	281.5	1.57	437.1	0.15	16.64
Core of PSG-CA-CNC I	213.4	238.2	0.46	276.6	1.36	431.3	0.11	22.84
Core of PSG-CA-CNC I/II	214.7	239.4	0.45	277.2	1.35	432.4	0.11	23.72
Core of PSG-CA-CNF I	215.7	239.6	0.46	279.0	1.42	432.9	0.11	17.73
Core of PSG-CA-CNF I/II	217.5	240.6	0.45	281.4	1.41	434.5	0.12	18.91

[a] Onset degradation temperature
[b] Maximum thermal degradation temperature
[c] Maximum weight loss rate
[d] Char yields at 600 ℃

At 200 ℃, both the shell and core began a three-step pyrolysis. For the shell, the weight loss in the first (~ 25%) and second (~ 20%) stages corresponded to the decomposition of alginate and PVA chains associated with chain scission reactions (Sajjan et al., 2013; Kuila and Ray, 2014). The decomposition peak at 256.1 ℃ was greater than that at 316.7 ℃, indicating that SA was the dominant component in the shell. The third pyrolysis stage ranged from 384.9-536.1 with T_{max} of 457.7 ℃ was ascribed to the pyrolysis of PVA backbone and alginate carbonaceous matter (George et al., 2011; Yang et al., 2014).

There were three stages of thermal degradation for the core as well. Due to thermal de-polymerization between of PVA-SA and GA, the small degradation step with a higher weight loss of about 10% was observed around 227.4–243.4 ℃, implying that the IPN structured core is not thermally stable above 227.4 ℃. (Kuila and Ray, 2014; Lu et al., 2015). The maximum thermal degradation temperatures for alginate and PVA were combined to one and shifted to

281.5 ℃ with WLR_{max} of 1.57 %/℃, while the pyrolysis of breakdown of polymer backbone occurred over the wide temperature range of 350.8-506.7 ℃ (Yang et al., 2014). Compared to degradation in the shells, the main decomposition of the cores at a much quicker rate was indicative of lower thermal resistance. This could be attributed to cross linking between -OH and $–CHO^-$ groups at core were weaker than egg box junctions between $–COO^-$ and Ca^{2+} at shell which required higher activation energy for thermal decomposition. Also, the char yield at 600 ℃ was around 20% for the core, but for the shell, 37.3% of the char residue was observed at 600 ℃. The high char yield of the shell was ascribed to the crosslinking of $–COO^-$ ions through Ca^{2+} ions with PVA dispersing in shell, forming SIPN structure by strong egg box junctions (Dragan, 2014). This phenomenon evidenced that the shell was compact and rigid, which is consistent with SEM and mechanical results.

After incorporating CNPs in the core, T_0 and T_{max} of PSG-CA-CNP cores were up to 15 ℃ lower than those of PSG-CA core (Table 4.2). This phenomenon could be explained by the presence of SO_4^{2-} groups that were created during acid hydrolysis of cellulose. These groups induced more degradation reactions in PVA and SA, thus accelerating the decomposition of these polymers (George et al., 2011; Uddin et al., 2011). Furthermore, T_0 values of PSG-CA-CNF I core and PSG-CA-CNC I core were 215.7 and 213.4 ℃, and T_{max} of PSG-CA-CNF I core was higher than that of PSG-CA-CNC I core for all the three stages, illustrating the thermal stability for PSG-CA-CNF cores was higher than PSG-CA-CNC cores. The increased number of free end groups of CNCs in PSG-CA-CNC cores resulted in their degradation at lower temperature. Also, compared to the PSG-CA-CNF I and PSG-CA-CNC I cores, the degradation of PSG-CA-CNF I/II core and PSG-CA-CNC I/II core were initiated at higher temperatures. The structure of cellulose I/II with part of anti-parallel chains achieved a stronger crystalline lattice

and more robust –OH group interactions, therefore, they required more energy to degrade. These results were consistent with our previous study (Yue et al., 2012a; Yue et al., 2015a).

With the addition of CNPs, CY values for PSG-CA-CNP cores were larger than those for PSG-CA core. Specifically, CY for PSG-CA-CNC cores was higher as compared to PSG-CA-CNF cores. It was attributed to higher concentration of sulfuric acid partial destruction of the amorphous region in making CNCs, resulting in a higher percentage of residual char at 600 ℃. In addition, CY values for the core of PSG-CA-CNF I/II and PSG-CA-CNC I/II were higher than those for the core of PSG-CA-CNF I and PSG-CA-CNC I, which was possibly ascribed to the higher thermal stability of cellulose I/II and their favorable interactions with polymer matrixes.

4.3.5 UV transmittance Spectra of Hydrogel

Because of their high water content (Table 4.3), hydrogels were translucent with a mean transmittance of ~47.29%. The transmittance of hydrogel decreased with incorporation of CNPs (Figure 4.7a) mainly because CNPs hindered the light passage through the hydrogels (Oun and Rhim, 2015). In addition, compared to PSG-CA-CNC I, the decrease in light transmittance of PSG-CA-CNF I over the range from 300nm to 800 nm indicated that as compared to CNC I, CNF I hindered more light passing through the hydrogels. This was because large-sized CNF I can promote the entanglement of polymeric chains and thus resulted in a more compact structure (Han et al., 2013a).

As shown in Figure 4.7a and b, for all the hydrogels and CNP suspensions, the transmittance was lower at wavelengths of 300-500 nm as the consequence of more light scattering when wavelengths were within the range of the particle (PVA and SA) diameters (Benhamou et al., 2014). At lower wavelengths (300-500 nm), the transmittance was in order of PSG-CA-CNC I/II> PSG-CA-CNC I> PSG-CA-CNF I/II> PSG-CA-CNF I, meaning that the

diameter followed the opposite order of CNC I/II< CNC I< CNF I/II< CNF I, which was consistent with the results in morphology section (Figure 4.2 and Table 4.1). The increasing rate of transmittance for PSG-CA was similar to that for PSG-CA-CNC I/II, indicating that the diameter of CNC I/II approached the diameter of PVA and SA polymer chains.

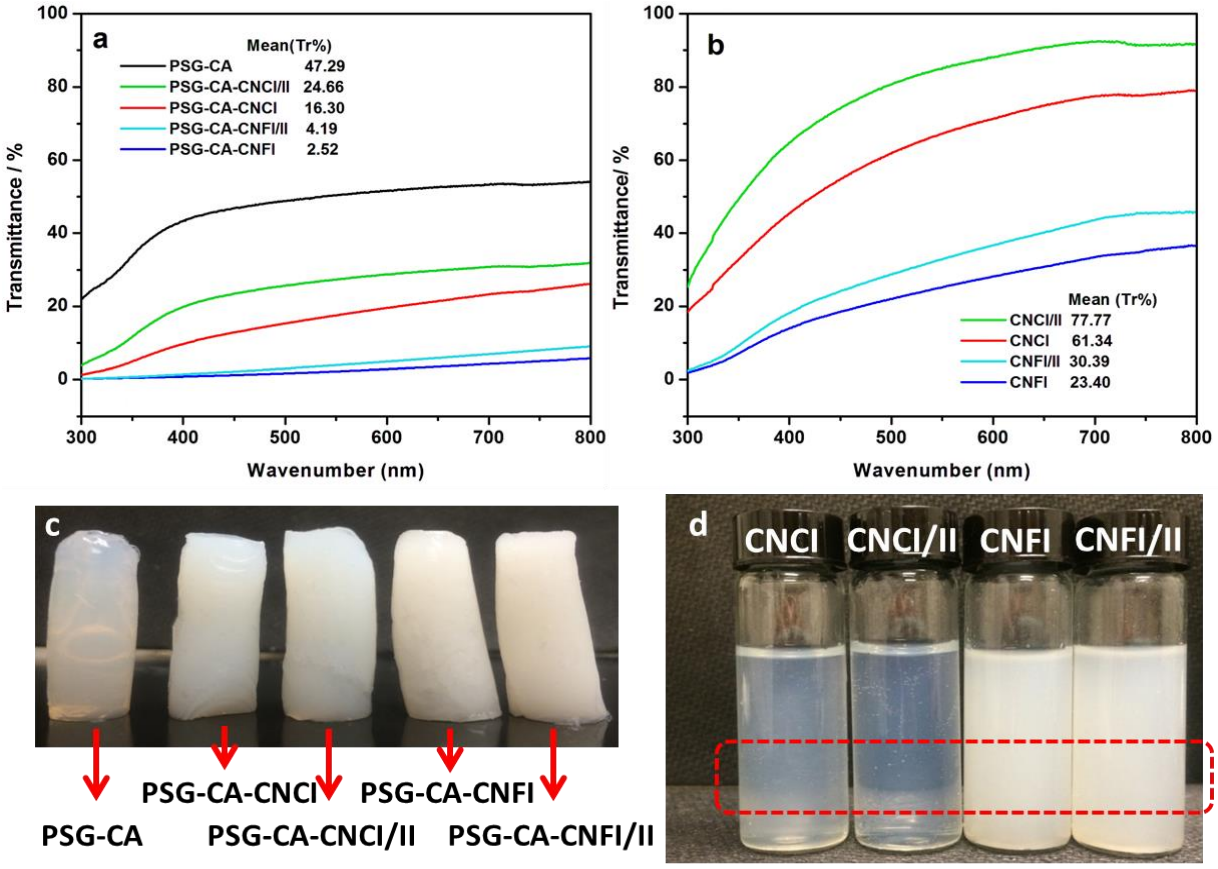

Figure 4.7 UV–Vis light transmittance spectra of (a) core-shell hydrogels and (b) 1.0 wt% CNPs at visible wavelength range of 300–800 nm; Photographs of (c) hydrogels without/with incorporating 1.0 wt% CNPs (diameter 10 mm) and (d) the dispersion states of CNPs at the 1.0 wt% concentration level.

Additionally, PSG-CA-CNC I exhibited a translucent color, whereas PSG-CA-CNF I was opalescent, further confirming that the color of hydrogel varied with the types of incorporating CNPs (Figure 4.7c). The transmittance followed the trend of PSG-CA> PSG-CA-CNC I/II> PSG-CA-CNC I> PSG-CA-CNF I/II> PSG-CA-CNF I, which was in accordance with the transparency trend of CNP suspensions (Figure 4.7b and d). In addition, all these hydrogels

manifested high stability and superior homogeneity, suggesting that CNPs were well-dispersed in the core and shell matrixes without any visible aggregation, further evidencing an excellent compatibility of cellulose fillers with the polymer matrix. The homogeneous dispersion state of CNPs was attributed to the SIPN structured shell, the IPN structured core and the CNPs all being hydrophilic, and the –OH groups in CNPs easily interacted with the –OH groups in both core and shell (El Miri et al., 2015), leading to a tangled, crosslinked and stable 3D network structure. The homogeneity of CNPs in the PSG system was significantly important for achieving the improved mechanical properties of the hydrogels.

4.3.6 Viscoelasticity of core

Because the core significantly decreased the brittleness and contributed to the mechanical strength of the hydrogel, viscoelasticity tests were carried out to study the reinforcement of the core. Before other rheological measurements, dynamic strain sweep was performed for the IPN core to define the LVR, in which G' was independent to the applied strain. The end of LVR was defined as the critical strain (ε_c) (Benhamou et al., 2014). When strain (ε) was out of LVR, G' was decreased, as a consequence of a transition from the quasi-solid state to a quasi-liquid state (Han et al., 2014). As shown in Figure 4.8a, the ε_c values for CNF I as well as PSG-CA-CNF I and PSG-CA cores were 3.9, 1.0, and 2.0%. In general, the shorter the LVR, the more rigid the sample (Han et al., 2014). The ε_c value of the PSG-CA-CNF I core was smaller than those of the CNF I suspension and the PSG-CA cores. Therefore, the shorter LVR of PSG-CA-CNF I core implied the stiffness of the network in PSG-CA-CNF I core. For all of the hydrogels, when ε was less than 1.0%, G' was basically independent of the applied ε. A strain level of 1.0% was then selected in the subsequent tests to ensure that the deformation of each sample was within the LVR. At the 1.0% strain level, the core with 1.0% CNPs (PSG-CA-CNP cores) exhibited

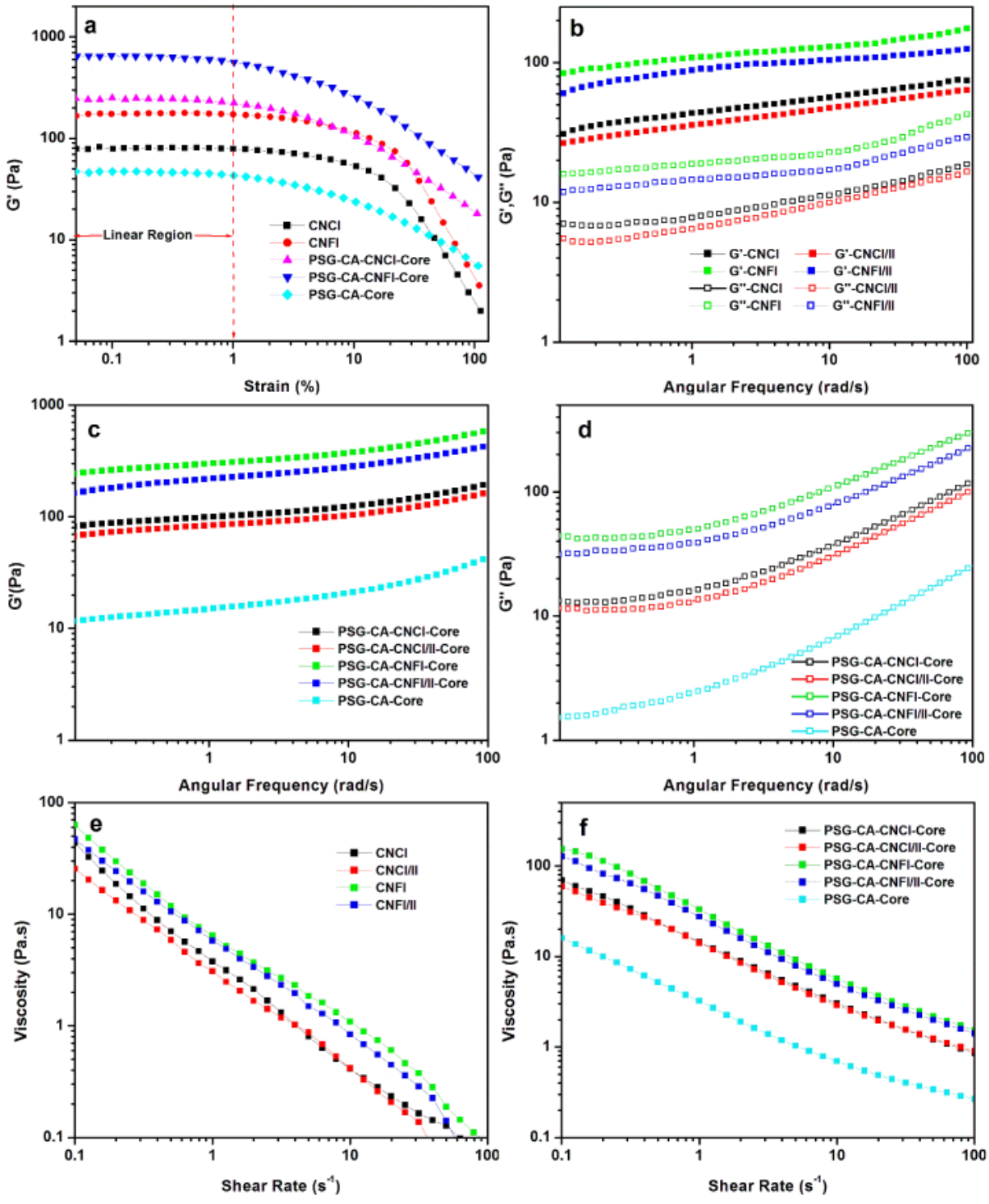

Figure 4.8 Rheological performance of PSG-CA-CNP core complexes at 25 ℃: (a) strain dependence of G' for PSG-CA-CNP cores and CNP suspensions, measured at ω = 1.0 Hz; (b) frequency dependence of G' and G" for 1.0 wt% CNPs; (c) and (d) frequency dependence of G' and G" for PSG-CA-CNP cores; (e) shear rate dependence of viscosity for CNP suspensions, and (f) PSG-CA-CNP cores.

significantly higher G' values compared to these of the 1.0 wt% CNPs and PSG-CA core. Because of the excellent mechanical strength and toughness of CNPs, G' for the CNP dispersions was larger than that for neat IPN at the 1.0% strain level.

Dispersions of CNPs were subjected to dynamic frequency sweep to study its viscoelastic behavior. Figure 4.8b shows G' and G" as a function of ω for CNPs at loading levels of 1.0 wt%. All of the CNP suspensions had the higher G' values than G" values over the frequency range of 1-100 rad/s. This observation suggested that the reversible potential energy (elastic properties) were dominant as compared to irreversible consumed energy (viscous characteristics) (Benhamou et al., 2014). With increased ω, G' and G" implying that the rigidity and viscosity of CNPs (Figure 4.8b and e) was greater at higher frequency. The phenomenon was caused by the equilibrium state of CNPs being broken at high frequencies and an ordered network structure being reestablished by the rearrangement of CNPs (Han et al., 2014).

G' and G" as a function of ω for PSG-CA-CNP cores are shown in Figure 4.8c and d. The G' value from the frequency sweep agreed well with the observations from the strain sweep behavior of the PSG-CA-CNP and PSG-CA cores (Figure 4.8a). For all the core systems, the elastic character was a dominant factor, inferred from the observation that G' was about one order of magnitude larger than G" over the frequency range from 1 to 100 rad/s. In the low frequency region, G' and G" were relatively independent of frequency. As ω increased, G" gradually approached G', which was a sign of deformation and re-formation of hydrogen bonding and interactions between PVA and SA (Wang and Chen, 2011). Because PVA is a flexible polymer and SA is relatively rigid (Cho et al., 2009), it was considered that SA with its stiff nature of SA played a primary role at low rotational frequency, whereas flexible PVA chains dominated the modulus at higher rates. For the PSG-CA core, G' and G" were 45 and 26 Pa,

respectively. These relatively high values probably occurred because the fact that -CHO groups in GA were able to crosslink with the –OH groups in SA and PVA to form an IPN structure. After incorporation CNPs, the increase in G' and G" values suggested the presence of a greater number of interactions in PSG-CA-CNP cores than those in PSG-CA core. This favorable mechanical performance was attributed to the homogeneous distribution of CNPs in the PVA-SA matrix (Figure 4.7a and c) and crosslinked with the PVA/SA matrix through hydrogen bonds, resulting in additional interactions between CNPs and PVA-SA chains.

The elasticity of structure in hydrogel is in the order of PSG-CA-CNF I core> PSG-CA-CNF I/II core> PSG-CA-CNC I core>PSG-CA-CNC I/II core> PSG-CA core. For example, with the addition of CNF I, the values of the elastic modulus reached 600 Pa and the viscous modulus achieved 320 Pa for the PSG-CA-CNF I core; whereas the G’ and G” for PSG-CA-CNC I core were only 201 and 127 Pa. This phenomenon suggested that the viscoelastic behaviors for PSG-CA core increased 13 and 4.5-fold with addition of CNF I and CNC I, respectively. According to TEM data, the average lengths for CNF I and CNC I were 485±168 nm and 154±72 nm, respectively, therefore, the CNP’s dimension was the most important influence on the mechanical strength of the hydrogel (Benhamou et al., 2014). Compared with CNC I, CNF I possessed higher fiber length and larger aspect ratio, which contributed to the entanglement of CNPs in PSG-CA cores and the construction of 3D structured IPN (Liu et al., 2011), resulting in the enhancement of mechanical strength, increase of density, and higher thermal stability for the hydrogels. In addition, because the cellulose I/II with smaller particle lengths possessed small number of -OH interactions, they were less tangled with PVA and SA chains. As a result, the toughness of cellulose I/II incorporated core was lower than cellulose I integrated core for both CNC and CNF. The small crosslinking capacity and rigidity of CNC I/II and CNF I/II also

resulted in a lower density of PSG-CA-CNC I/II and PSG-CA-CNF I/II cores. Therefore, the density for hydrogel followed the trend of PSG-CA-CNF I core> PSG-CA-CNF I/II core> PSG-CA-CNC I core>PSG-CA-CNC I/II core> PSG-CA core (Table 4.3).

Figures 4.8e and f display the steady shear η of the CNP suspensions as well as PSG-CA-CNP cores as a function of γ. With the increase of γ, η values of CNP suspensions and PSG-CA-CNP core complexes decreased. A possible reason for this pronounced shear-thinning behavior was the inter/intra molecular interaction in CNPs and the entanglement between PVA-SA and CNPs were disrupted at a rotational rate faster than their rate of reformation (El Miri et al., 2015). With incorporation of CNPs, the η for all of the PSA-CA-CNP cores were significantly increased. The η values were in the order of PSG-CA-CNF I core> PSG-CNF I/II core> PSG-CNC I core>PSG-CNC I/II core> PSG-CA core, indicating that the dimension of CNPs influenced viscous response. In addition, the η values for PSG-CA-CNP cores were higher than those for CNPs, especially at higher γ. It appeared that once the IPN network was formed, the covalent associations are seldom broken even at a high γ (Dragan, 2014), further confirming a dense and stable structure of the PSG-CA-CNP cores. Therefore, the core, with high modulus and viscosity along with a rigid shell allowed the hydrogels to achieve a favorable performance and build a solid foundation for future applications.

4.3.7 Compression property of the hydrogels

The uniaxial compression measurements were performed to investigate mechanical properties of hydrogel with a ductile core and a stiff shell. The stress–strain curves of core shell structured hydrogels before shell rupture are presented in Figure 4.9a. To compare the compressive strength of the hydrogel with different types of CNPs, the stresses at the 20%, 35%, and 45% strain were evaluated, and the values are summarized in Table 4.3.

In the first stage, the hydrogels exhibited a typical linear stress-strain behavior. That indicated that the core and shell changed from a relaxed state to a stressed state and the hydrogels deformed elastically to store energy for resisting applied stresses (Zhao et al., 2015) (Figure 4.9a and c). In the subsequent stage, the stress slightly deviated from linear response, and the energy-dissipation happened inside the network to resist the compression stress (Gyarmati et al., 2015; Zhao et al., 2015). In the final stage, a sharp increase in stress with an extremely large deformation was presented, suggesting that the network interactions for shell almost reached its full extent. The ultimate compressive strength for hydrogel was reached at a strain around 47%. After shell rupture, the core might still be able to bear some compression stresses.

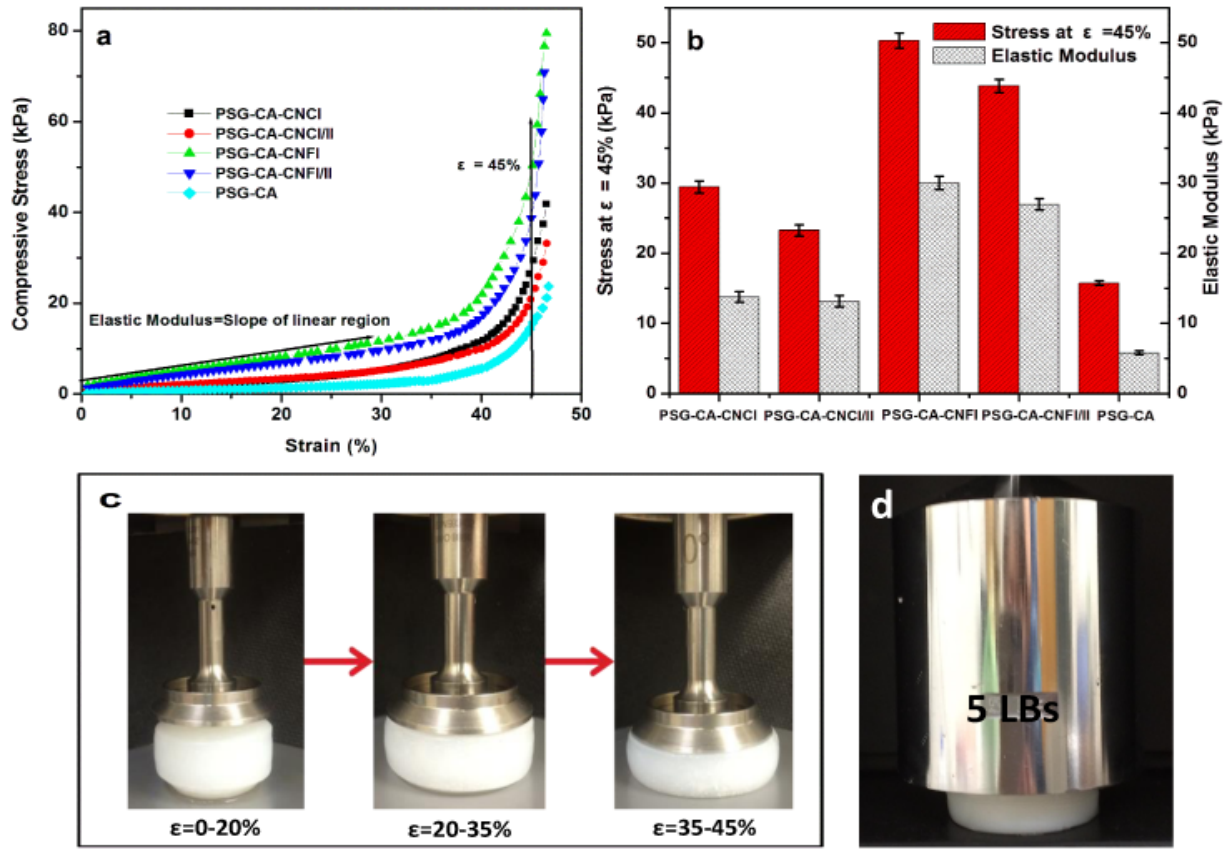

Figure 4.9 Compression property of hydrogels: (a) compression stress–strain curves of hydrogels; and (b) a comparison of compressive stress at the 45% of strain and the compressive elastic modulus Eε; (c) the compression process; (d) the PSG-CA-CNF I undamaged under a static loading of 5.0 lbs.

Table 4.3 Physical and compression properties of hydrogels

Hydrogels	Water Content Wc (wt %)	Density (g/cm^3)	Stress at ε=20% (kPa)	Stress at ε=35% (kPa)	Stress at ε=45% (kPa)	Elastic modulus (kPa)
PSG-CA-CNC I	93.3 ± 1.5	1.14 ± 0.07	3.21 ± 0.07	7.68 ± 0.20	29.46 ± 0.87	6.87 ± 0.74
PSG-CA-CNC I/II	93.5 ± 1.6	1.12 ± 0.06	3.43 ± 0.07	7.27 ± 0.22	23.27 ± 0.82	6.58 ± 0.79
PSG-CA-CNF I	92.3 ± 2.0	1.21 ± 0.13	8.33 ± 0.10	14.73 ± 0.39	50.51 ± 1.09	15.02 ± 0.93
PSG-CA-CNF I/II	92.7 ± 1.3	1.18 ± 0.11	7.01 ± 0.11	11.89 ± 0.35	43.86 ± 0.95	13.48 ± 0.82
PSG-CA	94.2 ± 2.2	1.12 ± 0.07	1.43 ±0.05	3.26 ± 0.13	15.67 ± 0.33	2.91 ± 0.27

The compressive stress of PSG-CA at the 45% strain level was 15.67 ± 0.33 kPa (Figure 4.9b). Compared with other virgin hydrogels with the compression stress (at the strain level of 80%) in the range of 3-5 kPa (Sun et al., 2015), the observed high compressive load revealed the stiff nature of the current core-shell structure hydrogel. This was attributed to the existence of SA in both the core and the shell and all of the polymers have many –OH groups. When CNPs were incorporated into the core-shell structured hydrogels, the compressive stress of PSG-CA-CNC I, PSG-CA-CNC I/II, PSG-CA-CNF I and PSG-CA-CNF I/II at the 45% strain level were 1.9, 1.5, 3.2 and 2.8 times higher than that of the hydrogel without CNPs, indicating that the addition of CNPs significantly increased the compressive-resistance for PSG-CA hydrogel. It was reported that the hydrogel mechanical properties were highly related to the distribution of CNPs in IPN and cross-linking degree with polymer matrix (Liu et al., 2011; Hou et al., 2015). Because CNPs were homogenously dispersed in polymer matrix and interacted with core and shell through –OH (SEM, UV and FTIR results), they could sustain a portion of the compressive load, and contribute to a promising mechanical strength for PSG-CA-CNP hydrogels.

The compression strength for these hydrogels were in order of PSG-CA-CNF I > PSG-CA-CNF I/II > PSG-CA-CNC I >PSG-CA-CNC I/II > PSG-CA. Before the shell raptured, PSG-

CA-CNC I, PSG-CA-CNC I/II, PSG-CA-CNF I, PSG-CA-CNF I/II and PSG-CA could sustain a pressure of 41.9, 33.2, 79.5, 70.8 and 23.7 kPa, respectively, suggesting that characteristics of CNPs played dominant roles in improving the mechanical properties of hydrogels (Hou et al., 2015). Compared to other CNPs with average length ranging from 98 to 367 nm, CNF I, which had an average length of 485 nm (Table 4.1) led to the increasingly physical and chemical cross-linking with core and shell (Han et al., 2013a). As shown in the insert of Figure 4.9d, the PSG-CA-CNF I could sustain a 5.0 lbs weight, exhibiting an extremely high stress.

Clearly, the hydrogel without CNPs (PSG-CA) had a low elastic modulus (Eε) (Figure 4.9b and Table 4.3), (determined from the slope of the linear portion of the stress–strain curve), indicative of a fairly soft hydrogel with a relatively weak network (Liang et al., 2008; Han et al., 2013a; Sun et al., 2015). The stress-strain curves for PSG-CA-CNPs had a greater slope than that of the PSG-CA, and the initial Eε of PSG-CA-CNC I, PSG-CA-CNC I/II, PSG-CA-CNF I and PSG-CA-CNF I/II were 2.4, 2.3, 5.2 and 4.6 times higher than that of PSG-CA, demonstrating that PSG-CA-CNP can resist much higher pressure than PSG-CA.

4.3.8 Adsorption and desorption performances

The adsorption of MB on core-shell structured hydrogels at constant temperature (25℃) was studied and the experimental results are shown in Figure 4.10. In Figure 4.10a, at low initial concentration (≤ 5mg/L), the number of adsorbed molecules increased quickly due to abundant free adsorption sites on the hydrogel pore surfaces. The concentration differential in MB solution and hydrogels also provided a strong driving force (Zheng et al., 2014). As the concentration increased, more active adsorption sites of hydrogels were occupied and the adsorbed MB on hydrogels was increased. Thereafter, the adsorption rate decreased until reaching the maximum adsorption capacity. It was reported that various factors influenced MB adsorption, such as pore

volume in sorbent surfaces, sorbent surface chemistries, and the interaction between MB and sorbent (Ghorai et al., 2013). Because of the porous nature, the absorbent nature of SA (active sites of -COOH), and chemical stability of IPN and SIPN structure (Aftab et al., 2014), hydrogel could easily adsorb MB, which was deposited on the highly crosslinked polymer matrix (Bhattacharyya and Ray, 2015). In addition, the PSG-CA-CNPs absorbed a greater amount of MB than neat PSG-CA. A possible reason was that the active sites of –OH and -SO_4 groups on the surfaces of CNPs led to more free energy for adsorbing MB, resulting in a synergistic behavior of CNPs and PSG-CA on adsorption. It should be noted that there were no clear differences in adsorption capacities through incorporating different types of CNPs, therefore, only two plots are shown in Figure10.

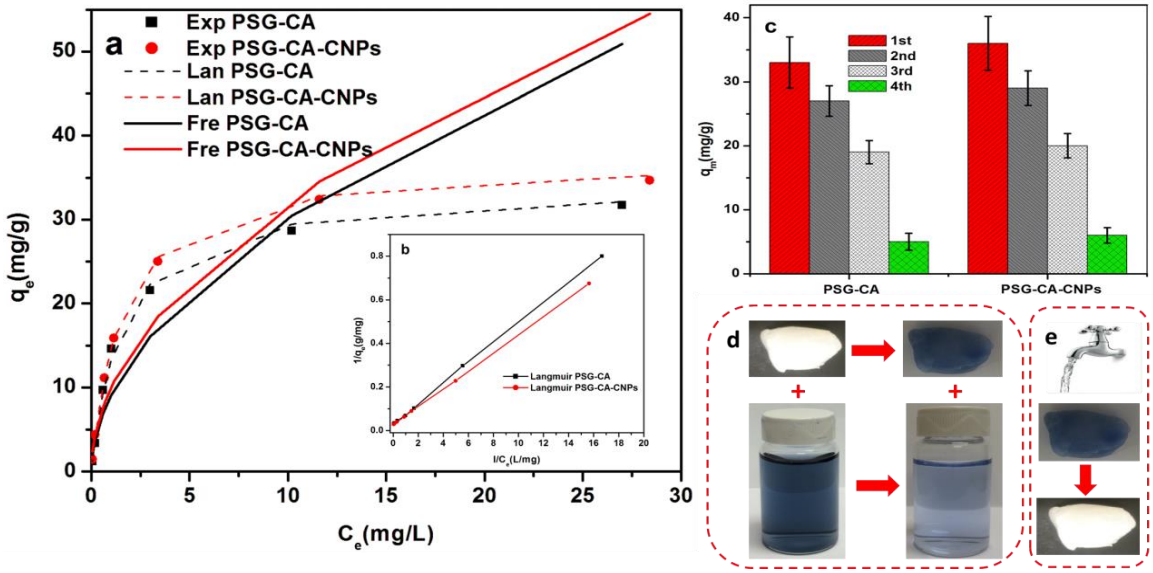

Figure 4.10 The adsorption and desorption behavior of hydrogels: (a) experimental data of MB adsorption on hydrogels, and the predicted Langmuir and Freundlich isotherms; (b) Langmuir isotherms determined from the linear plot of $1/q_e$ versus $1/c_e$; (c) the hydrogels maximum adsorption capacity for the four cycles of the adsorption–desorption process; (d) adsorption and (e) desorption behavior of MB on hydrogels

Langmuir and Freundlich isotherm models (Equations [4.4] and [4.5], respectively) were applied to the MB adsorption.

$$q_e = \frac{q_m K_L C_e}{1+K_L C_e} \qquad [4.4]$$

Where q_m is the Langmuir constant related to maximum adsorption capacity (mg/g), and K_L is the Langmuir adsorption equilibrium coefficient reflecting affinity of adsorbent toward adsorbate (L/mg).

$$q_e = K_F C_e^{1/n} \qquad [4.5]$$

Where K_F is the Freundlich adsorption equilibrium coefficient (L/mg), and 1/n is the adsorption intensity, respectively.

These two models can be described in a linear form as Equations [4.6] and [4.7]. The experimental data satisfying the linearity of the isotherm indicated the adsorption process followed the isotherm. Then the values of isotherm parameters (K_L and qm for Langmuir, K_F and 1/n for Freundlich) could be calculated using slope and intercept. The obtained isotherm parameters are listed in Table 4.4.

$$\frac{1}{q_e} = \left(\frac{1}{K_L q_m}\right)\frac{1}{C_e} + \frac{1}{q_m} \qquad [4.6]$$

$$log q_e = \frac{1}{n} log C_e + log K_F \qquad [4.7]$$

Table 4.4 Comparison of the parameters predicted from Langmuir and Freundlich models with experimental data obtained from hydrogel adsorption of methyl blue

Sample	q_m(exp) (mg/g)	Predicted parameter					
		Langmuir			Freundlich		
		q_m (mg/g)	K_L (L/mg)	R^2	K_F (mg/g)	1/n	R^2
PSG-CA	33.6	34.0	0.650	0.995	9.00	0.525	0.802
PSG-CA-CNPs	36.3	37.2	0.634	0.996	9.91	0.510	0.813

Langmuir isotherm models assume a monolayer adsorption, that adsorbent surface is homogeneous, and that all active sites have the same affinity to adsorbate (Bhattacharyya and Ray, 2014; Chung et al., 2015). On the other hand, the Freundlich isotherm model applies to multilayer adsorption on heterogeneous surfaces with different adsorption energies.(Bhattacharyya and Ray, 2015) As shown in Figure 4.10b and Table 4.4, the linear fitting of Langmuir isotherm model and the high value of R^2 (≥ 0.99) indicated experimental data having a favorable mathematical fitting to the Langmuir isotherm, implying that MB adsorbed on hydrogels was monolayer adsorption and the adsorbed MB layer was one molecule depth in thickness (Ghorai et al., 2013; Chung et al., 2015). The calculated maximum adsorption amount of MB (q_m) on PSG-CA and PSG-CA-CNPs was 34.0 and 37.2 mg/g, which were very close to the experimental values (33.6 for PSG-CA and 36.3 for PSG-CA-CNPs).

The parameter RL was used to evaluate the adsorption favorability in the Langmuir isotherm. The Langmuir process is unfavorable when RL > 1, favorable when 0 < RL <1, linear when RL = 1 and irreversible when RL = 0 (Ghorai et al., 2013; Bhattacharyya and Ray, 2015).

$$R_L = \frac{1}{1+C_0 K_L} \qquad [4.8]$$

In this study, the K_L values were about 0.65 and the R_L values were in the range of 0-1, which signify a promising adsorption ability of the hydrogels for MB (Ghorai et al., 2013; Bhattacharyya and Ray, 2014).

As shown in Figure 4.10c, although there were slight reductions in the adsorption capacities, the hydrogel exhibited a satisfactory adsorption capacity after two to three cycles of the adsorption–desorption process, proving that a hydrogel that offers strong electrostatic interaction energies could be employed multiple cycles (Bhattacharyya and Ray, 2014). Figure 4.10d shows that after the adsorption process, the MB solution was much lighter in color, further

demonstrating that the hydrogel adsorbed most of the MB from aqueous solution. Figure 4.10e shows that the adsorbed hydrogel, which was thoroughly rinsed with distilled water for 10 minutes, was white without any trace of blue. This high desorption performance is important for achieving multiple adsorption–desorption cycles by the hydrogels.

4.4 CONCLUSIONS

Core-shell structured hydrogels consisting of a rigid SIPN shell and a flexible IPN core were prepared through chelation and covalent bonding of PVA-SA with Ca^{2+} and GA, respectively. Four kinds of CNPs (differences in particle size, aspect ratio and crystal structure) were incorporated into the hydrogel system. These CNPs were well dispersed in the hydrogels and reinforced the hydrogels via inter/intra-molecular hydrogen bonds. The hydrogel had micro-porous shells and macro-porous cores. The neat PSG-CA hydrogels with a water content of 94.2% provided an elastic modulus of 2.91 kPa and a maximum MB adsorption capacity of 33.6 mg/g. Although incorporation CNPs into the hydrogels decreased the thermal stabilities, dynamic oscillation and compression measurements showed that the CNPs dramatically elevated the viscoelasticity of the core and the compressive strength of the hydrogels. The modulus of the core and mechanical property of the hydrogels were in the order of PSG-CA-CNF I > PSG-CA-CNF I/II > PSG-CA-CNC I > PSG-CA-CNC I/II > PSG-CA, while their transparency was sequenced in a reverse order. PSG-CA-CNF I exhibited the strongest stiffness and its storage modulus and compressive strength were 13 and 3.2 times higher than that of neat PSG-CA. The incorporation of CNPs into core-shell structured hydrogels also increased the MB adsorption capacity by 10%. The MB adsorbed on hydrogels in monolayers and multiple adsorption-desorption cycles could be applied to the hydrogels. The proposed hydrogel with good ductility core and high strength shell has many excellent properties, such as readily processed, eco-

friendliness, favorable mechanical strength and promising adsorption capacity, the hydrogels could be used in treating many water pollutants (dye, toxic metals and agricultural residues removal). Moreover, the properties of the hydrogels could be regulated through selecting different CNPs and the potential applications could be extended to the areas in biosensors (Cushing and Anseth, 2007; Seliktar, 2012; Zhang et al., 2015).

4.5 REFERENCES

Aftab, K., Akhtar, K., Jabbar, A., 2014. Batch and column study for Pb-II remediation from industrial effluents using glutaraldehyde–alginate–fungi biocomposites. Ecological Engineering 73, 319-325.

Bekin, S., Sarmad, S., Gürkan, K., Keçeli, G., Gürdağ, G., 2014. Synthesis, characterization and bending behavior of electroresponsive sodium alginate/poly(acrylic acid) interpenetrating network films under an electric field stimulus. Sensors and Actuators B: Chemical 202, 878-892.

Benhamou, K., Dufresne, A., Magnin, A., Mortha, G., Kaddami, H., 2014. Control of size and viscoelastic properties of nanofibrillated cellulose from palm tree by varying the TEMPO-mediated oxidation time. Carbohydrate Polymers 99, 74-83.

Berrebi, M., Fabre-Francke, I., Lavédrine, B., Fichet, O., 2015. Development of organic glass using Interpenetrating Polymer Networks with enhanced resistance towards scratches and solvents. European Polymer Journal 63, 132-140.

Bhattacharyya, R., Ray, S.K., 2014. Enhanced adsorption of synthetic dyes from aqueous solution by a semi-interpenetrating network hydrogel based on starch. Journal of Industrial and Engineering Chemistry 20, 3714-3725.

Bhattacharyya, R., Ray, S.K., 2015. Adsorption of industrial dyes by semi-IPN hydrogels of Acrylic copolymers and sodium alginate. Journal of Industrial and Engineering Chemistry 22, 92-102.

Bidarra, S.J., Barrias, C.C., Granja, P.L., 2014. Injectable alginate hydrogels for cell delivery in tissue engineering. Acta Biomaterialia 10, 1646-1662.

Bras, J., Viet, D., Bruzzese, C., Dufresne, A., 2011. Correlation between stiffness of sheets prepared from cellulose whiskers and nanoparticles dimensions. Carbohydrate Polymers 84, 211-215.

Cho, S.H., Lim, S.M., Han, D.K., Yuk, S.H., Lm, G.I., Lee, J.H., 2009. Time-Dependent Alginate/Polyvinyl Alcohol Hydrogels as Injectable Cell Carriers. Journal of Biomaterials Science -- Polymer Edition 20, 863-876.

Chung, H.-K., Kim, W.-H., Park, J., Cho, J., Jeong, T.-Y., Park, P.-K., 2015. Application of Langmuir and Freundlich isotherms to predict adsorbate removal efficiency or required amount of adsorbent. Journal of Industrial and Engineering Chemistry 28, 241-246.

Cushing, M.C., Anseth, K.S., 2007. Hydrogel Cell Cultures. Science 316, 1133-1134.

Dash, R., Foston, M., Ragauskas, A.J., 2013. Improving the mechanical and thermal properties of gelatin hydrogels cross-linked by cellulose nanowhiskers. Carbohydrate Polymers 91, 638-645.

Dragan, E.S., 2014. Design and applications of interpenetrating polymer network hydrogels. A review. Chemical Engineering Journal 243, 572-590.

El Miri, N., Abdelouandi, K., Barakat, A., Zahouily, M., Fihri, A., Solhy, A., El Achaby, M., 2015. Bio-nanocomposite films reinforced with cellulose nanocrystals: Rheology of film-forming solutions, transparency, water vapor barrier and tensile properties of films. Carbohydrate Polymers 129, 156-167.

George, J., Ramana, K.V., Bawa, A.S., Siddaramaiah, 2011. Bacterial cellulose nanocrystals exhibiting high thermal stability and their polymer nanocomposites. International Journal of Biological Macromolecules 48, 50-57.

Ghorai, S., Sarkar, A.K., Panda, A.B., Pal, S., 2013. Effective removal of Congo red dye from aqueous solution using modified xanthan gum/silica hybrid nanocomposite as adsorbent. Bioresource Technology 144, 485-491.

Gyarmati, B., Meszar, E.Z., Kiss, L., Deli, M.A., Laszlo, K., Szilagyi, A., 2015. Supermacroporous chemically cross-linked poly(aspartic acid) hydrogels. Acta Biomaterialia 22, 32-38.

Han, J., Lei, T., Wu, Q., 2013a. Facile preparation of mouldable polyvinyl alcohol-borax hydrogels reinforced by well-dispersed cellulose nanoparticles: physical, viscoelastic and mechanical properties. Cellulose 20, 2947-2958.

Han, J., Lei, T., Wu, Q., 2014. High-water-content mouldable polyvinyl alcohol-borax hydrogels reinforced by well-dispersed cellulose nanoparticles: Dynamic rheological properties and hydrogel formation mechanism. Carbohydrate Polymers 102, 306-316.

Han, J., Zhou, C., Wu, Y., Liu, F., Wu, Q., 2013b. Self-Assembling Behavior of Cellulose Nanoparticles during Freeze-Drying: Effect of Suspension Concentration, Particle Size, Crystal Structure, and Surface Charge. Biomacromolecules 14, 1529-1540.

Hou, R.X., Nie, L., Du, G.L., Xiong, X.P., Fu, J., 2015. Natural polysaccharides promote chondrocyte adhesion and proliferation on magnetic nanoparticle/PVA composite hydrogels. Colloids and Surfaces B-Biointerfaces 132, 146-154.

Jao, W.C., Chen, H.C., Lin, C.H., Yang, M.C., 2009. The controlled release behavior and pH- and thermo-sensitivity of alginate/poly(vinyl alcohol) blended hydrogels. Polymers for Advanced Technologies 20, 680-688.

Kahya, S., Solak, E.K., Sanli, O., 2010. Sodium alginate/poly(vinyl alcohol) alloy membranes for the pervaporation, vapour permeation and vapour permeation with temperature difference separation of dimethylformamide/water mixtures: A comparative study. Vacuum 84, 1092-1102.

Kan, B., Lin, B., Zhao, K., Zhang, X., Feng, L., Wei, J., Fan, Y., 2014. Imprinting of bovine serum albumin in a nonwoven polypropylene membrane supported polyacrylamide/calcium alginate interpenetrating polymer network hydrogel. RSC Advances 4, 55846-55852.

Kim, J.H., Jegal, J., Lee, K.H., Lee, Y., 2003. Enantioselective permeation of alpha-amino acid optical isomers through crosslinked sodium alginate membranes. Journal of Applied Polymer Science 89, 3046-3051.

Kuila, S.B., Ray, S.K., 2014. Dehydration of dioxane by pervaporation using filled blend membranes of polyvinyl alcohol and sodium alginate. Carbohydrate Polymers 101, 1154-1165.

Lee, K.Y., Mooney, D.J., 2012. Alginate: Properties and biomedical applications. Progress in Polymer Science 37, 106-126.

Liang, S., Wu, J., Tian, H., Zhang, L., Xu, J., 2008. High-Strength Cellulose/Poly(ethylene glycol) Gels. ChemSusChem 1, 558-563.

Liu, D., Chen, X., Yue, Y., Chen, M., Wu, Q., 2011. Structure and rheology of nanocrystalline cellulose. Carbohydrate Polymers 84, 316-322.

Lu, T., Xiang, T., Huang, X.-L., Li, C., Zhao, W.-F., Zhang, Q., Zhao, C.-S., 2015. Post-crosslinking towards stimuli-responsive sodium alginate beads for the removal of dye and heavy metals. Carbohydrate Polymers 133, 587-595.

Mounika, M., Ravindra, K., 2015. Characterization of Nanocomposites Reinforced with Cellulose Whiskers: A Review. Materials Today: Proceedings 2, 3610-3618.

Oun, A.A., Rhim, J.-W., 2015. Effect of post-treatments and concentration of cotton linter cellulose nanocrystals on the properties of agar-based nanocomposite films. Carbohydrate Polymers134, 20-29.

Papageorgiou, S.K., Katsaros, F.K., Favvas, E.P., Romanos, G.E., Athanasekou, C.P., Beltsios, K.G., Tzialla, O.I., Falaras, P., 2012. Alginate fibers as photocatalyst immobilizing agents applied in hybrid photocatalytic/ultrafiltration water treatment processes. Water Research 46, 1858-1872.

Perez, R.A., Kim, J.-H., Buitrago, J.O., Wall, I.B., Kim, H.-W., 2015. Novel therapeutic core–shell hydrogel scaffolds with sequential delivery of cobalt and bone morphogenetic protein-2 for synergistic bone regeneration. Acta Biomaterialia 23, 295-308.

Sajjan, A.M., Kumar, B.K.J., Kittur, A.A., Kariduraganavar, M.Y., 2013. Novel approach for the development of pervaporation membranes using sodium alginate and chitosan-wrapped multiwalled carbon nanotubes for the dehydration of isopropanol. Journal of Membrane Science 425, 77-88.

Samanta, H.S., Ray, S.K., 2014. Synthesis, characterization, swelling and drug release behavior of semi-interpenetrating network hydrogels of sodium alginate and polyacrylamide. Carbohydrate Polymers 99, 666-678.

Seliktar, D., 2012. Designing Cell-Compatible Hydrogels for Biomedical Applications. Science 336, 1124-1128.

Shin, M.K., Spinks, G.M., Shin, S.R., Kim, S.I., Kim, S.J., 2009. Nanocomposite Hydrogel with High Toughness for Bioactuators. Advanced Materials 21, 1712-1715.

Sun, F., Lin, M., Dong, Z., Zhang, J., Wang, C., Wang, S., Song, F., 2015. Nanosilica-induced high mechanical strength of nanocomposite hydrogel for killing fluids. Journal of Colloid and Interface Science 458, 45-52.

Sun, J.Y., Zhao, X., Illeperuma, W.R.K., Chaudhuri, O., Oh, K.H., Mooney, D.J., Vlassak, J.J., Suo, Z., 2012. Highly stretchable and tough hydrogels. Nature 489, 133-136.

Thakur, V.K., Thakur, M.K., 2014. Processing and characterization of natural cellulose fibers/thermoset polymer composites. Carbohydrate Polymers 109, 102-117.

Thankam, F.G., Muthu, J., Sankar, V., Gopal, R.K., 2013. Growth and survival of cells in biosynthetic poly vinyl alcohol-alginate IPN hydrogels for cardiac applications. Colloids and Surfaces B-Biointerfaces 107, 137-145.

Uddin, A.J., Araki, J., Gotoh, Y., 2011. Characterization of the poly(vinyl alcohol)/cellulose whisker gel spun fibers. Composites Part A: Applied Science and Manufacturing 42, 741-747.

Ummartyotin, S., Manuspiya, H., 2015. A critical review on cellulose: From fundamental to an approach on sensor technology. Renewable and Sustainable Energy Reviews 41, 402-412.

Wang, Y., Chen, L., 2011. Impacts of nanowhisker on formation kinetics and properties of all-cellulose composite gels. Carbohydrate Polymers 83, 1937-1946.

Yang, J., Han, C.-R., Duan, J.-F., Xu, F., Sun, R.-C., 2013. Mechanical and Viscoelastic Properties of Cellulose Nanocrystals Reinforced Poly(ethylene glycol) Nanocomposite Hydrogels. ACS Applied Materials and Interfaces 5, 3199-3207.

Yang, J.M., Wang, N.C., Chiu, H.C., 2014. Preparation and characterization of poly(vinyl alcohol)/sodium alginate blended membrane for alkaline solid polymer electrolytes membrane. Journal of Membrane Science 457, 139-148.

Yeom, C.K., Lee, K.H., 1996. Pervaporation separation of water-acetic acid mixtures through poly(vinyl alcohol) membranes crosslinked with glutaraldehyde. Journal of Membrane Science 109, 257-265.

Yue, Y., Han, J., Han, G., Aita, G.M., Wu, Q., 2015a. Cellulose fibers isolated from energycane bagasse using alkaline and sodium chlorite treatments: Structural, chemical and thermal properties. Industrial Crops and Products 76, 355-363.

Yue, Y., Han, J., Han, G., Zhang, Q., French, A.D., Wu, Q., 2015b. Characterization of cellulose I/II hybrid fibers isolated from energycane bagasse during the delignification process: Morphology, crystallinity and percentage estimation. Carbohydrate Polymers 133, 438-447.

Yue, Y., Zhou, C., French, A.D., Xia, G., Han, G., Wang, Q., Wu, Q., 2012. Comparative properties of cellulose nano-crystals from native and mercerized cotton fibers. Cellulose 19, 1173-1187.

Zhang, Y., Liu, J., Huang, L., Wang, Z., Wang, L., 2015. Design and performance of a sericin-alginate interpenetrating network hydrogel for cell and drug delivery. Scientific Reports 5, 12374.

Zhao, W., Shi, Z., Chen, X., Yang, G., Lenardi, C., Liu, C., 2015. Microstructural and mechanical characteristics of PHEMA-based nanofibre-reinforced hydrogel under compression. Composites Part B-Engineering 76, 292-299.

Zheng, Y., Zhu, Y., Wang, A., 2014. Highly efficient and selective adsorption of malachite green onto granular composite hydrogel. Chemical Engineering Journal 257, 66-73.

CHAPTER 5 OVERALL CONCLUSIONS

In this study, cellulose fibers were extracted from energycane bagasse using a $NaOH/NaClO_2$ treatment and fundamental research was conducted to compare the non-cellulosic components, yield, crystallinity, and thermal stability of isolated ligno-cellulose fibers under different treatment conditions. In addition, the morphology, crystallinity, percentage and functional groups of the cellulose I/II hybrid fibers obtained during the delignification process were characterized. Finally, core-shell structured hydrogels consisting of a rigid SIPN shell and a flexible IPN core were prepared. The isolated nanofiber was used as fillers to reinforce core-shell structured hydrogels and the effects of the CNPs length, aspect ratio and crystal structure on the characteristic of the hydrogel was studied. The conclusions of this study are as follows:

Cellulose fibers were successfully isolated from energycane bagasse by using a combined NaOH and $NaClO_2$ treatment. After the delignification process, most lignin and hemicellulose were removed with a 27.4wt% yield of cellulose fibers, and the mean diameter of cellulose fibers decreased from 137 ± 46 to $12 \pm 5 \mu m$. The severe treatment conditions (concentration, treatment time) led to the decrease of lignocellulose yield. The crystallinity of cellulose fibers first decreased and then increased by NaOH treatments, and the crystallinity decreased through further $NaClO_2$ treatment. The raw bagasse samples showed three-step pyrolysis processes, while NaOH and $NaOH/NaClO_2$ treated fibers had one-step pyrolysis process. Compared with the NaOH treated fibers, the $NaOH/NaClO_2$ treated fibers had a lower thermal stability.

Cellulose I, cellulose II and cellulose I/II hybrid fibers were obtained during the delignification process. The ribbon shaped cellulose I fibers were converted to a swollen state with a rougher surface by 20wt% NaOH treatment for 10h. The higher NaOH concentration and longer NaOH treatment time contributed to the transition from cellulose I to II. Based on the

XRD results, the percentage of cellulose I decreased from 100% to 5%, and the CI values increased from 58.2% to 68.8% during the conversion from cellulose I to II. After a further $NaClO_2$ treatment, the CI values for the corresponding samples decreased due to partial destruction of intermolecular or/ and intramolecular hydrogen bond network. The CI (TCI) values for cellulose I/II hybrid fibers were smaller than that of pure cellulose I or cellulose II. The properties of cellulose I/II hybrid characterized in this study can provide some fundamental information for the potential application of cellulose I/II hybrid fibers in some anticipated fields, such as clothing, cosmetic, pharmaceuticals, biomedicine and smart materials.

Core-shell structured hydrogels consisting of a rigid SIPN shell and a flexible IPN core were prepared through chelation and covalent bonding of PVA-SA with Ca2+ and GA, respectively. Four kinds of CNPs (differences in particle size, aspect ratio and crystal structure) were incorporated into the hydrogel system. These CNPs were well dispersed in the hydrogels and reinforced the hydrogels via inter/intra-molecular hydrogen bonds. The hydrogel had micro-porous shells and macro-porous cores. The neat PSG-CA hydrogels with a water content of 94.2% provided an elastic modulus of 2.91 kPa and a maximum MB adsorption capacity of 33.6 mg/g. Although incorporation CNPs into the hydrogels decreased the thermal stabilities, dynamic oscillation and compression measurements showed that the CNPs dramatically elevated the viscoelasticity of the core and the compressive strength of the hydrogels. The modulus of the core and mechanical property of the hydrogels were in the order of PSG-CA-CNF I > PSG-CA-CNF I/II > PSG-CA-CNC I > PSG-CA-CNC I/II > PSG-CA, while their transparency was sequenced in a reverse order. PSG-CA-CNF I exhibited the strongest stiffness and its storage modulus and compressive strength were 13 and 3.2 times higher than that of neat PSG-CA. The incorporation of CNPs into core-shell structured hydrogels also increased the MB adsorption

capacity by 10%. The MB adsorbed on hydrogels in monolayers and multiple adsorption-desorption cycles could be applied to the hydrogels. The proposed hydrogel with good ductility core and high strength shell has many excellent properties, such as readily processed, eco-friendliness, favorable mechanical strength and promising adsorption capacity, the hydrogels could be used in treating many water pollutants (dye, toxic metals and agricultural residues removal). Moreover, the properties of the hydrogels could be regulated through selecting different CNPs and the potential applications could be extended to the areas in biosensors.

APPENDIX: PERMISSION LETTERS

For chapter 2:

ELSEVIER LICENSE
TERMS AND CONDITIONS

Sep 24, 2015

This is a License Agreement between Yiying Yue ("You") and Elsevier ("Elsevier") provided by Copyright Clearance Center ("CCC"). The license consists of your order details, the terms and conditions provided by Elsevier, and the payment terms and conditions.

All payments must be made in full to CCC. For payment instructions, please see information listed at the bottom of this form.

Supplier	Elsevier Limited The Boulevard, Langford Lane Kidlington,Oxford,OX5 1GB,UK
Registered Company Number	1982084
Customer name	Yiying Yue
Customer address	1350 Bob Pettit Blvd Apt 17 BATON ROUGE, LA 70820
License number	3715611348986
License date	Sep 24, 2015
Licensed content publisher	Elsevier
Licensed content publication	Industrial Crops and Products
Licensed content title	Cellulose fibers isolated from energycane bagasse using alkaline and sodium chlorite treatments: Structural, chemical and thermal properties
Licensed content author	Yiying Yue, Jingquan Han, Guangping Han, Giovanna M. Aita, Qinglin Wu
Licensed content date	15 December 2015
Licensed content volume number	76
Licensed content issue number	n/a
Number of pages	9

Start Page	355
End Page	363
Type of Use	reuse in a thesis/dissertation
Intended publisher of new work	other
Portion	full article
Format	electronic
Are you the author of this Elsevier article?	Yes
Will you be translating?	No
Title of your thesis/dissertation	CELLULOSE NANOFIBERS FROM ENERGYCANE BAGASSE AND THEIR APPLICATIONS IN CORE-SHELL STRUCTURED HYDROGELS
Expected completion date	Dec 2015
Estimated size (number of pages)	110
Elsevier VAT number	GB 494 6272 12
Permissions price	0.00 USD
VAT/Local Sales Tax	0.00 USD / 0.00 GBP
Total	0.00 USD
Terms and Conditions	

INTRODUCTION

1. The publisher for this copyrighted material is Elsevier. By clicking "accept" in connection with completing this licensing transaction, you agree that the following terms and conditions apply to this transaction (along with the Billing and Payment terms and conditions established by Copyright Clearance Center, Inc. ("CCC"), at the time that you opened your Rightslink account and that are available at any time athttp://myaccount.copyright.com).

GENERAL TERMS

2. Elsevier hereby grants you permission to reproduce the aforementioned material subject to the terms and conditions indicated.

3. Acknowledgement: If any part of the material to be used (for example, figures) has appeared in our publication with credit or acknowledgement to another source, permission must also be sought from that source. If such permission is not obtained then that material may not be included in your publication/copies. Suitable acknowledgement to the source must be made, either as a footnote or in a reference list at the end of your publication, as follows:

"Reprinted from Publication title, Vol /edition number, Author(s), Title of article / title of chapter, Pages No., Copyright (Year), with permission from Elsevier [OR APPLICABLE SOCIETY COPYRIGHT OWNER]." Also Lancet special credit - "Reprinted from The Lancet, Vol. number, Author(s), Title of article, Pages No., Copyright (Year), with permission from Elsevier."

4. Reproduction of this material is confined to the purpose and/or media for which permission is hereby given.

5. Altering/Modifying Material: Not Permitted. However figures and illustrations may be altered/adapted minimally to serve your work. Any other abbreviations, additions, deletions and/or any other alterations shall be made only with prior written authorization of Elsevier Ltd. (Please contact Elsevier at permissions@elsevier.com)

6. If the permission fee for the requested use of our material is waived in this instance, please be advised that your future requests for Elsevier materials may attract a fee.

7. Reservation of Rights: Publisher reserves all rights not specifically granted in the combination of (i) the license details provided by you and accepted in the course of this licensing transaction, (ii) these terms and conditions and (iii) CCC's Billing and Payment terms and conditions.

8. License Contingent Upon Payment: While you may exercise the rights licensed immediately upon issuance of the license at the end of the licensing process for the transaction, provided that you have disclosed complete and accurate details of your proposed use, no license is finally effective unless and until full payment is received from you (either by publisher or by CCC) as provided in CCC's Billing and Payment terms and conditions. If full payment is not received on a timely basis, then any license preliminarily granted shall be deemed automatically revoked and shall be void as if never granted. Further, in the event that you breach any of these terms and conditions or any of CCC's Billing and Payment terms and conditions, the license is automatically revoked and shall be void as if never granted. Use of materials as described in a revoked license, as well as any use of the materials beyond the scope of an unrevoked license, may constitute copyright infringement and publisher reserves the right to take any and all action to protect its copyright in the materials.

9. Warranties: Publisher makes no representations or warranties with respect to the licensed material.

10. Indemnity: You hereby indemnify and agree to hold harmless publisher and CCC, and their respective officers, directors, employees and agents, from and against any and all claims arising out of your use of the licensed material other than as specifically authorized pursuant to this license.

11. No Transfer of License: This license is personal to you and may not be sublicensed, assigned, or transferred by you to any other person without publisher's written permission.

12. No Amendment Except in Writing: This license may not be amended except in a writing signed by both parties (or, in the case of publisher, by CCC on publisher's behalf).

13. Objection to Contrary Terms: Publisher hereby objects to any terms contained in any purchase order, acknowledgment, check endorsement or other writing prepared by you, which terms are inconsistent with these terms and conditions or CCC's Billing and Payment terms and conditions. These terms and conditions, together with CCC's Billing and Payment terms and conditions (which are incorporated herein), comprise the entire agreement between you and publisher (and CCC) concerning this licensing transaction. In the event of any conflict between your obligations established by these terms and conditions and those established by CCC's Billing and Payment terms and conditions, these terms and conditions shall control.

14. Revocation: Elsevier or Copyright Clearance Center may deny the permissions described in this License at their sole discretion, for any reason or no reason, with a full refund payable to you. Notice of such denial will be made using the contact information provided by you. Failure to receive such notice will not alter or invalidate the denial. In no event will Elsevier or Copyright Clearance Center be responsible or liable for any costs, expenses or damage incurred by you as a result of a denial of your permission request, other than a refund of the amount(s) paid by you to Elsevier and/or Copyright Clearance Center for denied permissions.

LIMITED LICENSE

The following terms and conditions apply only to specific license types:

15. **Translation**: This permission is granted for non-exclusive world **English** rights only unless your license was granted for translation rights. If you licensed translation rights you may only translate this content into the languages you requested. A professional translator must perform all translations and reproduce the content word for word preserving the integrity of the article.

16. **Posting licensed content on any Website**: The following terms and conditions apply as follows: Licensing material from an Elsevier journal: All content posted to the web site must maintain the copyright information line on the bottom of each image; A hyper-text must be included to the Homepage of the journal from which you are licensing athttp://www.sciencedirect.com/science/journal/xxxxx or the Elsevier homepage for books athttp://www.elsevier.com; Central Storage: This license does not include permission for a scanned version of the material to be stored in a central repository such as that provided by Heron/XanEdu.

Licensing material from an Elsevier book: A hyper-text link must be included to the Elsevier homepage at http://www.elsevier.com. All content posted to the web site must maintain the copyright information line on the bottom of each image.

Posting licensed content on Electronic reserve: In addition to the above the following clauses are applicable: The web site must be password-protected and made available only to bona fide students registered on a relevant course. This permission is granted for 1 year only. You may obtain a new license for future website posting.

17. **For journal authors:** the following clauses are applicable in addition to the above:

Preprints:

A preprint is an author's own write-up of research results and analysis, it has not been peer-reviewed, nor has it had any other value added to it by a publisher (such as formatting, copyright, technical enhancement etc.).

Authors can share their preprints anywhere at any time. Preprints should not be added to or enhanced in any way in order to appear more like, or to substitute for, the final versions of articles however authors can update their preprints on arXiv or RePEc with their Accepted Author Manuscript (see below).

If accepted for publication, we encourage authors to link from the preprint to their formal publication via its DOI. Millions of researchers have access to the formal publications on ScienceDirect, and so links will help users to find, access, cite and use the best available version. Please note that Cell Press, The Lancet and some society-owned have different preprint policies. Information on these policies is available on the journal homepage.

Accepted Author Manuscripts: An accepted author manuscript is the manuscript of an article that has been accepted for publication and which typically includes author-incorporated changes suggested during submission, peer review and editor-author communications.

Authors can share their accepted author manuscript:

- –immediately
    - via their non-commercial person homepage or blog
    - by updating a preprint in arXiv or RePEc with the accepted manuscript
    - via their research institute or institutional repository for internal institutional uses or as part of an invitation-only research collaboration work-group
    - directly by providing copies to their students or to research collaborators for their personal use
    - for private scholarly sharing as part of an invitation-only work group on commercial sites with which Elsevier has an agreement
- –after the embargo period
    - via non-commercial hosting platforms such as their institutional repository
    - via commercial sites with which Elsevier has an agreement

In all cases accepted manuscripts should:

- –link to the formal publication via its DOI
- –bear a CC-BY-NC-ND license - this is easy to do
- –if aggregated with other manuscripts, for example in a repository or other site, be shared in alignment with our hosting policy not be added to or enhanced in any way to appear more like, or to substitute for, the published journal article.

Published journal article (JPA): A published journal article (PJA) is the definitive final record of published research that appears or will appear in the journal and embodies all value-adding publishing activities including peer review co-ordination, copy-editing, formatting, (if relevant) pagination and online enrichment.

Policies for sharing publishing journal articles differ for subscription and gold open access articles:

Subscription Articles: If you are an author, please share a link to your article rather than the full-text. Millions of researchers have access to the formal publications on ScienceDirect, and so links will help your users to find, access, cite, and use the best available version.

Theses and dissertations which contain embedded PJAs as part of the formal submission can be posted publicly by the awarding institution with DOI links back to the formal publications on ScienceDirect.

If you are affiliated with a library that subscribes to ScienceDirect you have additional private sharing rights for others' research accessed under that agreement. This includes use for classroom teaching and internal training at the institution (including use in course packs and courseware programs), and inclusion of the article for grant funding purposes.

Gold Open Access Articles: May be shared according to the author-selected end-user license and should contain a CrossMark logo, the end user license, and a DOI link to the formal publication on ScienceDirect.

Please refer to Elsevier's posting policy for further information.

18. **For book authors** the following clauses are applicable in addition to the above: Authors are permitted to place a brief summary of their work online only. You are not allowed to download and post the published electronic version of your chapter, nor may you scan the printed edition to create an electronic version. **Posting to a repository:** Authors are permitted to post a summary of their chapter only in their institution's repository.

19. **Thesis/Dissertation**: If your license is for use in a thesis/dissertation your thesis may be submitted to your institution in either print or electronic form. Should your thesis be published commercially, please reapply for permission. These requirements include permission for the Library and Archives of Canada to supply single copies, on demand, of the complete thesis and include permission for Proquest/UMI to supply single copies, on demand, of the complete thesis. Should your thesis be published commercially, please reapply for permission. Theses and dissertations which contain embedded PJAs as part of the formal submission can be posted publicly by the awarding institution with DOI links back to the formal publications on ScienceDirect.

Elsevier Open Access Terms and Conditions

You can publish open access with Elsevier in hundreds of open access journals or in nearly 2000 established subscription journals that support open access publishing. Permitted third party re-use of these open access articles is defined by the author's choice of Creative Commons user license. See our open access license policy for more information.

Terms & Conditions applicable to all Open Access articles published with Elsevier:

Any reuse of the article must not represent the author as endorsing the adaptation of the article nor should the article be modified in such a way as to damage the author's honour or reputation. If any changes have been made, such changes must be clearly indicated.

The author(s) must be appropriately credited and we ask that you include the end user license and a DOI link to the formal publication on ScienceDirect.

If any part of the material to be used (for example, figures) has appeared in our publication with credit or acknowledgement to another source it is the responsibility of the user to ensure their reuse complies with the terms and conditions determined by the rights holder.

Additional Terms & Conditions applicable to each Creative Commons user license:

CC BY: The CC-BY license allows users to copy, to create extracts, abstracts and new works from the Article, to alter and revise the Article and to make commercial use of the Article (including reuse and/or resale of the Article by commercial entities), provided the user gives appropriate credit (with a link to the formal publication through the relevant DOI), provides a link to the license, indicates if changes were made and the licensor is not represented as endorsing the use made of the work. The full details of the license are available at http://creativecommons.org/licenses/by/4.0.

CC BY NC SA: The CC BY-NC-SA license allows users to copy, to create extracts, abstracts and new works from the Article, to alter and revise the Article, provided this is not done for commercial purposes, and that the user gives appropriate credit (with a link to the formal publication through the relevant DOI), provides a link to the license, indicates if changes were made and the licensor is not represented as endorsing the use made of the work. Further, any new works must be made available on the same conditions. The full details of the license are available at http://creativecommons.org/licenses/by-nc-sa/4.0.

CC BY NC ND: The CC BY-NC-ND license allows users to copy and distribute the Article, provided this is not done for commercial purposes and further does not permit distribution of the Article if it is changed or edited in any way, and provided the user gives appropriate credit (with a link to the formal publication through the relevant DOI), provides a link to the license, and that the licensor is not represented as endorsing the use made of the work. The full details of the license are available at http://creativecommons.org/licenses/by-nc-nd/4.0. Any commercial reuse of Open Access articles published with a CC BY NC SA or CC BY NC ND license requires permission from Elsevier and will be subject to a fee.

Commercial reuse includes:

- –Associating advertising with the full text of the Article
- –Charging fees for document delivery or access
- –Article aggregation
- –Systematic distribution via e-mail lists or share buttons

Posting or linking by commercial companies for use by customers of those companies.

20.**Other Conditions**:

v1.8

Questions?customercare@copyright.com or +1-855-239-3415 (toll free in the US) or +1-978-646-2777.

For chapter 3:

ELSEVIER LICENSE
TERMS AND CONDITIONS

Sep 24, 2015

This is a License Agreement between Yiying Yue ("You") and Elsevier ("Elsevier") provided by Copyright Clearance Center ("CCC"). The license consists of your order details, the terms and conditions provided by Elsevier, and the payment terms and conditions.

All payments must be made in full to CCC. For payment instructions, please see information listed at the bottom of this form.

Supplier	Elsevier Limited The Boulevard, Langford Lane Kidlington,Oxford,OX5 1GB,UK
Registered Company Number	1982084
Customer name	Yiying Yue
Customer address	1350 Bob Pettit Blvd Apt 17 BATON ROUGE, LA 70820
License number	3715590901715
License date	Sep 24, 2015
Licensed content publisher	Elsevier
Licensed content publication	Carbohydrate Polymers
Licensed content title	Characterization of cellulose I/II hybrid fibers isolated from energycane bagasse during the delignification process: Morphology, crystallinity and percentage estimation
Licensed content author	Yiying Yue, Jingquan Han, Guangping Han, Quanguo Zhang, Alfred D. French, Qinglin Wu
Licensed content date	20 November 2015
Licensed content volume number	133
Licensed content issue number	n/a
Number of pages	10
Start Page	438
End Page	447
Type of Use	reuse in a thesis/dissertation

Portion	full article
Format	electronic
Are you the author of this Elsevier article?	Yes
Will you be translating?	No
Title of your thesis/dissertation	CELLULOSE NANOFIBERS FROM ENERGYCANE BAGASSE AND THEIR APPLICATIONS IN CORE-SHELL STRUCTURED HYDROGELS
Expected completion date	Dec 2015
Estimated size (number of pages)	110
Elsevier VAT number	GB 494 6272 12
Permissions price	0.00 USD
VAT/Local Sales Tax	0.00 USD / 0.00 GBP
Total	0.00 USD
Terms and Conditions	

INTRODUCTION

1. The publisher for this copyrighted material is Elsevier. By clicking "accept" in connection with completing this licensing transaction, you agree that the following terms and conditions apply to this transaction (along with the Billing and Payment terms and conditions established by Copyright Clearance Center, Inc. ("CCC"), at the time that you opened your Rightslink account and that are available at any time at http://myaccount.copyright.com).

GENERAL TERMS

2. Elsevier hereby grants you permission to reproduce the aforementioned material subject to the terms and conditions indicated.

3. Acknowledgement: If any part of the material to be used (for example, figures) has appeared in our publication with credit or acknowledgement to another source, permission must also be sought from that source. If such permission is not obtained then that material may not be included in your publication/copies. Suitable acknowledgement to the source must be made, either as a footnote or in a reference list at the end of your publication, as follows:

"Reprinted from Publication title, Vol /edition number, Author(s), Title of article / title of chapter, Pages No., Copyright (Year), with permission from Elsevier [OR APPLICABLE SOCIETY COPYRIGHT OWNER]." Also Lancet special credit - "Reprinted from The Lancet, Vol. number, Author(s), Title of article, Pages No., Copyright (Year), with permission from Elsevier."

4. Reproduction of this material is confined to the purpose and/or media for which permission is hereby given.

5. Altering/Modifying Material: Not Permitted. However figures and illustrations may be altered/adapted minimally to serve your work. Any other abbreviations, additions, deletions and/or any other alterations shall be made only with prior written authorization of Elsevier Ltd. (Please contact Elsevier at permissions@elsevier.com)

6. If the permission fee for the requested use of our material is waived in this instance, please be advised that your future requests for Elsevier materials may attract a fee.

7. Reservation of Rights: Publisher reserves all rights not specifically granted in the combination of (i) the license details provided by you and accepted in the course of this licensing transaction, (ii) these terms and conditions and (iii) CCC's Billing and Payment terms and conditions.

8. License Contingent Upon Payment: While you may exercise the rights licensed immediately upon issuance of the license at the end of the licensing process for the transaction, provided that you have disclosed complete and accurate details of your proposed use, no license is finally effective unless and until full payment is received from you (either by publisher or by CCC) as provided in CCC's Billing and Payment terms and conditions. If full payment is not received on a timely basis, then any license preliminarily granted shall be deemed automatically revoked and shall be void as if never granted. Further, in the event that you breach any of these terms and conditions or any of CCC's Billing and Payment terms and conditions, the license is automatically revoked and shall be void as if never granted. Use of materials as described in a revoked license, as well as any use of the materials beyond the scope of an unrevoked license, may constitute copyright infringement and publisher reserves the right to take any and all action to protect its copyright in the materials.

9. Warranties: Publisher makes no representations or warranties with respect to the licensed material.

10. Indemnity: You hereby indemnify and agree to hold harmless publisher and CCC, and their respective officers, directors, employees and agents, from and against any and all claims arising out of your use of the licensed material other than as specifically authorized pursuant to this license.

11. No Transfer of License: This license is personal to you and may not be sublicensed, assigned, or transferred by you to any other person without publisher's written permission.

12. No Amendment Except in Writing: This license may not be amended except in a writing signed by both parties (or, in the case of publisher, by CCC on publisher's behalf).

13. Objection to Contrary Terms: Publisher hereby objects to any terms contained in any purchase order, acknowledgment, check endorsement or other writing prepared by you, which terms are inconsistent with these terms and conditions or CCC's Billing and Payment terms and conditions. These terms and conditions, together with CCC's Billing and Payment terms and conditions (which are incorporated herein), comprise the entire agreement between you and

publisher (and CCC) concerning this licensing transaction. In the event of any conflict between your obligations established by these terms and conditions and those established by CCC's Billing and Payment terms and conditions, these terms and conditions shall control.

14. Revocation: Elsevier or Copyright Clearance Center may deny the permissions described in this License at their sole discretion, for any reason or no reason, with a full refund payable to you. Notice of such denial will be made using the contact information provided by you. Failure to receive such notice will not alter or invalidate the denial. In no event will Elsevier or Copyright Clearance Center be responsible or liable for any costs, expenses or damage incurred by you as a result of a denial of your permission request, other than a refund of the amount(s) paid by you to Elsevier and/or Copyright Clearance Center for denied permissions.

LIMITED LICENSE

The following terms and conditions apply only to specific license types:

15. **Translation**: This permission is granted for non-exclusive world **English** rights only unless your license was granted for translation rights. If you licensed translation rights you may only translate this content into the languages you requested. A professional translator must perform all translations and reproduce the content word for word preserving the integrity of the article.

16. **Posting licensed content on any Website**: The following terms and conditions apply as follows: Licensing material from an Elsevier journal: All content posted to the web site must maintain the copyright information line on the bottom of each image; A hyper-text must be included to the Homepage of the journal from which you are licensing athttp://www.sciencedirect.com/science/journal/xxxxx or the Elsevier homepage for books athttp://www.elsevier.com; Central Storage: This license does not include permission for a scanned version of the material to be stored in a central repository such as that provided by Heron/XanEdu.

Licensing material from an Elsevier book: A hyper-text link must be included to the Elsevier homepage at http://www.elsevier.com . All content posted to the web site must maintain the copyright information line on the bottom of each image.

Posting licensed content on Electronic reserve: In addition to the above the following clauses are applicable: The web site must be password-protected and made available only to bona fide students registered on a relevant course. This permission is granted for 1 year only. You may obtain a new license for future website posting.

17. **For journal authors:** the following clauses are applicable in addition to the above:

Preprints:

A preprint is an author's own write-up of research results and analysis, it has not been peer-reviewed, nor has it had any other value added to it by a publisher (such as formatting, copyright, technical enhancement etc.).

Authors can share their preprints anywhere at any time. Preprints should not be added to or enhanced in any way in order to appear more like, or to substitute for, the final versions of articles however authors can update their preprints on arXiv or RePEc with their Accepted Author Manuscript (see below).

If accepted for publication, we encourage authors to link from the preprint to their formal publication via its DOI. Millions of researchers have access to the formal publications on ScienceDirect, and so links will help users to find, access, cite and use the best available version. Please note that Cell Press, The Lancet and some society-owned have different preprint policies. Information on these policies is available on the journal homepage.

Accepted Author Manuscripts: An accepted author manuscript is the manuscript of an article that has been accepted for publication and which typically includes author-incorporated changes suggested during submission, peer review and editor-author communications.

Authors can share their accepted author manuscript:

- -immediately
    - via their non-commercial person homepage or blog
    - by updating a preprint in arXiv or RePEc with the accepted manuscript
    - via their research institute or institutional repository for internal institutional uses or as part of an invitation-only research collaboration work-group
    - directly by providing copies to their students or to research collaborators for their personal use
    - for private scholarly sharing as part of an invitation-only work group on commercial sites with which Elsevier has an agreement
- -after the embargo period
    - via non-commercial hosting platforms such as their institutional repository
    - via commercial sites with which Elsevier has an agreement

In all cases accepted manuscripts should:

- -link to the formal publication via its DOI
- -bear a CC-BY-NC-ND license - this is easy to do
- -if aggregated with other manuscripts, for example in a repository or other site, be shared in alignment with our hosting policy not be added to or enhanced in any way to appear more like, or to substitute for, the published journal article.

Published journal article (JPA): A published journal article (PJA) is the definitive final record of published research that appears or will appear in the journal and embodies all value-adding publishing activities including peer review co-ordination, copy-editing, formatting, (if relevant) pagination and online enrichment.

Policies for sharing publishing journal articles differ for subscription and gold open access articles:

Subscription Articles: If you are an author, please share a link to your article rather than the full-text. Millions of researchers have access to the formal publications on ScienceDirect, and so

links will help your users to find, access, cite, and use the best available version.

Theses and dissertations which contain embedded PJAs as part of the formal submission can be posted publicly by the awarding institution with DOI links back to the formal publications on ScienceDirect.

If you are affiliated with a library that subscribes to ScienceDirect you have additional private sharing rights for others' research accessed under that agreement. This includes use for classroom teaching and internal training at the institution (including use in course packs and courseware programs), and inclusion of the article for grant funding purposes.

Gold Open Access Articles: May be shared according to the author-selected end-user license and should contain a CrossMark logo, the end user license, and a DOI link to the formal publication on ScienceDirect.

Please refer to Elsevier's posting policy for further information.

18. **For book authors** the following clauses are applicable in addition to the above: Authors are permitted to place a brief summary of their work online only. You are not allowed to download and post the published electronic version of your chapter, nor may you scan the printed edition to create an electronic version. **Posting to a repository:** Authors are permitted to post a summary of their chapter only in their institution's repository.

19. **Thesis/Dissertation**: If your license is for use in a thesis/dissertation your thesis may be submitted to your institution in either print or electronic form. Should your thesis be published commercially, please reapply for permission. These requirements include permission for the Library and Archives of Canada to supply single copies, on demand, of the complete thesis and include permission for Proquest/UMI to supply single copies, on demand, of the complete thesis. Should your thesis be published commercially, please reapply for permission. Theses and dissertations which contain embedded PJAs as part of the formal submission can be posted publicly by the awarding institution with DOI links back to the formal publications on ScienceDirect.

Elsevier Open Access Terms and Conditions

You can publish open access with Elsevier in hundreds of open access journals or in nearly 2000 established subscription journals that support open access publishing. Permitted third party re-use of these open access articles is defined by the author's choice of Creative Commons user license. See our open access license policy for more information.

Terms & Conditions applicable to all Open Access articles published with Elsevier:

Any reuse of the article must not represent the author as endorsing the adaptation of the article nor should the article be modified in such a way as to damage the author's honour or reputation. If any changes have been made, such changes must be clearly indicated.

The author(s) must be appropriately credited and we ask that you include the end user license and

a DOI link to the formal publication on ScienceDirect.

If any part of the material to be used (for example, figures) has appeared in our publication with credit or acknowledgement to another source it is the responsibility of the user to ensure their reuse complies with the terms and conditions determined by the rights holder.

Additional Terms & Conditions applicable to each Creative Commons user license:

CC BY: The CC-BY license allows users to copy, to create extracts, abstracts and new works from the Article, to alter and revise the Article and to make commercial use of the Article (including reuse and/or resale of the Article by commercial entities), provided the user gives appropriate credit (with a link to the formal publication through the relevant DOI), provides a link to the license, indicates if changes were made and the licensor is not represented as endorsing the use made of the work. The full details of the license are available at http://creativecommons.org/licenses/by/4.0.

CC BY NC SA: The CC BY-NC-SA license allows users to copy, to create extracts, abstracts and new works from the Article, to alter and revise the Article, provided this is not done for commercial purposes, and that the user gives appropriate credit (with a link to the formal publication through the relevant DOI), provides a link to the license, indicates if changes were made and the licensor is not represented as endorsing the use made of the work. Further, any new works must be made available on the same conditions. The full details of the license are available at http://creativecommons.org/licenses/by-nc-sa/4.0.

CC BY NC ND: The CC BY-NC-ND license allows users to copy and distribute the Article, provided this is not done for commercial purposes and further does not permit distribution of the Article if it is changed or edited in any way, and provided the user gives appropriate credit (with a link to the formal publication through the relevant DOI), provides a link to the license, and that the licensor is not represented as endorsing the use made of the work. The full details of the license are available at http://creativecommons.org/licenses/by-nc-nd/4.0. Any commercial reuse of Open Access articles published with a CC BY NC SA or CC BY NC ND license requires permission from Elsevier and will be subject to a fee.

Commercial reuse includes:

- -Associating advertising with the full text of the Article
- -Charging fees for document delivery or access
- -Article aggregation
- -Systematic distribution via e-mail lists or share buttons

Posting or linking by commercial companies for use by customers of those companies.

20. **Other Conditions**:

v1.8

Questions? customercare@copyright.com or +1-855-239-3415 (toll free in the US) or +1-978-646-2777.

Gratis licenses (referencing $0 in the Total field) are free. Please retain this printable license for your reference. No payment is required.

VITA

Yiying Yue was born in Harbin, China, in 1985. She received a Bachelor of Science degree in environmental engineering from Heilongjiang Institute of Science and Technology, Harbin, China, in July 2007. She gained valuable work experience as a Research Assistant in the field of bio-based composites at the Key Laboratory of Bio-based Material Science and Technology, Northeast Forestry University, Harbin, China. After receiving her Master's degree in forestry products at Louisiana State University under the direction of Dr. Qinglin Wu, she transferred to environmental engineering to work with Dr. William Moe as a master student. In 2014, she joined the Ph.D program in Renewable Natural Resources, advised by Dr. Qinglin Wu. Her research focuses on isolation cellulose fibers form agricultural waters, preparation of multifunctional bio-based polymers, and application of micro/ nano cellulose composites in treating water pollutants and other novel areas. So far, she has published six SCI papers as first author. Yiying Yue is expected to graduate in December 2015 and continue to explore the field of applying eco-friendly micro/nano composites on water treatment and pollution monitoring.